DYNAMIC CONDENSATION OF SEMICONDUCTOR MICROCAVITY POLARITONS

A DISSERTATION

SUBMITTED TO THE DEPARTMENT OF APPLIED PHYSICS

AND THE COMMITTEE ON GRADUATE STUDIES

OF STANFORD UNIVERSITY

IN PARTIAL FULFILLMENT OF THE REQUIREMENTS

FOR THE DEGREE OF

DOCTOR OF PHILOSOPHY

Hui Deng

June 2006

I certify that I have read this dissertation and that, in my opinion, it is fully adequate in scope and quality as a dissertation for the degree of Doctor of Philosophy.

———————————————————
Yoshihisa Yamamoto
(Principal Adviser)

I certify that I have read this dissertation and that, in my opinion, it is fully adequate in scope and quality as a dissertation for the degree of Doctor of Philosophy.

———————————————————
Alexander Fetter

I certify that I have read this dissertation and that, in my opinion, it is fully adequate in scope and quality as a dissertation for the degree of Doctor of Philosophy.

———————————————————
Mark Kasevich

Approved for the University Committee on Graduate Studies.

Abstract

There are a countable number of experimental systems where a macroscopic quantum order is established, such as lasers, superfluids, superconductors and Bose-Einstein condensates of atomic vapors. Each of these systems has deepened our fundamental understanding of many-body physics, and has led to novel research tools as well as applications. A newcomer to the family is the unique half-light half-matter quasi-particles in solids – the semiconductor microcavity polaritons. In this thesis, we use microcavities with multiple GaAs-quantum wells and search for a macroscopic phase of the polaritons at a temperature of 4 K.

We demonstrated a quantum degeneracy threshold of polaritons stemming from the Bose final state stimulation of polaritons. The threshold density is two orders of magnitude less than that of a photon laser and well below the electronic population inversion condition. This result is a proof of principle that microcavity polaritons hold promise for a new source of coherent light with high energy efficiency.

Further, many of the quantum statistical properties of polariton can be directly measured by well-developed optical techniques. We study for the first time the time-domain second order coherence function of the polaritons, and demonstrate that macroscopic coherence gradually builds up in the polariton ground state above the quantum degeneracy threshold. We measure the momentum distributions of the polaritons, and observe a quantum degenerate Bose-Einstein distribution at the lattice temperature, with a chemical potential close to zero. This is the first observation of simultaneous quantum degeneracy and thermal equilibrium in a gas of quasi-particles in solids. Polarization properties and spatial distributions of the polariton condensate also show distinct features associated with the phase transition.

Acknowledgement

When we dream alone it is only a dream, but when many dream together it is the beginning of a new reality.

— Friedensreich Hundertwasser

This thesis is a humble dream of a naive student turned into reality by the guidance and support of many.

I would like to thank Professor Yoshihisa Yamamoto for his constant mentorship and support throughout the thesis, for his insight and inspiration, for his guidance and encouragement behind every bit of my progress, and for his patience and understanding when the progress is slow. Above all, I thank him for deeply caring for his students rather than the work done by them. He congratulates me on any improvement I make on any aspect of the academics. After a most frustrating experiment with the most disappointing data, a discussion with him always fills me up again with hope and excitement of scientific exploration. He gives us ample room for trying out crazy new ideas and perfecting working ones. His way of mentoring evolves when we grow mature, he always tries to trigger our own creativity with admirable patience and optimism. He set for me an example of a great scientist and a great educator. He made it possible not only this thesis but also a most enjoyable and memorable time of my graduate years.

I would like to thank my oral defense committee: Professor Willam. E. Morner, Theodori H. Geballe, Alexander Fetter, and Mark Kasevich. I thank them for their time and interest, and for the many interesting questions they asked. Particularly, I thank Professor Morner for chairing my defense. I thank Professor Geballe for his kind

extremely talented and diligent group, while also exceptionally collegial and supportive. They together created a most intellectually nurturing environment. Especially, I thank Patrik Recher for also being a great friend in the last couple year, and for never tired of answering my questions however nonsensical they are sometimes. I thank the senior members, William D. Oliver, Edo Waks, Charles Santori, Cyrus Master, and Xavier Maire, for their warm friendship and support especially during my earlier years in the group, and for helping me on numerous occasions in the lab or with paper and pencil. And I thank Anne Verhulst for the good times we had sharing the office.

I would like to thank the secretaries of our group: Yurika Peterman, Rieko Sasaki, Mayumi. It is their hard work behind the scene that made the group to run smoothly, they also add a family touch to the group.

I would like to thank our collaborators who generously provided the samples for this thesis: J. Block from CNRS, France; R. Hey and K. H. Ploog from Paul-Drude-Institut, Germany; A. Pawlis and K. Lischka from University at Paderborn, Germany; A. Forchel from Julius-Maximilians-University Wuerzburg, Germany.

Last but not least, I would like to thank my parents and sister for their unconditional love and support from afar. And I would like to thank Zhongmin Xiong — the one other most significant person in my life who cared more for me and for this thesis than I do. I thank him for his love and care throughout the six years we have been together, for adding another layer of meaning to my life.

Contents

List of Tables

List of Figures

xvii

Chapter 1

Introduction

The physical world is most studied and best understood at its two limits: the macroscopic limit described by Newton's laws and Einstein's relativistic theories, and the microscopic limit described by quantum mechanics. Bridging these two limits are a few examples of 'macroscopic quantum states' – macroscopically big systems described by the laws of quantum mechanics, exhibiting features alien to the classical theories.

The most common example is a laser, where a macroscopically large number of photons have almost identical energy and momentum, described by a single mode wavefunction, can travel over thousands of miles without decoherence or divergence. It is so common that it is often considered as a classical state despite its quantum mechanical origin. More exotic are some matter wave systems, such as superconductors, superfluids, and atomic Bose-Einstein condensates.

A new emerging addition to the family is a half-matter half-light system — the polaritons, which are quasi-particles originating from strong light and matter coupling in solids. The theme of this thesis is the search for a macroscopic quantum state of polaritons, more specifically, the dynamical condensation of semiconductor microcavity polaritons.

1.1 Phase Diagram of Polaritons

When the optical field of a semiconductor microcavity strongly couples to the excitons in embedded quantum wells (QWs), new normal modes are formed — the lower polariton (LP) and the upper polariton (UP) (5). A variety of quantum phases are predicted for polaritons, including Bose-Einstein Condensation (BEC), superfluidity, and crossover from BEC to Bardeen-Cooper-Schrieffer (BCS) states (6; 7; 1; 8; 9). One possible phase diagram of microcavity polaritons is shown in figure 1.1. In the low density limit ($n_{exc}a^{*2} \ll 1$, n_{exc} is the exciton density and a^* is the exciton Bohr radius), polaritons are well approximated as bosonic particles, and form a BEC state below a critical temperature. Macroscopic coherence exists in the system in both the cavity field (the photon components) and the matter media (the excitonic components). Above a saturation density and with a low decoherence rate, excitons dissociate while momentum-space pairing forms between an electron and a hole, like in a BCS state, which still coherently couple to the cavity photon field. In experimental systems available today, decoherence in the electronic media is so high that only a laser transition is possible in the limit of high carrier densities. Hence in this thesis we focus on the low-density regime well below the exciton saturation density (which is about one order of magnitude below the Mott transition density), where a BEC-like transition is expected.

1.2 Experimental Realizations of BEC

BEC is a common phenomenon in all forms of matter at all scales, including Higgs Bosons. The more mundane systems one can manipulate in table top experiments are mainly, atomic and solid state systems. Table 1.1 compares the basic parameters of atomic gases to excitons and polaritons in semiconductors.

The parameter scales of these systems differ by many orders of magnitude. Even in a common quantum phase transition, each system is expected to have its own characteristics, to reveal particular pieces of unexplored fundamental physics, and
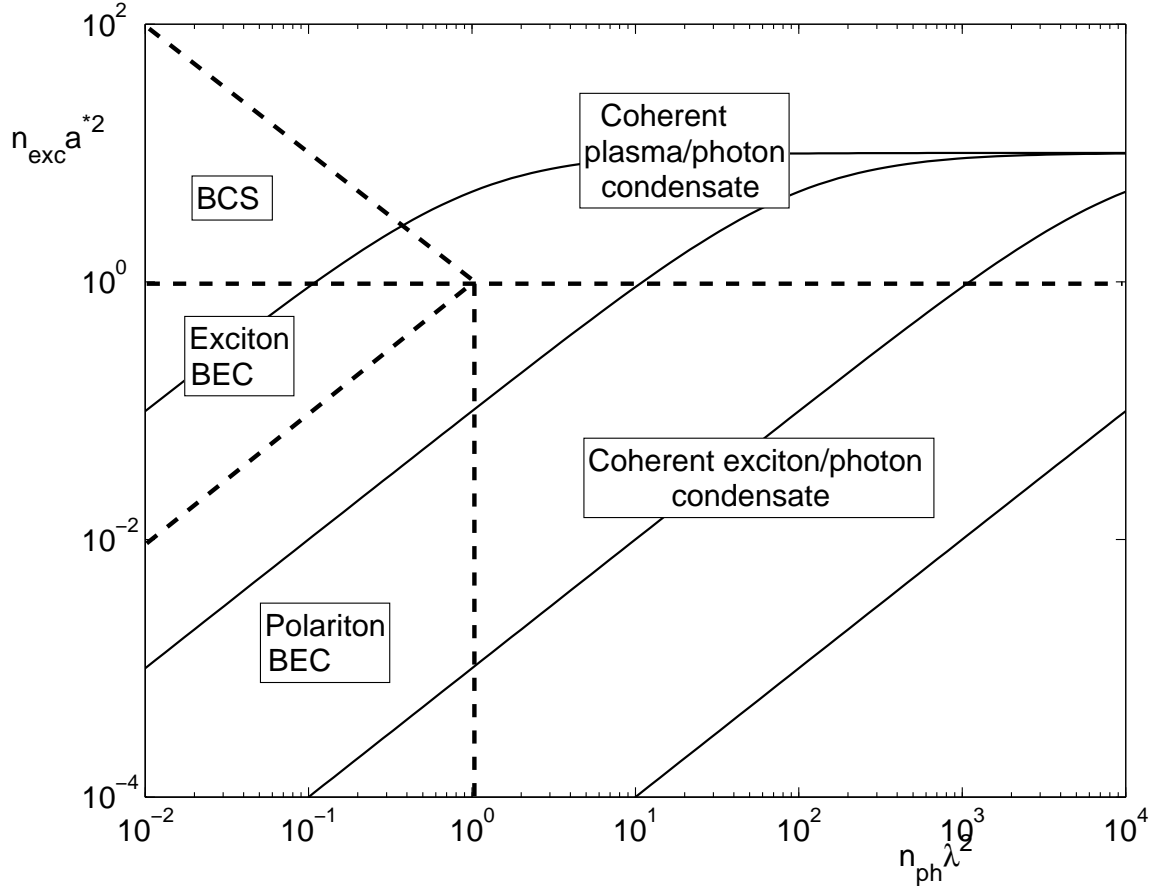
Figure 1.1: Taken from reference (1), by Littlewood, et al. Sketch to demonstrate the various crossovers in a polariton system assuming localized excitons. The vertical axis $n_{exc}a^{*2}$ is exciton density normalized by the exciton Bohr radius a^*. The horizontal axis $n_{ph}\lambda^2$ is the normalized cavity photon density. $\lambda \doteq \hbar^2/2M^*g$, where g is the coupling strength per exciton, $M^* \doteq m_e + m_h$ is the exciton effective mass and m_e and m_h are the effective mass of electron and hole respectively. The crossover from BEC of polaritons to an interaction-driven polariton condensate occurs when $n_{ph}\lambda^2 \approx 1$; the conventional BEC/BCS crossover for excitons occurs when $n_{exc}a^* \approx 1$, and at large photon numbers this marks the conventional point of inversion for a plasma "laser". The two wedges labeled BCS and exciton BEC constitute the regime where the Coulomb interaction is the dominant coupling term. The solid lines are rough guides to trajectories that would be followed for a fixed ratio of the coupling constants $(a^*/\lambda)^2 = (g/Ryd.)(M^*/m) = 10, \ 10^{-1}, \ 10^{-3}, \ 10^{-5}$, where $m \doteq \frac{m_e m_h}{m_e + m_h}$ is the exciton reduced mass. In order for the electron-hole density to be able to reach such high values as shown, the cavity mode frequency would need to be placed well above the edge of the band.

Table 1.1: Parameter Comparison of BEC Systems

systems	atomic gases	excitons	polaritons
effective mass m^*/m_e	10^3	10^{-1}	10^{-5}
Bohr radius a_B	10^{-1} Å	10^2 Å	10^2 Å
particle spacing: $n^{-\frac{1}{d}}$	10^3 Å	10^2 Å	1 μm
critical temperature T_c	1 nK~1 μK	1 mK~1 K	1 K~ >300 K
thermalization time / lifetime	1 ms/1 s $\sim 10^{-3}$	10 ps/1 ns $\sim 10^{-2}$	(1~10 ps)/(1~10 ps) $= 0.1$~10

to have unique applications. Most notable for the polariton system is its very light effective mass and very short time scale. The former leads to a critical temperature of phase transitions ranging from 1 K up to room temperature. The latter dictates the dynamic nature of polariton phase transitions. We will leave to chapter 3 more detailed discussions of the special properties of polaritons. Below we briefly review the history of BEC research for the above systems.

1.2.1   BEC of Atomic Systems

Atomic BEC systems include mainly liquid-^{4}He and ^{3}He, spin-polarized hydrogen gases, and dilute atomic gases. Liquid-^{4}He has the longest history for BEC study, since it was the first to demonstrate superfluidity, a macroscopic quantum phenomenon intimately related to BEC. However, helium atoms interact strongly via hard-core repulsion. The interaction is too strong to be treated perturbatively and a detailed microscopic theory of helium condensation is not available. At the same time, the strong interaction depletes the condensate ground state and renders a small condensate fraction of < 10%. Many salient features of BEC, that are predicted for an ideal or weakly interacting gases, are not expected for liquid helium. Consequently, experimental confirmation of BEC in liquid helium has been difficult, and interpretation of the experimental results are often model-dependent (10). Conclusive

evidence for BEC came first from dilute atomic gases in 1995 (11; 12; 13), and later in spin-polarized hydrogen (14) and metastable helium gases (15; 16). These systems now provide a powerful testing ground for a wide range of fundamental problems in many-body physics.

1.2.2   BEC in Solids

While atom BEC has been demonstrated since 1995 in various species of atomic gases and has evolved into a rather mature sub-discipline of its own, no analogue has been established in solid state systems. Whether or not BEC can be realized in solids remains a most debated and intriguing problem of modern physics. Mainly due to the slow progress in experimental work, BEC in solids is still a much less explored field. Two outstanding problems for solid state BEC are: to have an equilibrium system with high enough density, and to obtain clear experimental evidence in spite of the complications of solids.

Excitons

Exciton BEC was first proposed in 1962 by Moskalenko et al. (17) and Blatt et al. (18). A most well-known experimental system is the ortho-excitons in bulk Cu_2O. This system was considered to have shown, in the first conference on BEC held in 1995, the most convincing evidence of BEC (19). Yet it was found out later that the auger-recombination of excitons prevented the system from reaching the critical density of BEC (20; 21; 22). In 2002, a few macroscopic phenomena observed in quantum-well exciton systems were again proposed to be related to BEC (23; 24). Yet more careful analysis later concluded otherwise. Indirect evidence of quantum degeneracy was obtained with quantum-well excitons (e.g. reference (25; 26)), yet no evidence of a phase transition was inferred from these experiments, e.g. the coherence properties and momentum distribution functions of the excitons. The search continues for exciton BEC and the question remains open if BEC is ever possible in a solid state system.

Bulk Polaritons

In 1968, BEC was proposed to be also possible with bulk polaritons (6). However, these polaritons are outside of the optical cone (the LP branch in figure 3.15) and do not directly couple to light. It is very difficult to study the bulk polaritons experimentally. Moreover, the minimum energy of the bulk polariton bands are the crystal ground state with zero excitation energy. BEC is possible only with states at an energy-relaxation bottleneck. These states have a large degeneracy in momentum, adding much complication to the physics. There has been no successful experimental effort toward bulk polariton condensation.

Microcavity Polaritons

A more experimentally accessible solid-state system becomes available when the strong-coupling regime is reached in an epitaxially grown quantum-well microcavity (5). Due to confinement of both the cavity photon field and the quantum excitons along the growth direction, translational symmetry is broken in the longitudinal direction, only the transverse wavenumber $k_\parallel$ is a good quantum number for microcavity polaritons. Hence for the relevant polariton states, there exists a one-to-one coupling between each internal polariton mode with certain $k_\parallel$ at energy $E_{LP}(k_\parallel)$ and each external photon mode with the same $k_\parallel$ and $E_{LP}(k_\parallel)$ emitted into certain angle θ relative to the growth direction. The coupling rate is determined by the fixed cavity photon out-coupling rate. As a result, information about the internal polaritons can be directly obtained from the external photon emission by well developed optical techniques.

Within a decade after the first observation of microcavity polaritons, stimulated scattering threshold of polaritons were reported by various groups (27; 28; 29; 30). More recently, first-order spatial coherence was studied for bottleneck polaritons above the stimulated scattering threshold (31). Many pieces of evidence for a polariton phase transition are gathered in the course of this dissertation, as will be discussed in later chapters.

1.3   Outline of Thesis

This thesis is an experimental study of the dynamical condensation of semiconductor microcavity polaritons. We first introduce in chapters 2 and 3 the basic concepts of Bose-Einstein condensation and the fundamentals of the semiconductor microcavity system. In chapter 4 we discuss what are the experimental techniques to study the system, and how the samples are characterized.

The first step toward polariton condensation is presented in chapter 5 — reaching the quantum degeneracy threshold of polaritons (32). Spontaneous build-up of circular polarization of the emitted light is also observed at the threshold (4; 33). We also make a comparison with a standard photon laser threshold to reveal the different physical origin of the two types of the threshold, and to demonstrate, as a proof of principle, that a polaritons condensate offers a very low threshold coherent light source (4).

Chapter 6 contains a more in depth, and original, study of various quantum statistical properties of polariton condensation. We demonstrate that a quantum mechanical pure state and macroscopic coherence gradually build up in the condensate (3). We observe a sharp shrinkage of the system size at the threshold density and an abnormally slow growth of the system size above the threshold density (4), which can be understood in terms of the system size dependence of the BEC critical density in two-dimensions. Finally, the microcavity system above the quantum degeneracy threshold — when properly tuned — evolves from a non-equilibrium gas to a quasi-thermal equilibrium Bose gas with a high effective temperature (4), and finally to a thermal-equilibrium gas described by a Bose-Einstein distribution with the same temperature as the phonon bath, and with a chemical potential close to zero (34). Correspondingly, the energy relaxation time of the system decreases to a value much shorter than the lifetime of the polaritons.

The three samples discussed in this dissertation are listed in appendix A. Appendix B includes a discussion of the quantum statistical origin of parametric amplification with both bosons and fermions, which is rather independent of the central

theme of the thesis.

Chapter 2

Bogoliubov Theory of BEC

BEC has been a source of imagination and innovation of physicists ever since its first proposal by Einstein in 1925 (35). It adds to the wonder if we remember that, in 1925, quantum theory was still at its infancy, the concepts of boson and fermion were non-existing. In fact, that was the time when modern quantum statistics was coming into being. The first application of BEC to a physical system was by London in 1938 (36), right after the discovery of superfluidity in liquid helium (37; 38). Throughout the decades, BEC has triggered intense theoretical work in the field of manybody physics, quantum phase transitions and atom physics. It also fostered the development of experimental techniques in quantum optics, in trapping and cooling of atoms, and in quantum optics and in growth and fabrication of semiconductors. Almost half a century later, in 1995, the first unambiguous realization of BEC was achieved in dilute atomic gasses (11; 12; 13). The effort devoted to atomic systems has harvested a modern branch of physics, (ultra-)cold atom physics, which continues to be a test-ground of theories and a cradle of novel applications.

In semiconductors, the grand challenge is still to obtain conclusive evidence of BEC and phase transitions alike for excitons and polaritons, and to understand and formulate the underlying physics appropriate for them. Before presenting our effort along this direction in polariton systems, we first review in this chapter the basic concepts of BEC in a very simplified form. For rigorous and comprehensive discussions of BEC theories, many excellent review papers and books are available (39; 40).

2.1 BEC of an Ideal Bose Gas

BEC of an ideal bose gas results directly from quantum statistics. In a grand canonical ensemble, at thermal equilibrium, the probability of a configuration with M_r particles and energy E_s is given by:

$$P_{r,s} = e^{\beta(\mu M_r - E_s)}/Z(\beta, \mu), \tag{2.1}$$

where $\beta = 1/k_B T$, T and μ are the temperature and chemical potential of the reservoir. $Z(\beta, \mu)$ is the grand partition function:

$$Z(\beta, \mu) = \sum_{N_i}^{\infty} \sum_s e^{\beta(\mu M_r - E_s)} \tag{2.2}$$

Applied to an ideal gas of indistinguishable particles distributed in 'microstates i' of energy ε_i and occupation number N_i in each state:

$$Z(\beta, \mu) = \sum_{M_r} e^{\beta(\mu \sum_i N_i - \sum_i \varepsilon_i N_i)} = \prod_i \sum_{N_i} e^{\beta(\mu - \varepsilon_i)N_i}. \tag{2.3}$$

In a Bose gas, $N_i = 0, 1, 2, ...,$

$$Z(\beta, \mu) = \prod_i (1 - e^{\beta(\mu - \varepsilon_i)}). \tag{2.4}$$

Using (2.4) we obtain the Bose-Einstein distribution function $f_{BE}(\varepsilon_i)$, the total particle number N, and the total internal energy of the gas $E(T, \mu)$:

$$f_{BE}(\varepsilon_i) = \bar{N}_i = -\frac{\partial}{\partial \beta \varepsilon_i} \ln Z = \frac{1}{\exp[\beta(\varepsilon_i - \mu)] - 1}, \tag{2.5}$$

$$N = -\frac{\partial}{\partial \mu}(k_B T \ln Z) = \sum_i \frac{1}{\exp[\beta(\varepsilon_i - \mu)] - 1}$$

$$= \sum_i f_{BE}(\varepsilon_i), \tag{2.6}$$

$$E(T, \mu) = \sum_i \varepsilon_i f_{BE}(\varepsilon_i) = \sum_i \frac{\varepsilon_i}{\exp[\beta(\varepsilon_i - \mu)] - 1}. \tag{2.7}$$

In a Fermi gas, $N_i = 0, 1$, leading to the Fermi-Dirac distribution:

$$f_{FD}(\varepsilon_i) = \frac{1}{\exp[\beta(\varepsilon_i - \mu)] + 1}. \tag{2.8}$$

In the limit $\mu \ll -k_B T$, $e^{-\beta\mu} \gg 1$, both distributions are approximated by the Maxwell-Bolzmann distribution:

$$f_{MB}(\varepsilon_i) = \exp(\beta\mu) \ \exp[-\beta\varepsilon_i], \tag{2.9}$$

which is the exact result calculated from (2.2) in the case of distinguishable particles.

The physical condition of $N_i \geq 0$ induces a unique constraint for a bose gas: $\mu \leq \varepsilon_0$ (ε_0 is the energy of the single-particle ground state). We also notice that f_{BE} monotonically increases with increasing μ. Hence, at given T, when μ approaches ε_0 from below, $f_{BE}(\varepsilon_i > \varepsilon_0)$ reaches a finite maxima, while $f_{BE}(\varepsilon_0)$ diverges. If we rewrite (2.6) as

$$N = f_{BE}(\varepsilon_0, T, \mu) + \sum_{i \neq 0} f_{BE}(\varepsilon_i, T, \mu) = N_0(T, \mu) + N'(T, \mu), \tag{2.10}$$

At given T, the total number of particles in all *excited* states can not exceed $N_c(T) \doteq N'(T, 0)$. It is straightforward to show that $N_c(T)$ is finite in dimensions larger than two for an infinite system, or a box with periodic boundary conditions. If $N > N_c(T)$, the difference all goes to the ground state $N_0(T) = N - N_c(T)$.

In the thermodynamic limit, ε_i becomes continuous, the number density vanishes for any excited state:

$$n_i \doteq N_i/V = f_{BE}(\varepsilon)\frac{\rho(\varepsilon)d\varepsilon}{V} \to 0, \quad \text{as } V \to 0. \tag{2.11}$$

The ground state $n_0 = \frac{N - N_c(T)}{V}$ becomes finite once $N > N_c(T)$. In another word, a macroscopic number of particles *condense* into the single microscopic ground state. This is the phenomenon of BEC.
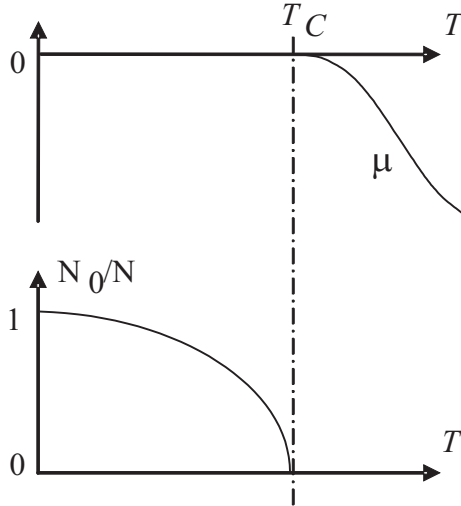
Figure 2.1: Illustration of condensate density n_0 and chemical potential μ v.s. temperature T,for a 3D bose gas with given density n

Take for example a free bose gas in 3D with mass m

$$n_c(T_c) = \frac{N'(T_c, 0)}{V} = \left(\frac{mk_BT_c}{2\pi\hbar^2}\right)^{\frac{3}{2}} \left(\frac{2}{\sqrt{\pi}} \int_0^\infty dx x^{\frac{1}{2}} \frac{1}{e^x - 1}\right), \qquad (2.12)$$

where we used $\varepsilon = p^2/2m$ and $x = \varepsilon/k_BT_c$. The integral is a Bose function, its value is 2.612; the term in front of it is the inverse cube of the thermal de Broglie wavelength:

$$\lambda_T(T) \doteq \sqrt{\frac{2\pi\hbar^2}{mk_BT}}. \qquad (2.13)$$

So we rewrite (2.12) as:

$$n_c = 2.612/\lambda_{T_c}^3 \quad \text{or,} \quad n_c\lambda_{T_c}^3 = 2.612. \qquad (2.14)$$

For given n, the condensate fraction $n_0/n = 1 - (T/T_c)^{3/2}$ at $T < T_c$, and $n_0/n = 0$ at $T \geq T_c$, as illustrated in figure 2.1

(2.14) shows that the phase transition takes place when the inter-particle spacing

is comparable with the particle's thermal de Broglie wavelength. In general we have

$$n_c \propto \lambda_T(T_c)^{-d}, \tag{2.15}$$

where d is the dimension. Hence for given particle density n, the critical temperature scales inversely proportional to the mass:

$$T_c \propto 2\pi\hbar^2 n_c^{-2/d} m^{-1}. \tag{2.16}$$

2.2   The 'Macroscopic' Ground State

To reveal the physical significance of a macroscopic n_0, we introduce the Bogoliubov theory which laid down the framework of the modern theory of BEC (41; 42; 43; 44). We first write down the Hamiltonian of a non-interacting bose gas in the formalism of second quantization:

$$\hat{H}_0 = \sum_i (\varepsilon_i - \mu)\hat{a}_i^\dagger \hat{a}_i, \tag{2.17}$$

where $\hat{a}_i$ and $\hat{a}_i^\dagger$ are the annihilation and creation operators a particle in state i. They obey the boson's commutation relations $[\hat{a}_i, \hat{a}_i^\dagger] = \delta_{ij}$ and $[\hat{a}_i, \hat{a}_j] = 0$. In the BEC phase,

$$[\frac{\hat{a}_0}{\sqrt{V}}, \frac{\hat{a}_0^\dagger}{\sqrt{V}}] = \frac{1}{V} \xrightarrow{V\to\infty} 0,$$

while at the same time

$$\langle \frac{\hat{a}_0}{\sqrt{V}} \cdot \frac{\hat{a}_0^\dagger}{\sqrt{V}} \rangle = \frac{N_0}{V} \to \text{finite}.$$

Hence $\hat{a}_0/\sqrt{V}$ and $\hat{a}_0^\dagger/\sqrt{V}$ behave like c-numbers, with a finite amplitude $\sqrt{N_0/V}$, and an arbitrary phase ϕ:

$$a_0 \approx \sqrt{N_0}e^{-i\phi}, \quad a_0^\dagger \approx \sqrt{N_0}e^{i\phi}.$$

If we operate a_0 on the ground state $|\Omega\rangle$:

$$a_0|\Omega\rangle \approx \sqrt{N_0}e^{-i\phi}|\Omega\rangle, \quad a_0^\dagger|\Omega\rangle \approx \sqrt{N_0}e^{i\phi}|\Omega\rangle \tag{2.18}$$

It means that when there is a macroscopic number of particles condensed in the ground state, adding or removing one particle from the condensate leaves the system physically unchanged. Replacing the ground state operators by c-numbers as in (2.2) is the first crucial step in Bogoliubov's theory, it is usually called the 'Bogoliubov approximation'. (2.18) also implies that $|\Omega\rangle$ behaves like an eigenstate of a_0, i.e., a coherent state.

2.3   The Order Parameter and Off Diagonal Long Range Order

Formally, consider an infinite uniform system, we define the Bose field operator $\Psi(\boldsymbol{r})$ as the order parameter of BEC:

$$\Psi(\boldsymbol{r}) = \frac{1}{\sqrt{V}}\sum_i \hat{a}_i e^{i\boldsymbol{p}_i\boldsymbol{r}} = \frac{a_0 e^{i\boldsymbol{p}_0\boldsymbol{r}}}{\sqrt{V}} + \frac{1}{\sqrt{V}}\sum_{i\neq 0}\hat{a}_i e^{i\boldsymbol{p}_i\boldsymbol{r}}$$

$$= \Psi_0(\boldsymbol{r}) + \Psi_T(\boldsymbol{r}), \tag{2.19}$$

where $\boldsymbol{r}$ is distance, and $\boldsymbol{p}_i$ is the momentum of the state i. $\Psi_T(\boldsymbol{r})$ consists of terms of the excited states. In the thermodynamic, $V \to \infty$, $\Psi_T(\boldsymbol{r})$ vanishes for $r > 0$. $\Psi_0(\boldsymbol{r})$ is the ground state term. In a condensed phase, $\Psi_0(\boldsymbol{r})$ has a finite and constant amplitude given by the square root of the condensate fraction.

The off-diagonal element of the first reduced density matrix of $\Psi(\boldsymbol{r})$ is:

$$\rho_1(\boldsymbol{r}, \boldsymbol{r}') = < \Psi^\dagger(\boldsymbol{r}')\Psi(\boldsymbol{r}) > = < \Psi_0^\dagger(\boldsymbol{r}')\Psi_0(\boldsymbol{r}) > + < \Psi_T^\dagger(\boldsymbol{r}')\Psi_T(\boldsymbol{r}) >$$
$$= \frac{N_0}{V} e^{i\boldsymbol{p}_0(\boldsymbol{r}-\boldsymbol{r}')} + \frac{1}{V} \sum_{i \neq 0} \langle \hat{a}_i^+ \hat{a}_i \rangle e^{i\boldsymbol{p}_i(\boldsymbol{r}-\boldsymbol{r}')}. \qquad (2.20)$$

$\rho_1(\boldsymbol{r}, \boldsymbol{r}')$ describes the correlation for generating of a particle at position $\boldsymbol{r}$ and annihilation of one at $\boldsymbol{r}'$. We again can separate it into terms of the excited states and a term from the ground state. When $|\boldsymbol{r} - \boldsymbol{r}'| \to \infty$, the phase $\boldsymbol{p}_i(\boldsymbol{r} - \boldsymbol{r}')$ of the excited-state terms become random, and the summation of these terms vanishes when $V \to \infty$. The ground-state term, however, has a finite and constant amplitude of $0 < n_0 \leq n$ in the BEC phase regardless of the separation $|\boldsymbol{r} - \boldsymbol{r}'|$. Hence $|\rho_1(\boldsymbol{r}, \boldsymbol{r}')| = n_0 = |\Psi_0|^2$ is finite and uniform even over macroscopic distances. This character of BEC is called the off-diagonal long range order (ODLRO). It serves as a measure of macroscopic coherence and an important criterion for BEC.

2.4 'Genuine' BEC of Interacting Bosons

So far, the theory is based on a non-interacting Bose gas, it predicts a BEC transition when a macroscopic number of particles condense into the ground state. The condensate can be described by a single-particle wavefunction, and is coherent over macroscopic distances. However, it is not clear if the predicted BEC corresponds to physical reality. For example, there is no physical mechanism to prevent condensate fragmentation into nearly-degenerate states, or to establish correlations among the condensed particles. These problems can be addressed when we include particle interactions (Nozière, reference (10)).

Consider the simplest type of scalar interaction:

$$U = \frac{1}{2V} \sum_{p,k,q} U_q \hat{a}_{\boldsymbol{p}+\boldsymbol{q}}^\dagger \hat{a}_{\boldsymbol{k}-\boldsymbol{q}}^\dagger \hat{a}_{\boldsymbol{k}} \hat{a}_{\boldsymbol{p}}.$$

If particles condense into two nearly degenerate states with occupancies N_1 and $N_2 =$

$N - N_1$, we have the ground state wavefunction and energy:

$$|\psi_0\rangle = \frac{1}{\sqrt{N_1!N_2!}}(\hat{a}_1^{\dagger N_1}\hat{a}_2^{\dagger N_2})|vac\rangle$$

$$E_0 = \frac{1}{2}U_0[N_1(N_1 - 1) + N_2(N_2 - 1) + 2U_0N_1N_2] + U_{p_1-p_2}N_1N_2$$

$$= \frac{1}{2}U_0N(N - 1) + U_0N_1N_2. \tag{2.21}$$

The first term in (2.21) consists of the self-interaction and Hartree forward scattering energies, the second term comes from the exchange interaction between particles. Note that U_0 has to be a positive (i.e. repulsive) potential otherwise the system will collapse. Hence the ground state energy is minimized when the Fock term is zero, i.e., $N_1 = 0, N_2 = N$ or vice versa. In another words, repulsive interactions prevent condensate fragmentation. Genuine BEC takes place only in a Bose gas with repulsive interactions.

The above analysis is the same if $|\psi_0\rangle$ is written as a coherent state $\exp(\phi\,\hat{a}_0^{\dagger})|vac\rangle$ instead of a number state, where $\phi = \sqrt{N_0}\,e^{i\theta}$ (Eq.(2.18)). Either way, $|\psi_0\rangle$ is the ground state wavefunction for a free bose gas. We naturally expect that the ground state shall be modified when interactions are taken into account. As a trial wavefunction, we consider:

$$|\psi_0\rangle = \exp(\phi\,\hat{a}_0^{\dagger} + \lambda_p\,\hat{a}_p^{\dagger}\hat{a}_{-p}^{\dagger})|vac\rangle.$$

It includes virtual excitation of a pair of particles out of the condensate, a process described by interaction terms like $\hat{a}_p^{\dagger}\hat{a}_{-p}^{\dagger}\hat{a}_0\hat{a}_0 + c.c.$ Using (2.4) to compute E_0, we obtain the usual Hartree and Fock terms with corrections of the order $U_0|\lambda_p|^2$ and $U_p|\lambda_p|^2$. In addition, a new macroscopic term emerges:

$$\Delta E_0 = \sum_p U_p\langle\hat{a}_0^{\dagger}\hat{a}_0^{\dagger}\rangle\langle\hat{a}_p\hat{a}_{-p}\rangle \sim \sum_p \phi \cdot \lambda_p \tag{2.22}$$

Hence the ground state energy is lowered by an macroscopic amount of when the phase is locked between ϕ and λ_p: $\Delta E_0 \sim -\sqrt{N_0}\sum|\lambda_p|$. It is the two-body interaction that

leads to phase locking among particles in the condensate.

2.5   BEC of a Dilute Weakly Interacting Bose Gas

The Hamiltonian including the two-body interactions is:

$$\hat{H} = \sum_{\bm{p}}(\varepsilon_{\bm{p}} - \mu)\hat{a}_{\bm{p}}^{\dagger}\hat{a}_{\bm{p}} + \frac{1}{2V}\sum_{\bm{p},\bm{k},\bm{q}} U_q \hat{a}_{\bm{p}+\bm{q}}^{\dagger}\hat{a}_{\bm{k}-\bm{q}}^{\dagger}\hat{a}_{\bm{k}}\hat{a}_{\bm{p}},$$

where U_q is the interaction potential. Interactions involving three or more particles are neglected under the assumption that the gas is dilute, i.e., $n|a|^3 \ll 1$, a defined as the s-wave scattering length of the gas. Replacing $\hat{a}_0^{\dagger}$ and $\hat{a}_0$ by $\sqrt{N_0}$ according to the Bogoliubov approximation (2.2) and let $n_0 = N_0/V$, we obtain:

$$
\begin{aligned}
\hat{H} =& \hat{H}_0 + \hat{H}_1 \\
\hat{H}_0 =& \frac{1}{2}n_0^2 U_0 V + \sum_{\bm{p}\neq 0}[(\varepsilon_{\bm{p}} - \mu) + n_0 U_0 + n_0 U_{\bm{p}}]\hat{a}_{\bm{p}}^{\dagger}\hat{a}_{\bm{p}} \\
& + \sum_{\bm{p}\neq 0}\frac{n_0 U_{\bm{p}}}{2}(\hat{a}_{\bm{p}}^{\dagger}\hat{a}_{-\bm{p}}^{\dagger} + \hat{a}_{\bm{p}}\hat{a}_{-\bm{p}}) \\
\hat{H}_1 =& \sum_{\bm{p},\bm{q}\neq 0}\frac{\sqrt{n_0}U_{\bm{q}}}{2\sqrt{V}}(\hat{a}_{\bm{p}+\bm{q}}^{\dagger}\hat{a}_{\bm{q}}\hat{a}_{\bm{p}}^{\dagger} + \hat{a}_{\bm{p}+\bm{q}}^{\dagger}\hat{a}_{-\bm{q}}^{\dagger}\hat{a}_{\bm{p}}) + \sum_{\bm{p},\bm{q}\neq 0}\frac{U_q}{2V}\hat{a}_{\bm{p}+\bm{q}}^{\dagger}\hat{a}_{\bm{k}-\bm{q}}^{\dagger}\hat{a}_{\bm{k}}\hat{a}_{\bm{p}} + \cdots
\end{aligned}
\tag{2.23}
$$

In the thermodynamic limit, $V \to \infty$, $N_i/V \to 0$ for $i \neq 0$ while n_0 is finite. Hence $\langle \hat{H}_1 \rangle \propto O(1/\sqrt{V}) \to 0$ while $\langle \hat{H}_0 \rangle \propto O(n_0)$, and the Hamiltonian of the BEC gas reduces to $\hat{H}_0$. The first term in $\hat{H}_0$ is the self-energy of the particles condensed into $\bm{p}_0 = 0$, it amounts to an offset of the ground state energy of the system. The second term in $\hat{H}_0$ correspond to the Hartree and Fork energies due to interactions between particles at $\bm{p}_0$ and at $\bm{p} \neq \bm{p}_0$, its expectation value is of the order n_0. The third term in $\hat{H}_0$, also of the order n_0, is an unconventional term unique to a BEC gas, it violates the particle number conservation! Physically it corresponds to the excitation/absorbtion of a pair of particles at opposite $|\bm{p}|$ from/by the condensate. The condensate serves as a macroscopic reservoir, adding or removing a pair from the condensate leaves it in the same state.

$\hat{H}_0$ is quadratic in $\hat{a}_{\boldsymbol{p}}$ and $\hat{a}_{\boldsymbol{p}}^{\dagger}$, it can be diagonalized by the 'Bogoliubov transformation':

$$\hat{a}_{\boldsymbol{p}} = u_{\boldsymbol{p}}\hat{b}_{\boldsymbol{p}} - v_{-\boldsymbol{p}}^{*}\hat{b}_{-\boldsymbol{p}}^{\dagger}, \quad \hat{a}_{\boldsymbol{p}}^{\dagger} = u_{\boldsymbol{p}}^{*}\hat{b}_{\boldsymbol{p}}^{\dagger} - v_{-\boldsymbol{p}}\hat{b}_{-\boldsymbol{p}}. \tag{2.24}$$

If $u_p = u_{-p}$, $v_p = v_{-p}$, and $|u_{\boldsymbol{p}}|^2 - |v_{-\boldsymbol{p}}|^2 = 1$, the new set of operators $\hat{b}_{\boldsymbol{p}}$ and $\hat{b}_{\boldsymbol{p}}^{\dagger}$ also satisfy the bose commutation relations and $[\hat{b}_i, \hat{b}_j] = 0$, $[\hat{b}_i, \hat{b}_j^{\dagger}] = \delta_{ij}$. The solution is found to be:

$$\hat{H}_0 = E_0 + \sum \omega(\boldsymbol{p})\hat{b}_{\boldsymbol{p}}^{\dagger}\hat{b}_{\boldsymbol{p}}, \tag{2.25}$$

$$\omega(\boldsymbol{p}) = \sqrt{\varepsilon_{\boldsymbol{p}}^2 + 2n_0 U_{\boldsymbol{p}}\,\varepsilon_{\boldsymbol{p}}}, \tag{2.26}$$

$$E_0 = \frac{1}{2}\sum_{\boldsymbol{p}}[\omega(\boldsymbol{p}) - \varepsilon_{\boldsymbol{p}} - n_0 U_{\boldsymbol{p}}] + \frac{n_0^2 U_0 V}{2}, \tag{2.27}$$

$$\mu = \frac{\partial E_0}{\partial N_0} = n_0 U_0, \tag{2.28}$$

$$u_{\boldsymbol{p}} = \left(\frac{\varepsilon_{\boldsymbol{p}} + n_0 U_{\boldsymbol{p}}}{2\omega(\boldsymbol{p})} + \frac{1}{2}\right)^{\frac{1}{2}}, \tag{2.29}$$

$$v_{-\boldsymbol{p}} = \left(\frac{\varepsilon_{\boldsymbol{p}} + n_0 U_{\boldsymbol{p}}}{2\omega(\boldsymbol{p})} - \frac{1}{2}\right)^{\frac{1}{2}}. \tag{2.30}$$

E_0 is the energy of the true ground state $|vac\rangle$ defined by $\hat{b}_{\boldsymbol{p}}|vac\rangle = 0$ for any $\boldsymbol{p} \neq \boldsymbol{p}_0$. $\hat{b}_{\boldsymbol{p}}^{\dagger}|vac\rangle$ creates an elementary excitation of the system with eigenenergy $\omega(\boldsymbol{p})$ given in (2.26).

(2.26) is the famous 'Bogoliubov dispersion' of BEC. In a dilute gas where $na^3 \ll 1$, most excitations are within an energy range $\varepsilon_{\boldsymbol{p}} \ll n_0 U_{\boldsymbol{p}}$. For those low energy excitations,

$$\omega(\boldsymbol{p}) \simeq \sqrt{n_0 U_{\boldsymbol{p}}/m}\,|\boldsymbol{p}| \simeq \sqrt{n_0 U_0/m}\,|\boldsymbol{p}|. \tag{2.31}$$

The dispersion becomes phonon-like with a sound velocity:

$$u_c \doteq \sqrt{U_0 n_0/m} \tag{2.32}$$

These phonon-like modes are called the Bogoliubov quasi-particles, or, the Goldstone modes.

2.6 BEC and Superfluidity

An important implication of the phonon-like low energy excitation is that, BEC often exhibits superfluidity. Consider the condensate moving at a velocity $\boldsymbol{v}_s = \boldsymbol{p}_0/m$ relative to a wall, friction is produced if and only if spontaneous excitations of the quasi-particles lower the energy of the BEC gas. In a reference frame that the wall is at rest, the energy of a single excitation is given by the Galilean transformation: $\omega'(\boldsymbol{p}) = \omega(\boldsymbol{p}) + \boldsymbol{v}_s \cdot \boldsymbol{p}$. If $\omega'(\boldsymbol{p}) > 0$ for all $\boldsymbol{p}$, there is no spontaneous energy dissipation of the system, the system is a frictionless superfluid. This gives the Landau's criterion for superfluidity:

$$v_s < v_c = \min_{\boldsymbol{p}} \frac{\omega(\boldsymbol{p})}{p} \tag{2.33}$$

BEC with dispersion (2.31) satisfies the above criterion when $v < v_c$.

The BEC order parameter $|\Psi_0|e^{i\theta}$ is not invariant under the Galilean transformation due to the phase factor $i\theta$ (which breaks the gauge symmetry). In a uniform system, the amplitude of $|\Psi_0|$ is a constant, and the phase factor transforms as (40):

$$S = -\frac{\mu t}{\hbar} \quad \rightarrow \quad S = \frac{1}{\hbar} \left[m\boldsymbol{v}_s \cdot \boldsymbol{r} - \left(\frac{1}{2}mv_s^2 + \mu \right) t \right], \tag{2.34}$$

Hence the superfluid velocity is proportional to the gradient of the phase:

$$\boldsymbol{v}_s = \frac{\hbar}{m}\nabla S \tag{2.35}$$

Note that although BEC often implies superfluidity and vice versa, these are two distinct phenomena. For example, BEC in disordered materials exhibits no superfluidity; Kosterlitz-Thouless phase in 2D is an example of superfluidity without BEC.

2.7   Peculiarities of 2D

In dimensions $d \leq 2$, in the thermodynamic limit, the critical density defined in (2.10) diverges when $\mu \to 0$. It was rigorously proven that in $d = 2$ with a constant energy density of state, long wavelength thermal fluctuation of the phase destroys a long range order (45; 46), and BEC is absent at any temperature $T > 0$. BEC does exist at $T = 0$ where there is only quantum phase fluctuations.

However, phase fluctuation does not necessarily destroy superfluidity. In 2D, it's the thermal excitation of vortices which destroys superfluidity. This leads to a new type of phase transition in 2D, the Kosterlitz-Thouless transition, with a critical temperature:

$$k_B T_{KT} = n_s \frac{\pi \hbar^2}{2m^2},$$
(2.36)

where n_s is the superfluid density. Equation 2.36 can also be written in terms of the thermal de Broglie wavelength defined in (2.13): $n_s \lambda_{T_c}^2 = 4$. Above T_{KT}, vortices are thermally excited and produce friction, as a result, n_s and the number of vortices are exponentially small. Below T_{kT}, single vortices are energetically costly, hence they bind to form pairs and cluster, with a total binding number equal to zero, allowing percolation of condensate droplets in which a phase coherent path exists between two distant points. Hence n_s jumps to a non-zero value. The superfluid is described by the same Bogoliubov theory for weakly interacting bosons, and follow the Bogoliubov quasi-particle dispersion $\omega(\boldsymbol{p})$ in (2.26). The superfluid density n_s is related to the normal fluid density n_n and total density n by the Landau formula derived in the framework of *two-fluid model* (see for example reference (47)):

$$n = n_n + n_s,$$
(2.37)

$$n_n = \int d^2\boldsymbol{p} \; \rho(p) \; \omega(\boldsymbol{p}) \left[-\frac{\partial f_{BE}(\omega(\boldsymbol{p}, T, \mu = 0))}{\partial \omega(\boldsymbol{p})} \right],$$
(2.38)

where $\rho(p)$ is the density of states.

A BEC transition at finite temperature is recovered in 2D if the bose gas in confined by a spatially varying potential $U \sim r^\eta$. In this case, the density of states

becomes $\rho(E) \sim \varepsilon^{2\eta}$, and the integral in (2.10) converges for $\eta > 0$, leading to a finite critical temperature for BEC phase transition:

$$k_B T_c^{2D} \sim (n/m)^{\eta/(2+\eta)}. \tag{2.39}$$

Practically, any experimental system is of finite size and with finite number of particles. With discrete energy levels ε_i (i=1,2,...), finite total particle number N, and finite size $S = L^2$, the critical condition defined in (2.12) can be modified as:

$$\mu = \varepsilon_1; \tag{2.40}$$

$$n_c = \frac{1}{S} \sum_{i \geq 2} \frac{1}{e^{\varepsilon_i/k_B T} - 1}. \tag{2.41}$$

Thus defined critical condition can be fulfilled at $T_c > 0$ even in a 2D box system of size L. The critical density is:

$$n_c = \frac{2}{\lambda_t^2} \ln(\frac{L}{\lambda_t}), \tag{2.42}$$

where λ_t is the thermal de Broglie wavelength. If the particle number N is sufficiently large, the transition shows similar features as a BEC transition defined at the thermodynamic limit (48).

2.8 Summary

In summary, we reviewed that BEC is characterized by a macroscopic order parameter, and the existence of macroscopic coherence, or, off-diagonal-long-range order. Interactions are necessary to form a genuine BEC, they establish the ODLRO, leads to a sharply peaked distribution in the momentum-space, and phonon-like low-energy excitations. In 2D, BEC is absent in the thermodynamic limit but survives in a finite system. And a KT transition is predicted for 2D where a superfluid forms.

In the next chapter, we introduce the microcavity polariton system and study its uniqueness as a system for BEC research.

Chapter 3

Microcavity Polaritons

A very elegant and unique physical entity, 'microcavity polariton' is a 'quasi-particle' resulting from 'strong-coupling between light and matter'. 'Quasi-particle' is a powerful concept that describes the formidable complications of the real world with misleading simplicity. Light and matter coupling, enhanced and controlled by carefully engineered cavities, marries the solid state devices to optical access and opens a world of discovery and innovation ranging from fundamental problems in cavity quantum electrodynamics to daily applications like laser pointers. Naturally, microcavity polariton has spurred intense interest, from both scientific and application perspectives, ever since its discovery in 1992 (5).

This chapter is to explain the question what are semiconductor excitons and polaritons.

3.1   Wannier-Mott Exciton

A solid consists of 10^{23} atoms. Instead of describing the 10^{23} atoms and their constituents in full detail, the common approach is to treat the stable ground state of an isolated system as a quasi-vacuum — the state with filled valence band and empty conduction band for a semiconductor — and to introduce quasi-particles as a unit of elementary excitation, which only weakly interact with each other. An exciton is a typical example of such a quasi-particle, consisting of an electron and a hole bound

by the Coulomb interaction. The quasi-vacuum of a semiconductor is the state with filled valence band and empty conduction band. When an electron with charge $-e$ is excited from the valence band into the conduction band, the vacancy it leaves in the valence band can be described as a quasi-particle called a 'hole'. A hole in the valence band has charge $+e$, and an effective mass defined by $-(\frac{\partial^2 E}{\partial p^2})^{-1}$. A hole and an electron at $p \sim 0$ interacts with each other via Coulomb interaction and form a bound pair — an exciton — analogous to a hydrogen atom where an electron is bound to a proton. The envelope wavefunction of an exciton is also analogous to that of a hydrogen atom. However, due to the strong dielectric screening in solids and a small effective mass ratio of the hole to the electron, the binding energy of an exciton in GaAs is on the order of 10 meV, three orders of magnitude smaller than that of hydrogen atoms, and the radius of an exciton is about 10^2 Å, extending over tens of atomic sites in the crystal (Wannier-Mott exciton).

Following Hanamura and Haug (reference (49)), the Hamiltonian of the electronic system of a direct two-band semiconductor is:

$$\hat{H} = \int d^3\boldsymbol{x}\hat{\psi}^\dagger(\boldsymbol{x})\hat{H}_0(\boldsymbol{x})\hat{\psi}^\dagger(\boldsymbol{x}) + \frac{1}{2}d^3\boldsymbol{x}d^3\boldsymbol{y}\hat{\psi}^\dagger(\boldsymbol{x})\hat{\psi}^\dagger(\boldsymbol{y})\hat{V}(\boldsymbol{x}-\boldsymbol{y})\hat{\psi}(\boldsymbol{x})\hat{\psi}(\boldsymbol{y}), \qquad (3.1)$$

where $\hat{H}_0(\boldsymbol{x})$ is the Hamiltonian of single electrons, $\hat{V}(\boldsymbol{x}) = e^2/\epsilon|\boldsymbol{x}|$ is the screened Coulomb potential, and ψ is the field operator for electrons expanded in terms of the electron eigenfunctions $\psi_{\boldsymbol{k}j}(\boldsymbol{x})$:

$$\hat{\psi}(\boldsymbol{x}) = \sum_{j=c,v;\boldsymbol{k}} \hat{a}_{\boldsymbol{k}j}\psi_{\boldsymbol{k}j}(\boldsymbol{x})$$

$$\psi_{\boldsymbol{k}j}(\boldsymbol{x}) = u_{\boldsymbol{k}j}(\boldsymbol{x})\exp(i\boldsymbol{k}\cdot\boldsymbol{x})/\sqrt{N}. \qquad (3.2)$$

Here $j = c, v$ denotes the conduction or valence band, $u_{\boldsymbol{k}j}(\boldsymbol{x})$ is the Bloch wavefunction and N is the number of unit cells of the lattice. $\hat{a}_{\boldsymbol{k}j}$ is the fermionic annihilation operator for an electron. It obeys the commutation relations $\{\hat{a}_{\boldsymbol{k}}, \hat{a}_{\boldsymbol{l}}^\dagger\} = \delta_{\boldsymbol{k},\boldsymbol{l}}$ and $\{\hat{a}_{\boldsymbol{k}j}, \hat{a}_{\boldsymbol{l}j}\} = 0$. For the valence band, we introduce the hole creation operator $\hat{b}_{-\boldsymbol{k}}$ to

replace the electron annihilation operator:

$$\hat{a}^{\dagger}_{\boldsymbol{k}v} = \hat{b}_{-\boldsymbol{k}}. \tag{3.3}$$

Annihilation of a valence band electron in a state with a wavevector $\boldsymbol{k}$, spin σ, charge $-e$ and kinetic energy $-E(k)$ from the top of the valence band is equivalent to creation of a hole in state $-\boldsymbol{k}$ with flipped spin $\bar{\sigma}$, positive charge $+e$ and kinetic energy $E(k)$. For the conduction band, we can now simplify the denotation as:

$$\hat{a}_{\boldsymbol{k}c} = \hat{a}_{\boldsymbol{k}}. \tag{3.4}$$

Substitute (3.2) to (3.4) into (3.1), neglecting number non-conserving terms, we obtain:

$$
\begin{aligned}
\hat{H} =& \sum E_e(k)\hat{a}^{\dagger}_k \hat{a}_k + \sum E_h(k)\hat{b}^{\dagger}_k \hat{b}_k \\
&+ \frac{1}{2}\sum V^{c\,c\,c\,c}_{\boldsymbol{k}_1 \boldsymbol{k}_2 \boldsymbol{k}_3 \boldsymbol{k}_4} \hat{a}^{\dagger}_{\boldsymbol{k}_1} \hat{a}^{\dagger}_{\boldsymbol{k}_2} \hat{a}_{\boldsymbol{k}_3} \hat{a}_{\boldsymbol{k}_4} + \frac{1}{2}\sum V^{v\;\;v\;\;v\;\;v}_{-\boldsymbol{k}_1 -\boldsymbol{k}_2 -\boldsymbol{k}_3 -\boldsymbol{k}_4} \hat{b}^{\dagger}_{\boldsymbol{k}_1} \hat{b}^{\dagger}_{\boldsymbol{k}_2} \hat{b}_{\boldsymbol{k}_3} \hat{b}_{\boldsymbol{k}_4} \\
&- \sum \left(V^{c\,v\,v\,c}_{\boldsymbol{k}_1 \boldsymbol{k}_3 \boldsymbol{k}_2 \boldsymbol{k}_4} - V^{c\,v\,c\,v}_{\boldsymbol{k}_1 \boldsymbol{k}_3 \boldsymbol{k}_4 \boldsymbol{k}_2} \right) \hat{a}^{\dagger}_{\boldsymbol{k}_1} \hat{b}^{\dagger}_{\boldsymbol{k}_2} \hat{b}_{\boldsymbol{k}_3} \hat{a}_{\boldsymbol{k}_4}. \tag{3.5}
\end{aligned}
$$

In the effective mass approximation, $E_e(k)$ ($E_h(k)$) are the kinetic energies of an electron (a hole) with effective mass m_e (m_h):

$$
\begin{aligned}
E_e(k) &= E_g + \frac{\hbar^2 k^2}{2m_e}, \\
E_h(k) &= \frac{\hbar^2 k^2}{2m_h}, \tag{3.6}
\end{aligned}
$$

where E_g is the bandgap energy. $V^{i\,j\,m\,n}_{\boldsymbol{k}_1 \boldsymbol{k}_2 \boldsymbol{k}_3 \boldsymbol{k}_4}$ are the direct and exchange interactions among electrons and holes due to the Coulomb potential $\hat{V}$:

$$V^{i\,j\,m\,n}_{\boldsymbol{k}_1 \boldsymbol{k}_2 \boldsymbol{k}_3 \boldsymbol{k}_4} = \langle \boldsymbol{k}_1 i, \boldsymbol{k}_2 j | \hat{V} | \boldsymbol{k}_3 m, \boldsymbol{k}_4 n \rangle \qquad (i, j, m, n = c, v), \tag{3.7}$$

For Wannier-Mott excitons, the plane wave factor in (3.2) and the Coulomb potential $\hat{V}$ are slowly varying functions which change very little in one unit cell of the lattice,

hence (3.7) can be calculated by first integrating the Bloch functions in a unit cell Ω_i, then summing over all unit cells weighted by the planar wave factors. We also notice that:

$$\int_{v_i} d^3\boldsymbol{x} u^*_{\boldsymbol{k}\approx 0,c}(\boldsymbol{x}) u_{\boldsymbol{k}\approx 0,c}(\boldsymbol{x}) \approx 1$$
$$\int_{v_i} d^3\boldsymbol{x} u^*_{\boldsymbol{k}\approx 0,c}(\boldsymbol{x}) u_{\boldsymbol{k}\approx 0,v}(\boldsymbol{x}) \approx 0. \tag{3.8}$$

And we find that (3.7) can be simplified to a form, for example:

$$V^{cv}_{\boldsymbol{k}-\boldsymbol{l}'}{}^{v}_{-\boldsymbol{k}'}{}^{c}_{\boldsymbol{l}} = \frac{1}{V^2}\int d^3\boldsymbol{x} d^3\boldsymbol{y} \exp[i(\boldsymbol{l}-\boldsymbol{k})\cdot\boldsymbol{x} + i(\boldsymbol{l}'-\boldsymbol{k}')\cdot\boldsymbol{y}]\frac{e^2}{\epsilon|\boldsymbol{x}-\boldsymbol{y}|}. \tag{3.9}$$

Now we consider the general wavefunction of an electron-hole state:

$$|p\rangle = \sum C_{\boldsymbol{k}\boldsymbol{k}'}\hat{a}^\dagger_{\boldsymbol{k}}\hat{b}^\dagger_{\boldsymbol{k}'}|vac\rangle, \tag{3.10}$$

where $|vac\rangle$ is the quasi-vacuum with a full valence band and an empty conduction band. From the eigenvalue equation $H|p\rangle = E|p\rangle$, we obtain the equation for the amplitude $C_{\boldsymbol{k}\boldsymbol{k}'}$:

$$(E_e(k) + E_h(k') - E)C_{\boldsymbol{k}\boldsymbol{k}'} - \sum_{\boldsymbol{l}\boldsymbol{l}'}(V^{cv}_{\boldsymbol{k}-\boldsymbol{l}'}{}^{v}_{-\boldsymbol{k}'}{}^{c}_{\boldsymbol{l}} - V^{cv}_{\boldsymbol{k}-\boldsymbol{l}'}{}^{c}_{-\boldsymbol{l}}{}^{v}_{-\boldsymbol{k}'})C_{\boldsymbol{l}\boldsymbol{l}'} = 0 \tag{3.11}$$

Taking a Fourier transform of (3.11), using (3.7)–(3.9), we obtain the Wannier equations for an exciton (50):

$$\hat{H}_{exc}\phi(\boldsymbol{x}_e, \boldsymbol{x}_h) = E\phi(\boldsymbol{x}_e, \boldsymbol{x}_h),$$
$$\hat{H}_{exc} = -\frac{\hbar^2}{2m_e}\nabla_e - \frac{\hbar^2}{2m_h}\nabla_h + E_g - \frac{e^2}{\epsilon|\boldsymbol{x}_e - \boldsymbol{x}_h|}. \tag{3.12}$$

The two particle wavefunction is related to the amplitudes $C_{\boldsymbol{k}\boldsymbol{k}'}$ by

$$\phi(\boldsymbol{x}_e, \boldsymbol{x}_h) = \sum C_{\boldsymbol{k}\boldsymbol{k}'}\exp(i\boldsymbol{k}\cdot\boldsymbol{x}_e + i\boldsymbol{k}'\cdot\boldsymbol{x}_h). \tag{3.13}$$

We separate the center of mass motion and the relative motion by introducing the new coordinates:

$$\boldsymbol{r} = \boldsymbol{x}_e - \boldsymbol{x}_h, \quad \boldsymbol{R} = \beta_e \boldsymbol{x}_e - \beta_h \boldsymbol{x}_h, \tag{3.14}$$

where $\beta_e = m_e/M, \quad \beta_h = m_h/M, \quad M = m_e + m_h$. Then (3.13)become:

$$\phi(\boldsymbol{x}_e, \boldsymbol{x}_h) = \phi_n(\boldsymbol{r}) \exp(i\boldsymbol{K} \cdot \boldsymbol{R})/\sqrt{V}, \tag{3.15}$$

and the equation of relative motion is:

$$\left(-\frac{\hbar^2}{2m_r} \nabla_r - \frac{e^2}{\epsilon_0 r} + \varepsilon_{exc,n} \right) \phi_n(\boldsymbol{r}) = 0, \tag{3.16}$$

It has the same form as the equation of relative motion for a Hydrogen atom, but the reduced mass $m_r = m_e m_h/M$ is normally four orders of magnitude less than the hydrogen atom mass, and the Coulomb interaction is screened and reduced by a factor of ϵ_0. These lead to a much larger Bohr radius and much weaker binding energy of an exciton compared to an hydrogen atom. The total energy of the pair is:

$$E(K,n) = E_g - \varepsilon_{exc,n} + \frac{\hbar^2 K^2}{2M}, \tag{3.17}$$

The binding energy of the $1s$ state is:

$$E_B^{3D} \doteq \varepsilon_{exc,1} = \frac{\hbar^2}{2m_r a_B^2 n^2}, \tag{3.18}$$

and the Bohr radius of the 1s exciton is:

$$a_B^{3D} = \frac{\hbar^2 \epsilon_0}{e^2 m_r}. \tag{3.19}$$

Now the exciton operator $\hat{e}_{\boldsymbol{K},n}^{\dagger}$ can be defined by inserting (3.13)-(3.15) into (3.10)

and using $|p\rangle = \hat{e}^{\dagger}_{\boldsymbol{K},n}|vac\rangle$. We obtain:

$$\hat{e}^{\dagger}_{\boldsymbol{K},n} = \sum_{\boldsymbol{k},\boldsymbol{k}'} \delta_{\boldsymbol{K},\boldsymbol{k}+\boldsymbol{k}'}\phi_n(\beta_h\boldsymbol{k} - \beta_e\boldsymbol{k}')\hat{a}^{\dagger}_{\boldsymbol{k}}\hat{b}^{\dagger}_{\boldsymbol{k}'}, \qquad (3.20)$$

where $\phi_n(\boldsymbol{k})$ is the Fourier transform of $\phi_n(\boldsymbol{x})$. The commutation relations of the exciton operators are:

$$[\hat{e}_{\boldsymbol{K}',n'}, \hat{e}_{\boldsymbol{K},n}] = 0$$

$$[\hat{e}^{\dagger}_{\boldsymbol{K}',n'}, \hat{e}^{\dagger}_{\boldsymbol{K},n}] = 0$$

$$[\hat{e}_{\boldsymbol{K}',n'}, \hat{e}^{\dagger}_{\boldsymbol{K},n}] = \delta_{\boldsymbol{K}\boldsymbol{K}'}\delta_{nn'} - O(n_{exc}a_B^3). \qquad (3.21)$$

Hence excitons can be considered as bosons in the low density regime when $n_{exc} \ll a_B^{-3}$, or, when the exciton inter-particle spacing is much larger than its Bohr radius.

3.2 Exciton Optical Transition

The electron and hole in an exciton form a dipole which interacts with electromagnetic fields of light. The interband optical transition matrix element is given by the Fermi's golden rule:

$$W_{cv} = \frac{2\pi}{\hbar}\sum_{f,i}|\langle f|\hat{H}_I|i\rangle|^2\delta(E_f - E_i - \hbar\omega), \qquad (3.22)$$

where i and f denotes the initial and final states with energies E_i and E_f respectively. $\hbar\omega$ is the photon energy, and $\hat{H}_I$ is the dipole interaction Hamiltonian. We first consider an uncorrelated electron-hole pair, the matrix element is given by:

$$M \doteq |\langle f|\hat{H}_I|i\rangle| = \delta_{\sigma,j_e-j_h}\int_V \chi^*_{ck_e}(\boldsymbol{r})u^*_{ck_e}(\boldsymbol{r})e\boldsymbol{r}\cdot\boldsymbol{E}u_{vk_h}(\boldsymbol{r})\chi_{vk_h}(\boldsymbol{r}), \qquad (3.23)$$

where σ is the polarization of light, j_e and j_h are the angular momenta of the electron and hole, χ_{ck_e} and χ_{vk_h} are the envelope functions, and u_{ck_e} and u_{vk_h} are the Bloch functions. Since χ_{ck_e,vk_h} vary little within a unit cell, while u_{ck_e} and u_{vk_h} are the same
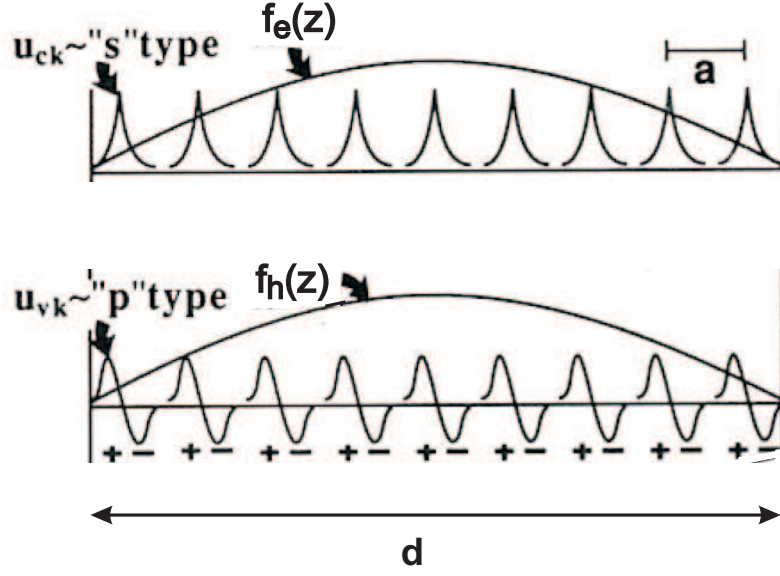
Figure 3.1: Bloch and envelope functions of electrons and holes in a QW

from cell to cell, we can rewrite the integral $\int_V$ as a summation over all cells of the integrations in each unit cell Ω_i:

$$M \approx \delta_{\sigma,j_e-j_h} \sum_{\boldsymbol{R_i}} \int_{\Omega_i} d\boldsymbol{r'} \left[\chi^*_{ck_e}(\boldsymbol{r'}+\boldsymbol{R_i}) u^*_{ck_e}(\boldsymbol{r'}+\boldsymbol{R_i}) e\boldsymbol{r}\cdot\boldsymbol{E}\; u_{vk_h}(\boldsymbol{r'}+\boldsymbol{R_i})\chi_{vk_h}(\boldsymbol{r'}+\boldsymbol{R_i}) \right]$$

$$\simeq \delta_{\sigma,j_e-j_h} \frac{1}{\Omega} \sum_{\boldsymbol{R_i}} \Omega \chi^*_{ck_e}(\boldsymbol{R_i})\chi_{vk_h}(\boldsymbol{R_i})$$

$$\cdot \left[\int_\Omega d\boldsymbol{r'} u^*_{ck_e}(\boldsymbol{r'}) e\boldsymbol{r'} \cdot \boldsymbol{E} u_{ck_h}(\boldsymbol{r'}) + e\boldsymbol{R_i}\cdot\boldsymbol{E} \int_\Omega d\boldsymbol{r'} u^*_{ck_e}(\boldsymbol{r'}) u_{ck_h}(\boldsymbol{r'}) \right].$$

Notice that for the lowest energy interband transition u_{ck_e} has s-wave symmetry while u_{vk_h} has p-wave symmetry (figure 3.1), we obtain:

$$M \simeq \left[\int_V d\boldsymbol{r} \chi^*_{ck_e}(\boldsymbol{r})\chi_{vk_h}(\boldsymbol{r}) \right] \delta_{\sigma,j_e-j_h} \left[\frac{1}{\Omega} \int_\Omega d\boldsymbol{r'}\; u^*_{ck_e}(\boldsymbol{r'})\; u_{ck_h}(\boldsymbol{r'}) e\boldsymbol{r'} \cdot \boldsymbol{e} \right] (\frac{2\pi\omega}{\epsilon\hbar V})^{1/2},$$

$$(3.24)$$

The first term is an overlap integral of the envelope functions of an electron and a hole. Without a confinement potential,

$$\chi_{ck_e}(\boldsymbol{r}) = \exp(i\boldsymbol{k_e} \cdot \boldsymbol{r}) \tag{3.25}$$

$$\chi_{vk_h}(\boldsymbol{r}) = \exp(i\boldsymbol{k_h} \cdot \boldsymbol{r}) \tag{3.26}$$

Then the overlap integral reduces to $\delta(\boldsymbol{k_e} - \boldsymbol{k_h})$. This is the *momentum conservation* condition, since the photon's momentum is negligible compared to excitons.

The second term in equation (3.24) stems from *angular momentum conservation*, it means that for heavy holes, only the pair $j_{hh} = 3/2, j_e = 1/2$ and $j_{hh} = -3/2, j_e = -1/2$ are optical active. The third term is the projection of exciton dipole moment on the light polarization

When an electron and a hole are bound by the Coulomb interaction to form an exciton, the exciton's envelop function consists of a plane wave for the center of mass motion with momentum K, and the bound relative motion. Hence the momentum conservation condition becomes $\boldsymbol{K} = 0$, and the overlap integral is enhanced by $\sqrt{V/a_B^3}$. Unlike an un-correlated electron and hole which move independently throughout the volume V, the electron and hole in an exciton move together with an average relative separation a_B, increasing the probability of an optical transition. This effect is often called the mesoscopic enhancement.

Due to the conservation of angular momentum discussed above, only heavy hole excitons with $j = \pm 1$ can interact with photons which are circularly polarized, hence they are called the bright excitons. Heavy hole excitons with $j = \pm 2$ are called dark excitons for which light emission and absorption are forbidden.

Oscillator Strength of Excitons

A convenient material parameter that characterizes the exciton-photon coupling is the exciton oscillator strength f defined analogous to the atomic oscillator strength

as:

$$f = \frac{2m^*\omega}{\hbar}|\langle u_v|\boldsymbol{r}\cdot\boldsymbol{e}|u_c\rangle|^2\frac{V}{\pi a_B^3} \tag{3.27}$$

The optical transition matrix element M can be expressed in terms of f as:

$$M = \sqrt{\frac{\pi e^2 f}{\epsilon m^* V}}\Gamma \tag{3.28}$$

Γ are the first three terms in equation (3.24) which depends on the selection rules and geometric properties of the semiconductor.

3.3 Quantum-Well Exciton

3.3.1 Quantum Confinement

With the advance of epitaxial growth techniques of molecular beam epitaxy (MBE) and metal organic vapor phase epitaxy, semiconductor materials can be fabricated to atomic monolayer precision, giving birth to novel quantum structures, such as two-dimensional (2D) quantum wells (QWs), 1D quantum wires, and 0D quantum dots. A QW is a thin layer of narrow bandgap semiconductor sandwiched between two barrier layers of wider bandgaps materials (figure 3.2). The quantum well thickness is comparable to the exciton Bohr radius, hence the motion of the electrons and holes are confined perpendicular to the QW plane (which is also the growth direction, and is defined as the z-direction in this thesis), and their energy levels are quantized. Their energy-momentum dispersion have a set of bands (figure 3.3). The energy density of states (DOS) change accordingly from $\propto E^{1/2}$ in 3D to step functions in 2D, as shown in figure 3.4.

The quantum confinement also modifies the valence band structure significantly, as illustrated in figure 3.5(a). Take GaAs for example, the hole has a p-like wavefunction with orbital angular momentum $L = \pm 1$ and spin $S = \pm\frac{1}{2}$. In bulk, holes form two degenerate light hole bands and two degenerate heavy hole bands, and they
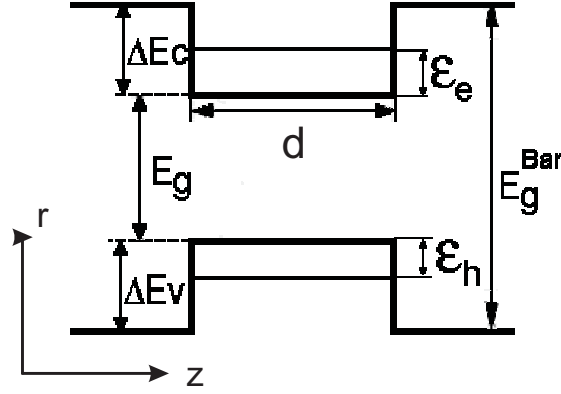
Figure 3.2: Quantum Well
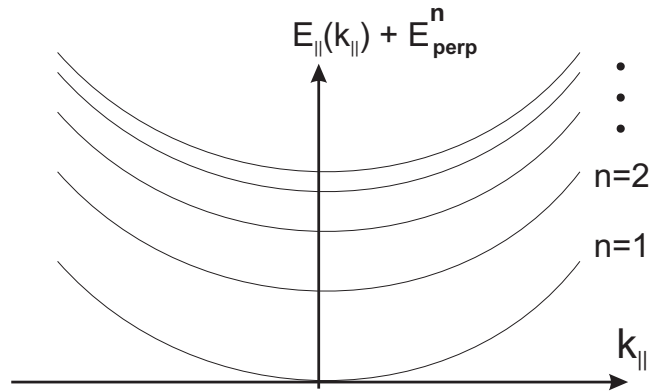
Figure 3.3: Discrete energy bands in a QW

are four-fold degeneracy at $k = 0$. Light holes have a a total angular momentum $J = \pm 1/2$ and a lighter mass of $m_{lh}^{3D} = m_e/(\gamma_1 + 2\gamma_2)$, while the heavy holes have $J = \pm 3/2$ and a heavier mass of $m_{hh}^{3D} = m_e/(\gamma_1 - 2\gamma_2)$ (γ_1 and γ_2 are the Luttinger parameters (51)). In a QW where the translational symmetry is broken in the growth direction, the degeneracy between light and heavy holes at $k = 0$ is lifted, the heavy-hole bands become closer to the conduction band with a lighter in-plane mass of $m_{hh\parallel} = m_e/(\gamma_1 - \gamma_2)$ near $k = 0$ (figure 3.5(b)).

In our experiments, the QW confinement is strong enough so that intra-band mixing is negligible. We only consider the lowest electron band and the heavy hole band, which from the lowest exciton band. The center of mass motion of these excitons are described by 2D plane-wave wavefunctions.
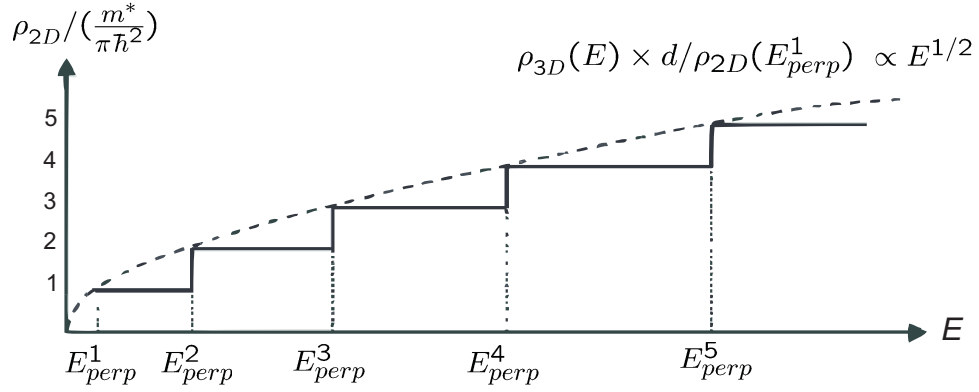
Figure 3.4: Energy density of states in 3D and 2D.

3.3.2 Quantum Well Exciton Binding Energy

In the limit of an exact 2D gas, the Bohr radius of an exciton becomes half of the corresponding 3D value given by equation (3.19), and the binding energy is increased by a factor of four compared to the 3D value in equation (3.18). More accurate values of a_B^{2D} and E_B^{2D} can be obtained by taking into account the finite QW thickness (52; 2; 53). Normally, we are interested in strongly confined excitons, and are only interested in excitons with relatively small momenta. Hence we make the following approximations:

1. The electron and hole are confined in the z-direction by square well potential V_e and V_h, respectively.

2. Conduction and valence bands are treated as parabolic.

3. There is no mixing with higher valence bands.

4. There is no mixing among electron or hole sub-bands.

Then we decompose the wavefunction of exciton's internal motion as:

$$\phi(\boldsymbol{r}_e, \boldsymbol{r}_h) = f_e(z_e)f_h(z_h)g(r, Z), \quad Z = |z_e - z_h|. \tag{3.29}$$

Here $f_e(z_e)$, $f_h(z_h)$ and $g(r, Z)$ are respectively the electron's transverse wavefunction, hole's transverse wavefunction, and the pair's in-plane wavefunction. They satisfy the
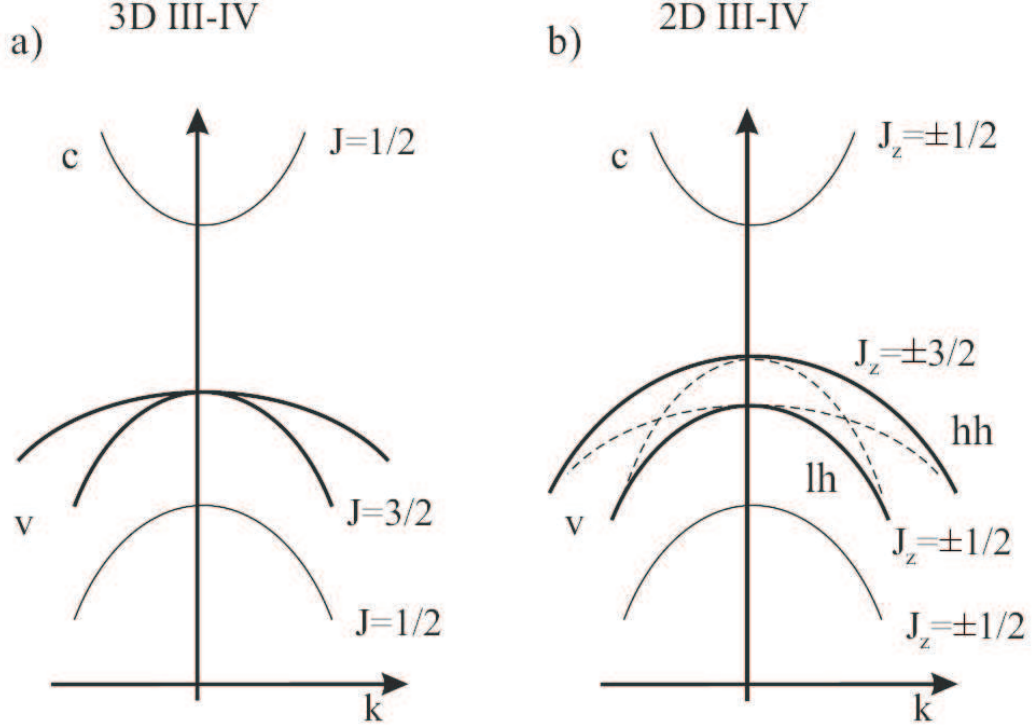
Figure 3.5: Band structures for III-V semiconductors in (a) bulk and (b) QW.

following equations of motion:

$$\left[-\frac{\hbar^2}{2} \frac{d}{dz_e} \left(\frac{1}{m_{e\perp}} \frac{d}{dz_e} \right) + V_e(z_e) \right] f_e(z_e) = \varepsilon_e f_e(z_e), \tag{3.30}$$

$$\left[-\frac{\hbar^2}{2} \frac{d}{dz_h} \left(\frac{1}{m_{h\perp}} \frac{d}{dz_h} \right) + V_h(z_h) \right] f_h(z_h) = \varepsilon_h f_h(z_h), \tag{3.31}$$

$$\left[-\frac{\hbar^2}{2u_\parallel} \frac{1}{r} \frac{d}{dr} \left(r \frac{d}{dr} \right) - \frac{e^2}{\epsilon_0 (r^2 + Z^2)^{1/2}} \right] g(r, Z) = \varepsilon_r(Z) g(r, Z), \tag{3.32}$$

and the binding energy of the exciton is approximately

$$E_B^{2D} = \int dz_e dz_h |f_e(z_e)|^2 |f_h(z_h)|^2 \varepsilon_r(z_e - z_h). \tag{3.33}$$

Here $\varepsilon_r(z_e - z_h)$ is the binding energy of a 2D exciton with the electron and hole confined at $z = z_e$ and $z = z_h$ respectively. E_B^{2D} is an average of $\varepsilon_r(z_e - z_h)$ over the (z_e, z_h) configuration space weighted by the probability of electron at z_e and a hole at z_h.
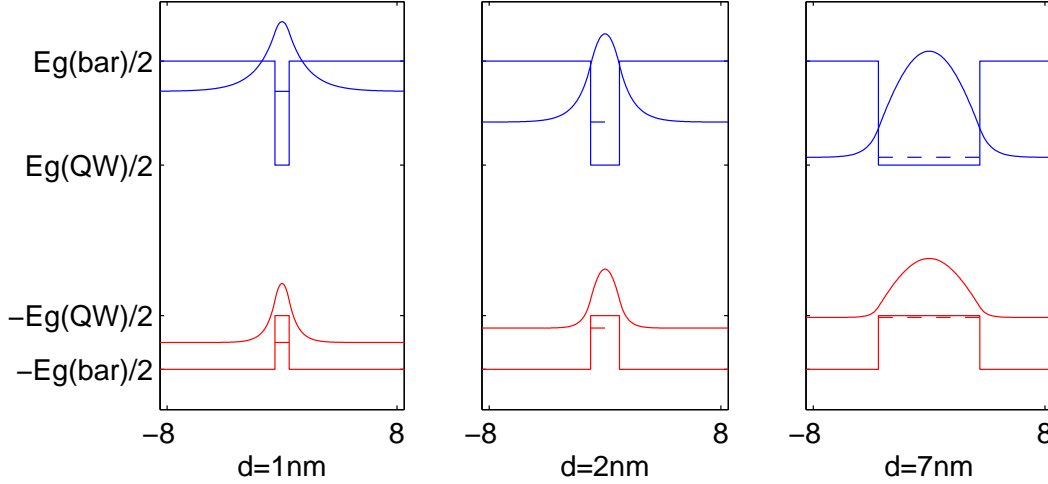
Figure 3.6: $f_e(z)$ and $f_h(z)$ for GaAs/AlAs QWs.

Solutions of f_e in (3.30) and f_h in (3.31) can be found in standard quantum mechanics textbooks. Figure 3.6 gives a few examples for GaAs QW in and AlAs barrier layers. It shows that with decreasing QW thickness d, the electron and hole at first become more and more tightly confined by the QW. When d is too thin, however, the wavefunction starts to spread outside of the QW, and electrons are delocalized much more than the holes. A plane-wave solution is recovered in both limits of $d \to 0$ and $d \to \infty$.

$g(r, Z)$ can be solved via variational methods. Following Leavitt and Little (reference (52)), a reasonably good and easy to calculate ansatz is:

$$g(r, Z) = 4g_0 \exp\left\{\eta \frac{\sqrt{r^2 + Z^2} - Z}{a_B^{3D}}\right\}, \tag{3.34}$$

where η is the variational parameter, g_0 is a normalization factor, and a_B^{3D} is the Bohr radius of $1s$ exciton in bulk. Let $\nu = Z/a_B^{2D}$, from (3.34) and (3.32) we have:

$$\langle \varepsilon(\nu, \eta) \rangle = E_B^{3D} \left[-\eta^2 + \frac{4\eta + 4\eta^4 \nu^2 E_1 2\eta\nu \exp(2\eta\nu)}{1 + 2\eta\nu}\right]. \tag{3.35}$$

$E_1(x) = \int_x^\infty (e^{-t}/t)dt$ is the exponential integral, E_B^{3D} is the binding energy of $1s$ exciton in bulk. η takes the value that minimizes ($\langle \varepsilon(\nu, \eta) \rangle$) for given ν. Then the QW
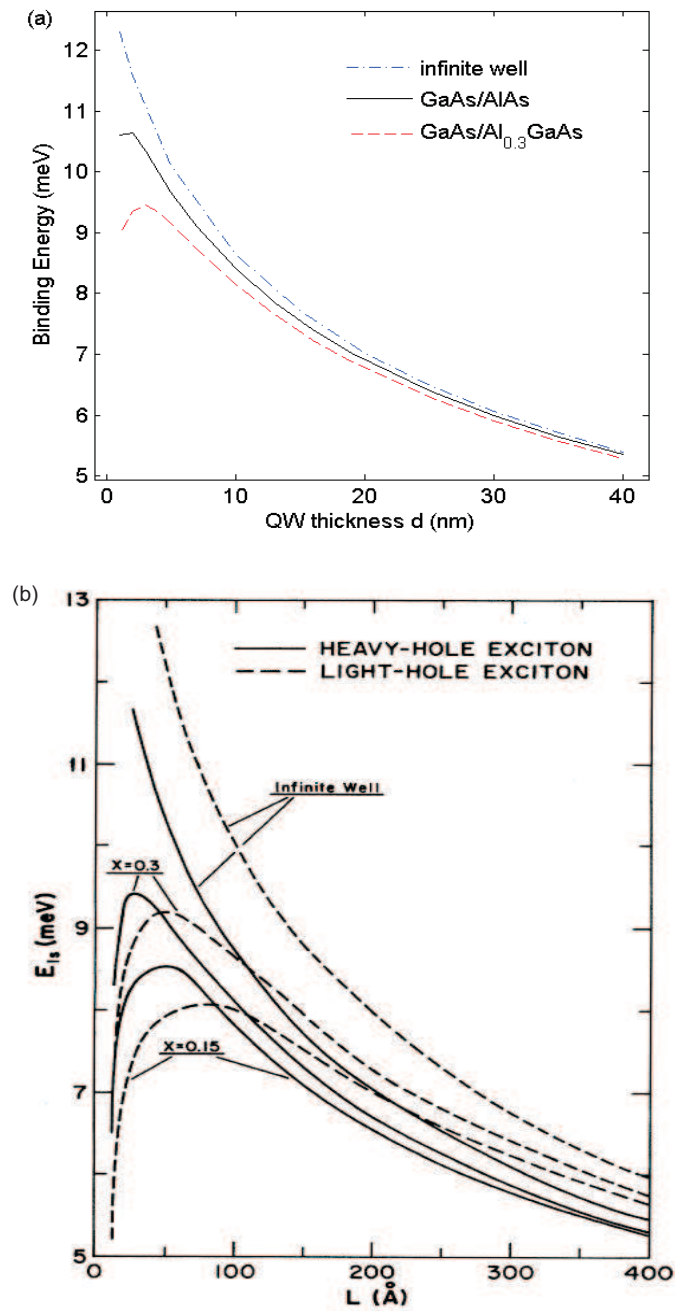
Figure 3.7: Binding energy of $1s$ exciton in GaAs/Al$_x$GaAs QWs (a) Calculated using equation (3.35) and (3.33). (b) From Greene et al. (reference (2)).

exciton binding energy can be calculated using (3.33). Figure 3.7(a) shows the result for GaAs QW with AlAs and Al$_{0.3}$GaAs, AlAs, and infinite potential barrier layers. Figure 3.7(b) shows the results calculated by Greene et al. (2). When d decreases, E_B^{2D} first increases from the bulk limit to an optimal QW thickness $d_{opt} \sim 3$ nm, corresponding to the decrease of Bohr radius a_B with tighter confinement. When d is too thin, as shown in figure 3.6, overlap between f_e and f_h decreases while the average $|z_e - z_h|$ increases, hence E_B^{2D} decreases.

3.3.3   Optical Transition of QW Excitons

A most important effect of quantum confinement is manifested in the optical transitions of excitons in a QW compared to in bulk.

Firstly, the requirement of the momentum conservation condition in the optical transition matrix element (equation (3.24)) is different. Due to QW confinement, the z-direction and in-plane motion of the electron and hole are decoupled, the envelope wavefunction of the electron and hole become,

$$\chi_{ck_e}(\boldsymbol{r}) = f_e(z) \exp(i\boldsymbol{k}_{e\parallel} \cdot \boldsymbol{r}_\parallel) \tag{3.36}$$

$$\chi_{vk_h}(\boldsymbol{r}) = f_h(z) \exp(i\boldsymbol{k}_{h\parallel} \cdot \boldsymbol{r}_\parallel) \tag{3.37}$$

And the first term in equation (3.24) becomes:

$$\int_V d\boldsymbol{r}\,\chi_{ck_e}^*(\boldsymbol{r})\chi_{vk_h}(\boldsymbol{r}) = \int_z dz\,f_e^*(z)f_h(z) \int_S d\boldsymbol{r}_\parallel \exp[i(\boldsymbol{k}_{h\parallel} - \boldsymbol{k}_{e\parallel}) \cdot \boldsymbol{r}_\parallel]. \tag{3.38}$$

The first integral on the righthand side dictates that an optical transition only takes place between electron and hole z-subbands with the same parity, such as the two lowest energy bands (figure 3.6). The second integral requires momentum conservation in the QW plane. Thus excitons in a QW couple to light with the same in-plane wavenumber $k_\parallel$ and arbitrary transverse wavenumber $k_\perp$. QWs are much more optically accessible than bulk materials.

Secondly, heavy holes in a QW only have inplane orbital angular momenta, hence

conservation of the angular momentum means that heavy hole excitons always couple to TE modes. Light hole excitons have one third of probability coupling to TE modes and two thirds of probability to TM modes. The possible transitions which satisfy the angular momentum conservation are summarized in figure 3.8
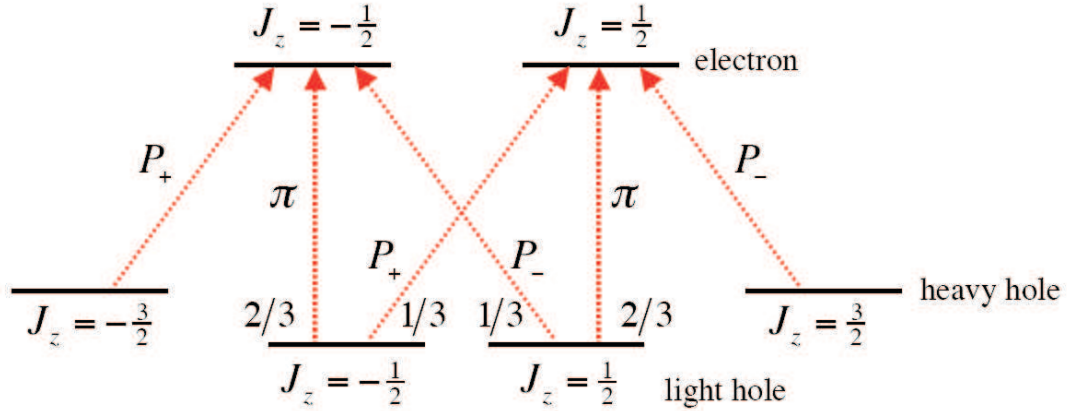
Figure 3.8: Optical transitions between electrons and holes that conserve total angular momentum.

Finally, the exciton Bohr radius is reduced in 2D compared to 3D, leading to an enhancement of the oscillator strength by $(a_B^{3D}/a_B^{2D})^3$.

This enhancement is often offset by a reduction in the overlap between the light field and the exciton, because the longitudinal coherence length of a TE-mode photon field is usually much longer than the QW thickness. To achieve stronger exciton-photon coupling, it is necessary to also confine the photon field in the z-direction by introducing a microcavity.

3.4   Semiconductor Microcavity

Figure 3.9 shows a typical structure of a semiconductor microcavity consisting of a $\lambda_c/2$ cavity layer sandwiched between two distributed Bragg reflectors (DBRs). A DBR is made of layers of alternating high and low refraction indices, each layer with an optical thickness of $\lambda/4$. Light reflected from each interface destructively interfere, creating a stop-band for transmission. Hence the DBR acts as a high-reflectance mirror (Figure 3.10 (a)) when the wavelength of the incident light is within the
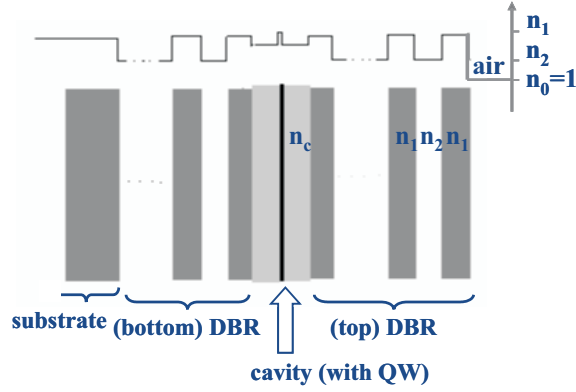
Figure 3.9: Sketch of a semiconductor $\lambda/2$ microcavity.

stopband. The left-side DBR (or, bottom DBR) in figure 3.9 consists of $2N$ layers with alternating refraction indices of n_1 and n_2, the first layer with refraction index n_1 is next to a cavity layer with refraction index n_c, while the last layer with refraction index n_2 is next to the substrate with reflection n_t. For incident light from the cavity side, the maximum reflectivity is at the center of the stopband (54) :

$$R_{max}^{2N} = \left(\frac{1 - \frac{n_c}{n_t}\left(\frac{n_2}{n_1}\right)^{2N}}{1 + \frac{n_c}{n_t}\left(\frac{n_2}{n_1}\right)^{2N}} \right)^2 . \tag{3.39}$$

If the DBR has $N+1$ layers with refraction index n_1 and N layers with n_2, such as the right-side DBR (or, top DBR) in figure 3.9, then:

$$R_{max}^{2N+1} = \left(\frac{1 - \frac{n_c}{n_1}\frac{n_t}{n_1}\left(\frac{n_2}{n_1}\right)^{2N}}{1 + \frac{n_c}{n_1}\frac{n_t}{n_1}\left(\frac{n_2}{n_1}\right)^{2N}} \right)^2 . \tag{3.40}$$

R_{max} always increases with N and increases with the refraction index contrast of the pair. If $n_c < n_1$ or n_2 and $n_t > n_1$ or n_2, as is often the case for a bottom DBR, the maximum reflection is achieved with a DBR of $2N$ layers and with $n_1 > n_2$. In case of a top DBR, light transmits into air which has $n_t = 1 < n_1$ or n_2, then maximum reflection is obtain with a DBR of $2N + 1$ layers and with $n_1 > n_2$. If $1 - R \ll 1$,

R_{max} is approximated by:

$$R_{max}^{2N} \simeq 1 - \frac{4n_c}{n_t}\left(\frac{n_2}{n_1}\right)^{2N}$$

$$R_{max}^{2N+1} \simeq 1 - \frac{4n_c n_t}{n_1^2}\left(\frac{n_2}{n_1}\right)^{2N}. \tag{3.41}$$

Shown in figure 3.10(b) is the change of R_{max}^{2N+1} with N for two different values of n_1/n_2.
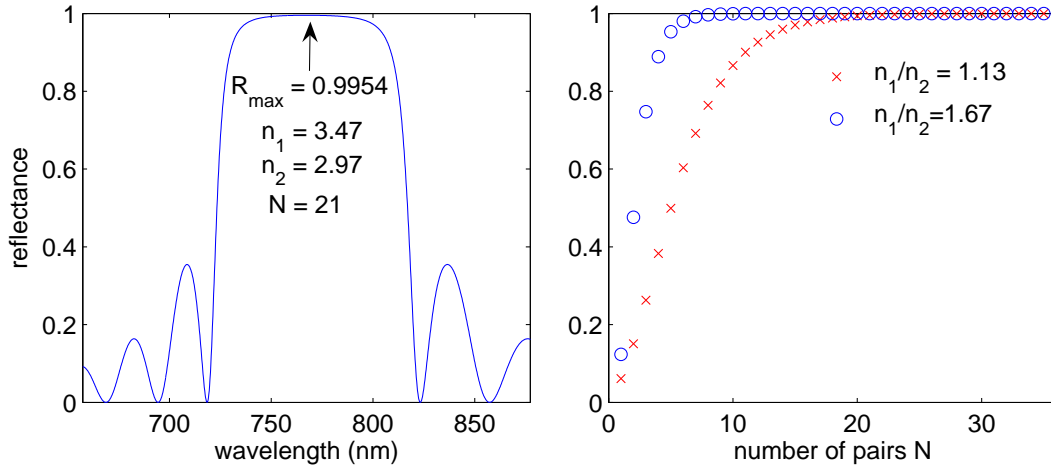
Figure 3.10: (a) Reflection spectra of a typical DBR. (b) R_{max}^{2N} vs. N. Crosses are for a $Al_{0.2}GaAs/AlAs$ DBR with $n_1 = 3.43, n_2 = 2.97$, $n_c = 2.97$ and $n_t = 3.6$, at the stopband center wavelength $\lambda = 767.3$ nm. Circles are for a YF_3/ZnS DBR with $n_1 = 2.43$, $n_2 = 1.50$, $n_c = 2.74$ and $n_t = 3.6$, at $\lambda = 500$ nm. The inset is $1 - R$ vs. N.

When two such high-reflectance DBRs are attached to a layer with an optical thickness integer times of $\lambda_c/2$ ($\lambda_c \approx \lambda$), a cavity resonance is formed at λ_c, leading to a sharp increase of the transmission T at λ_c:

$$T = \frac{(1 - R_1)(1 - R_2)}{[1 - \sqrt{R_1 R_2}]^2 + 4\sqrt{R_1 R_2}\sin^2(\phi/2)}. \tag{3.42}$$

where ϕ is the cavity round-trip phase shift of a photon at λ_c. If $R_1 \approx R_2 = R$, $\left(\frac{1-R}{2}\right)^2 \leq T \leq 1$ depending on ϕ. One characteristic parameter of the cavity quality

is the cavity quality factor Q defined as:

$$Q \doteq \frac{\lambda_c}{\Delta\lambda_c} \simeq \frac{\pi(R_1 R_2)^{1/4}}{1 - (R_1 R_2)^{1/2}}, \tag{3.43}$$

where $\Delta\lambda_c$ is the width of the resonance. An ideal cavity has $Q = \infty$. If the cavity length is $\lambda/2$, Q is the average number of round trips a photon travels inside the cavity before it escapes. Figure 3.11(a) give an example of the reflection spectrum of a cavity with $Q \simeq 4000$. Figure 3.11(b) shows the field intensity distribution $|E(z)|^2$ of a resonant TE-mode. The field is concentrated around the center of the cavity, its intensity is amplified ~ 20 times compared to the free space value. Yet unlike in a metallic cavity, the field penetration depth into the DBRs is much larger. So effective cavity length is extended in a semiconductor microcavity as:

$$L_{eff} = L_c + L_{DBR}$$
$$L_{DBR} \approx \frac{\lambda_c}{2n_c} \frac{n_1 n_2}{|n_1 - n_2|}. \tag{3.44}$$

The planar DBR-cavity confines the photon field in the z-direction but not in plane, incident light from a slant angle θ relative to the z-axis has a resonance at $\lambda_c/\cos\theta$. As a result, the cavity has an energy dispersion vs. the inplane wavenumber $k_{\parallel}$:

$$E_{cav} = \frac{\hbar c}{n_c} \sqrt{k_{\perp}^2 + k_{\parallel}^2}, \tag{3.45}$$

where $k_{\perp} = n_c \frac{2\pi}{\lambda_c}$. And there is a one-to-one correspondence between the incidence angle θ and each resonance mode with inplane wavenumber $k_{\parallel}$:

$$k_{\parallel} = n_c \frac{2\pi}{\lambda_c} \tan[\sin^{-1}(\frac{\sin\theta}{n_c})] \tag{3.46}$$
$$\overset{k_{\parallel} \ll k_{\perp}}{\approx} \frac{2\pi}{\lambda_c}\theta$$
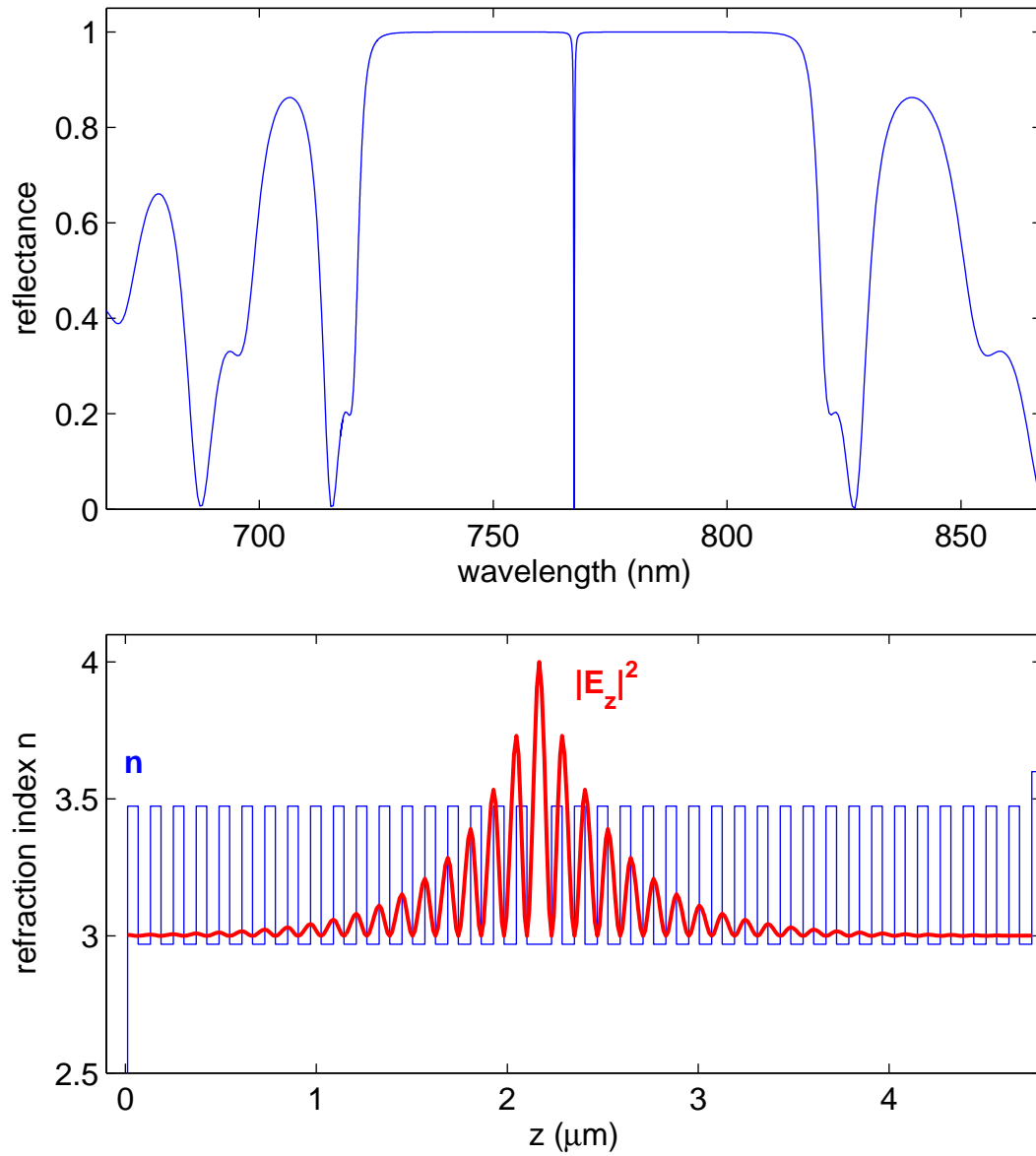
Figure 3.11: (a) Reflectance of an empty $\lambda/2$ microcavity. (b) The cavity structure and field intensity distribution $|E_z|^2$ of the resonant TE mode.
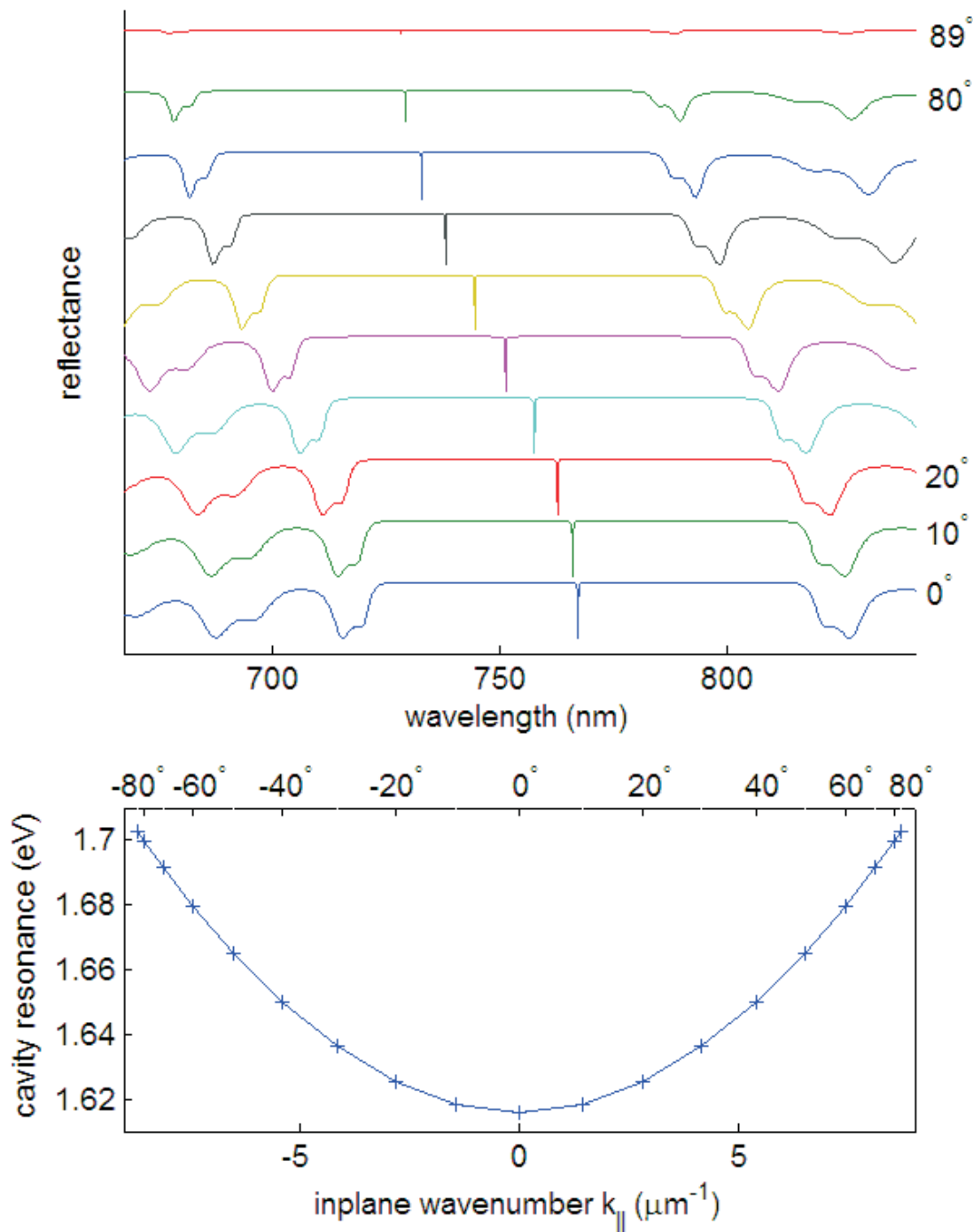
Figure 3.12: (a) Incidence angle θ dependence of the cavity reflectance. (b) Cavity dispersion E_{cav} vs. $k_\parallel$ or θ

In the region $k_\parallel \ll k_\perp$, we have:

$$E_{cav} \approx \frac{\hbar c}{n_c k_\perp}(1 + \frac{k_\parallel^2}{2k_\perp^2})$$

$$= E_{cav}(k_\parallel = 0) + \frac{\hbar^2 k_\parallel^2}{2(2\pi\hbar/\lambda_c c)}$$

$$= E_{cav0} + \frac{\hbar^2 k_\parallel^2}{2m_{cav}}. \tag{3.47}$$

Thus the cavity photon acquires an effective mass of

$$m_{cav} = \frac{2\pi\hbar}{\lambda_c c} \tag{3.48}$$

Figure 3.12 gives a numerical example of the angle-tuning, or energy and inplane wavenumber dispersion of the cavity resonance.

3.5   Qunatum-Well Microcavity Polariton

When the GaAs QWs are placed at the antinodes of a semiconductor microcavity, the $J = 1$ heavy hole exciton doublet strongly interacts with the confined optical field of the cavity. If the rate of energy exchange between the cavity field and the excitons becomes much faster than the decay and decoherence rates of both the cavity photons and the excitons, an excitation in the system is stored in the combined system of photon and exciton. Thus the elementary excitations of the system are no longer exciton *or* photon, but a new type of quasi-particles called the polaritons.

Using the rotating wave approximation, the linear Hamiltonian of the system is written in the second quantization form as:

$$\hat{H}_{pol} = \hat{H}_{cav} + \hat{H}_{exc} + \hat{H}_I$$

$$= \sum E_{cav}(k_\parallel, k_c)\hat{a}_{\boldsymbol{k}_\parallel}^\dagger \hat{a}_{\boldsymbol{k}_\parallel} + \sum E_{exc}(k_\parallel)\hat{e}_{\boldsymbol{k}_\parallel}^\dagger \hat{e}_{\boldsymbol{k}y} + \sum \hbar\Omega(\hat{a}_{\boldsymbol{k}_\parallel, k_c}^\dagger \hat{e}_{\boldsymbol{k}_\parallel} + \hat{a}_{\boldsymbol{k}_\parallel} \hat{e}_{\boldsymbol{k}_\parallel}^\dagger).$$

$$\tag{3.49}$$

Here $\hat{a}_{\boldsymbol{k}_\parallel}^\dagger$ is the photon creation operator with inplane wavenumber $k_\parallel$ and longitudinal

wavenumber $k_c = \boldsymbol{k} \cdot \hat{\boldsymbol{z}}$ determined by the cavity resonance. $\hat{e}^{\dagger}_{\boldsymbol{k}_{\parallel}}$ is the exciton creation operators with inplane wavenumber $\boldsymbol{k}_{\parallel}$. $\hbar\Omega$ is the exciton-photon dipole interaction given by the exciton optical transition matrix element M (equation (3.28)), and we used the condition that M is non-zero only between modes with the same $\boldsymbol{k}_{\parallel}$. The above Hamiltonian can be diagonalized by the transformation:

$$\hat{p}_{\boldsymbol{k}_{\parallel}} = X_{\boldsymbol{k}_{\parallel}} \hat{e}_{\boldsymbol{k}_{\parallel}} + C_{\boldsymbol{k}_{\parallel}} \hat{a}_{\boldsymbol{k}_{\parallel}} \tag{3.50}$$

$$\hat{q}_{\boldsymbol{k}_{\parallel}} = -C_{\boldsymbol{k}_{\parallel}} \hat{e}_{\boldsymbol{k}_{\parallel}} + X_{\boldsymbol{k}_{\parallel}} \hat{a}_{\boldsymbol{k}_{\parallel}}, \tag{3.51}$$

And $\hat{H}_{pol}$ becomes:

$$\hat{H}_{pol} = \sum E_{LP}(k_{\parallel}) \hat{p}^{\dagger}_{\boldsymbol{k}_{\parallel}} \hat{p}_{\boldsymbol{k}_{\parallel}} + \sum E_{UP}(k_{\parallel}) \hat{q}^{\dagger}_{\boldsymbol{k}_{\parallel}} \hat{q}_{\boldsymbol{k}_{\parallel}}. \tag{3.52}$$

The new operators $(\hat{p}_{\boldsymbol{k}_{\parallel}}, \hat{p}^{\dagger}_{\boldsymbol{k}_{\parallel}})$ and $(\hat{q}_{\boldsymbol{k}_{\parallel}}, \hat{q}^{\dagger}_{\boldsymbol{k}_{\parallel}})$ are the new quasi-particles, or, eigen modes, of the system. They are called the lower (LP) and upper polaritons (UP), corresponding to the lower and upper branches of the eigen energies. A polariton is a linear superposition of an exciton and a photon with the same inplane wavenumber $\boldsymbol{k}_{\parallel}$. Since both excitons and photons are bosons, so are the polaritons. The exciton and photon fractions in each lower polariton (and vice versa for upper polaritons) are given by the amplitude squared of $X_{k_{\parallel}}$ and $C_{k_{\parallel}}$ which are referred to as the Hopfield coefficients (55), they satisfy:

$$|X_{k_{\parallel}}|^2 + |C_{k_{\parallel}}|^2 = 1. \tag{3.53}$$

Let $\Delta E(k_{\parallel}) = E_{exc}(k_{\parallel}) - E_{cav}(k_{\parallel}, k_c)$, $X_{k_{\parallel}}$ and $C_{k_{\parallel}}$ are given by:

$$|X_{k_{\parallel}}|^2 = \frac{1}{2}\left(1 + \frac{\Delta E(k_{\parallel})}{\sqrt{\Delta E(k_{\parallel})^2 + 4\hbar^2\Omega^2}}\right),$$

$$|C_{k_{\parallel}}|^2 = \frac{1}{2}\left(1 - \frac{\Delta E(k_{\parallel})}{\sqrt{\Delta E(k_{\parallel})^2 + 4\hbar^2\Omega^2}}\right), \tag{3.54}$$

At $\Delta E = 0$, $|X|^2 = |C|^2 = \frac{1}{2}$, LP and UP are exactly half photon half exciton.
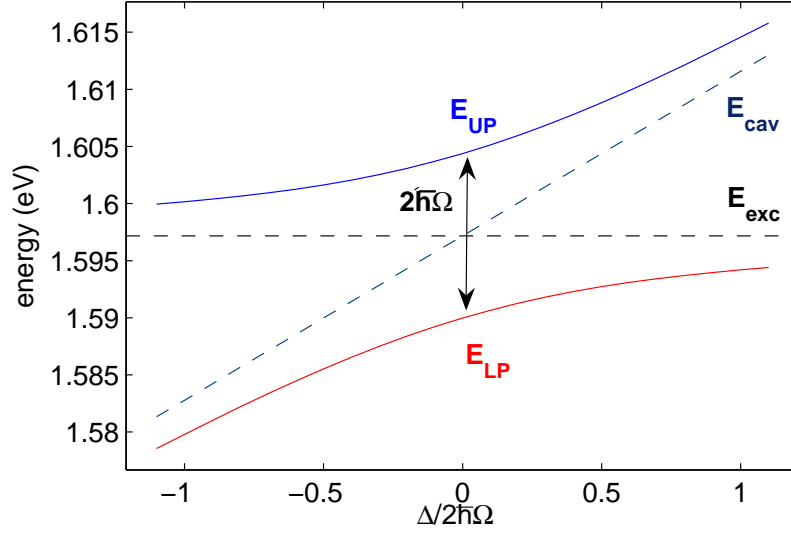
Figure 3.13: Anti-crossing of LP and UP energy levels when tuning the cavity energy across the exciton energy by transfer matrix calculation.

The energies of the polaritons, which are the eigen energies of the Hamiltonian (3.52), are deduced from the diagonalization procedure as:

$$E_{LP,UP}(k_{\parallel}) = \frac{1}{2}\left[E_{exc} + E_{cav} \pm \sqrt{4\hbar^2\Omega^2 + (E_{exc} - E_{cav})^2}\right], \qquad (3.55)$$

When the un-coupled exciton and photon are at resonance, $E_{exc} = E_{cav}$, lower and upper polariton energies have the minimum separation $E_{UP} - E_{LP} = 2\hbar\Omega$, which is often called the 'Rabi splitting' in analogy to the atomic cavity Rabi splitting. Due to the coupling between the exciton and photon modes, the new polariton energies anti-cross when the cavity energy is tuned across the exciton energy. This is one of the signatures of 'strong coupling' (figure 3.13). When $|E_{cav} - E_{exc}| \gg \hbar\Omega$, the polariton energies reduce to the same as photon and exciton energies due to the very large detuning between the two modes, and polariton is no longer a useful concept. So the detuning is assumed to be comparable to or less than the coupling strength in our discussions unless specified.

We use Δ as the exciton and photon energy detuning at $k_\parallel = 0$:

$$\Delta \doteq E_{cav}(k_\parallel = 0) - E_{exc}(k_\parallel = 0),, \tag{3.56}$$

and define

$$k_{\parallel c} \doteq \sqrt{n_c k_c \frac{2\Omega}{c}}, \tag{3.57}$$

for which $E_{cav}(k_{\parallel c}) - E_{cav}(0) \sim \hbar\Omega$. Given Δ, equation (3.55) gives the polariton energy-momentum dispersions. At $k_\parallel \ll k_{c\parallel}$, the dispersions are approximately parabolic:

$$E_{LP,\ UP}(k_\parallel) \simeq E_{LP,\ UP}(0) + \frac{\hbar^2 k_\parallel^2}{2m_{LP,\ UP}}. \tag{3.58}$$

The polariton effective mass is the weighted harmonic mean of the mass of its exciton and photon components:

$$\frac{1}{m_{LP}} = \frac{|X|^2}{m_{exc}} + \frac{|C|^2}{m_{cav}}, \tag{3.59}$$

$$\frac{1}{m_{UP}} = \frac{|C|^2}{m_{exc}} + \frac{|X|^2}{m_{cav}},, \tag{3.60}$$

where X and C are the exciton and photon fractions given by (3.54). m_{exc} is effective exciton mass of its center of mass motion, and m_{cav} is the effective cavity photon masses given by (3.48). Since m_{cav} is much smaller than m_{exc},

$$m_{LP}(k_\parallel \sim 0) \simeq m_{cav}/|C|^2 \sim 10^{-4} m_{exc},$$
$$m_{UP}(k_\parallel \sim 0) \simeq m_{cav}/|X|^2. \tag{3.61}$$

The very small effective mass of LPs at $k_\parallel \sim 0$ determines the very high critical temperature of phase transitions for the system. At large $k_\parallel \gg k_{c\parallel}$, $E_{cav}(k_\parallel) - E_{exc}(k_\parallel) \gg \hbar\Omega$, dispersions of the LP and UP converge to the exciton and photon dispersions respectively, and LP has an effective mass $m_{LP}(k_\parallel \gg k_{c\parallel}) \sim m_{exc}$. Hence

the LP's effective mass changes by four order of magnitude from $k_\parallel \sim 0$ to large $k_\parallel$. This peculiar shape has important implications in the energy relaxation dynamics of polaritons, as will be discussed in chapter 5 and 6. A few examples of the polariton dispersion with different Δ are given if figure 3.14.

When taking into account the finite lifetime of the cavity photon and QW exciton, the eigen-energy equation (3.55) is modified as:

$$E_{LP,UP}(k_\parallel) = \frac{1}{2} \left[E_{exc} + E_{cav} + i(\gamma_{cav} + \gamma_{exc}) \right.$$
$$\left. \pm \sqrt{4\hbar^2\Omega^2 + [E_{exc} - E_{cav} + i(\gamma_{cav} - \gamma_{exc})]^2} \, \right]. \qquad (3.62)$$

Here γ_{cav} is the out-coupling rate of a cavity photon due to imperfect mirrors, and γ_{exc} is the non-radiative decay rate of an exciton. Thus the coupling strength must be larger than half of the difference in decay rates to exhibit anti-crossing, i.e., to have polaritons as the new eigen modes. In another word, an excitation must be able to coherently transfer between a photon and an exciton at least once. When $\hbar\Omega \gg (\gamma_{cav} - \gamma_{exc})/2$, we call the system in the *strong coupling* regime. In the opposite limit when excitons and photons instead are the eigen modes, the system is called to be in the *weak coupling* regime, and the radiative decay rate of an exciton is given by the optical transition matrix element. We are mostly interested in microcavities with $\gamma_{exc} \ll \gamma_{cav} \ll \hbar\Omega$, then equation (3.55) gives an accurate approximation of the polariton energies.

As a linear superposition of an exciton and a photon, the lifetime of the polaritons is directly determined by γ_{exc} and γ_{cav} as:

$$\gamma_{LP} = |X|^2\gamma_{exc} + |C|^2\gamma_{cav}, \qquad (3.63)$$

$$\gamma_{UP} = |C|^2\gamma_{exc} + |X|^2\gamma_{cav}. \qquad (3.64)$$

In current semiconductor samples, we have $\gamma_{cav} = 1 \sim 10$ ps and $\gamma_{exc} \sim 1$ ns, hence the polariton lifetime is mainly determined by the cavity photon lifetime: $\gamma_{LP} \simeq |C|^2\gamma_{cav}$. Polariton decays in the form of emitting a photon with the same $k_\parallel$ and total energy
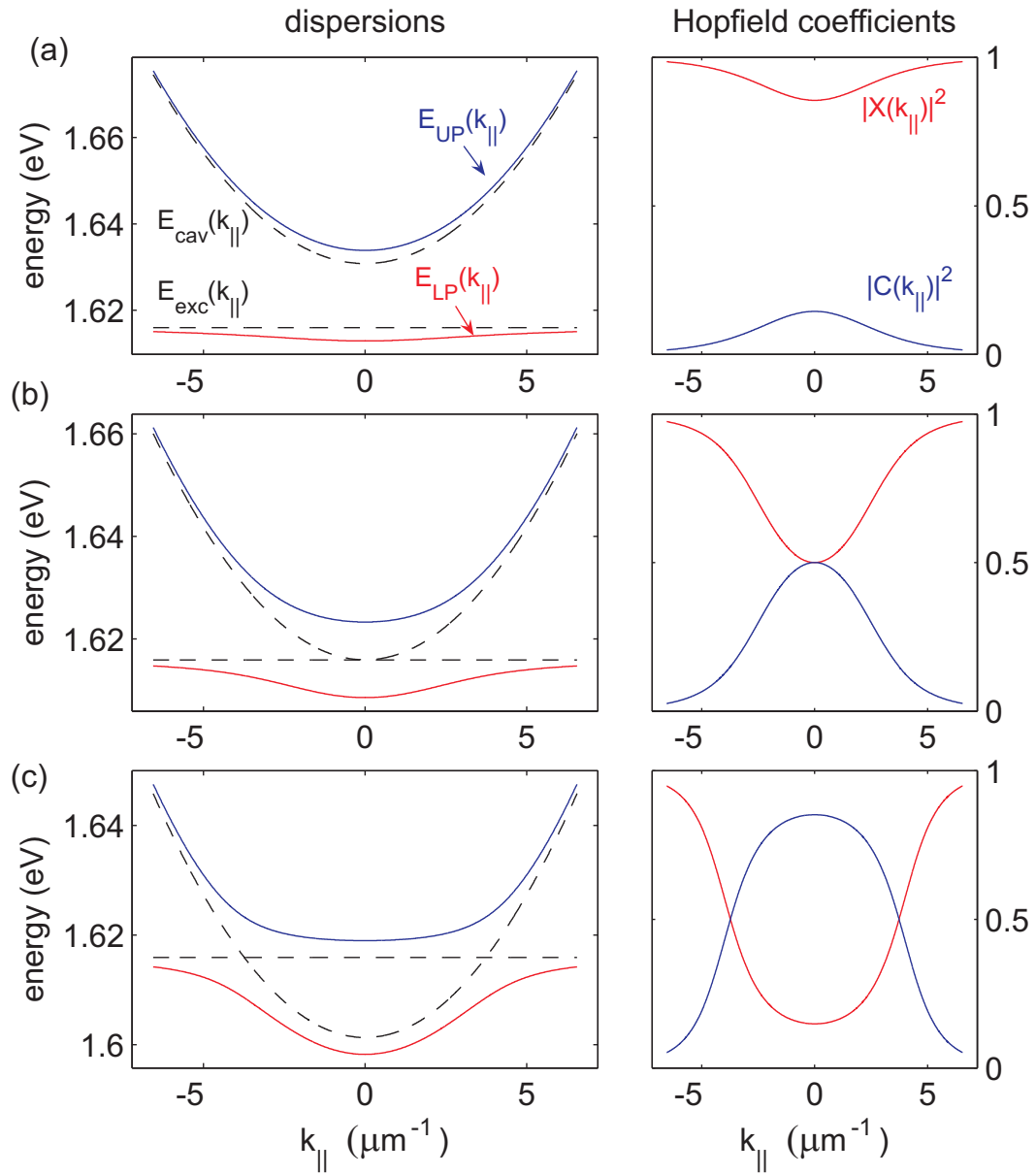
Figure 3.14: Polariton dispersions and corresponding Hopfield coefficients at (a) $\Delta = 2\hbar\Omega$, (b) $\Delta = 0$, and (c) $\Delta = -2\hbar\Omega$.

$\hbar\omega = E_{LP,\ UP}$. The one-to-one correspondence between the internal polariton mode and the external out-coupled photon mode lends great convenience to experimental access to the system. The external emitted photon field carry direct information of the internal polaritons, such as the energy dispersion, population per mode, and statistics of the polaritons. It is mainly through the emitted photons that we study the internal polaritons.

Comparison to Bulk Polaritons

In bulk semiconductors, due to the full overlap of the cavity and exciton envelop wavefunctions (both are plane waves), the coupling strength is relatively large, and polaritons are often eigen modes of the system. For GaAs, we have $2\hbar\Omega \sim 8$ meV. However, in bulk with 3D translation symmetry, a polariton has the same wavenumber as that of its exciton and photon constituents: $k \sim n_{bulk}E_{exc}/\hbar c \sim k_c$, rather than $k_\parallel \sim \sqrt{k^2 - k_c^2} \ll k_c$ in case of a QW polariton. Hence a bulk polariton (in the region $|E_{cav} - E_{exc}|$ comparable to $\hbar\Omega$) always has large phase velocity and kinetic energy. It is vulnerable to various dephasing channels in a solid. And the thermal equilibrium state of the system (if assuming infinite lifetime) consist of mostly $k \sim 0$ photon-like modes, rather than $k_\parallel \sim 0$ LPs in case of a QW-microcavity. Furthermore, a bulk polariton does not couple out of the system till it hits the surface of the crystal. It is subject to scattering by crystal defects and impurities as well as other excitons and polaritons. Hence the 'lifetime' of a polariton or exciton inside the crystal depends on the distribution and density of the polaritons, photoluminescence from the crystal carry only indirect information of the polaritons inside. Moreover, inside the bulk, the LP branch is outside of the optical cone (figure 3.15) and do not directly couple to light. It is in general very difficult to study a bulk system in experiments.

Although the field-exciton overlap in z-direction is small for a QW, the field intensity of the cavity mode can be amplified by the cavity confinement. Moreover, the decreased exciton Bohr radius in 2D leads to a larger mesoscopic enhancement effect of $(a_B^{3D}/a_B^{QW})^{3/2}$. As a typical example, a 20 nm wide GaAs QW in a $\lambda/2$ cavity with $Q \sim 2000$ has a field-exciton overlap of ~ 0.2, and an observed $2\hbar\Omega = 4$ meV. By
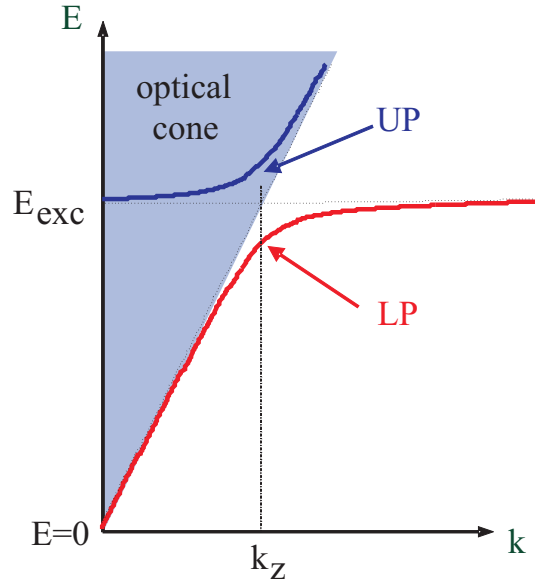
Figure 3.15: Illustration of the dispersions of bulk upper (UP) and lower polaritons (LP), using parameters for GaAs and a coupling strength (hence the UP-LP splitting) 50 times larger than the actual value. With an actual coupling strength, the LP-UP splitting would be barely visible in the current scale.

using thinner QWs to take advantage of a smaller Bohr radius, and using multiple QWs to increase the field overlap, $2\hbar\Omega = 15$ meV was measured in a $\lambda/2$ cavity with twelve 7-nm wide GaAs QWs. The coupling strength is even larger than in the bulk case.

Finally, QW-microcavity systems are more flexible than bulk system with a few very useful tuning parameters such as the QW thickness, number and position, and the cavity length.

3.6   Very Strong Coupling Regime

The definition of polariton operators by equations (3.49) to (3.52) follows the procedure that first diagonalizes the electron-hole Hamiltonian by exciton operators, and then diagonalizes the exciton-photon Hamiltonian by polariton operators, treating the excitons as structure-less quasi-particles. When the exciton-photon coupling is so strong as to become comparable to exciton binding energy, the question arises whether or not the above procedure is still valid. More rigorous is to treat the electron, hole

and photon on equal footing (56; 57), and one finds that the LPs then consists of excitons with an even smaller effective Bohr radius and larger binding energy, while the opposite holds for UPs. This named the *very strong coupling* effect. It can also be understood as a consequence of sub-band mixing of excitons (mixing between 1s, 2s, 2p... exciton levels).

Following Khurgin (56), the Hamiltonian of the system is written as:

$$\hat{H} = \hat{H}_k + \hat{H}_{eh} + \hat{H}_{eh-p} + \hat{H}_p. \tag{3.65}$$

It consists of the kinetic energy term of the electron-hole pair $\hat{H}_k$, the Coulomb attraction between the electron and hole $\hat{H}_{eh}$, the coupling between the electron-hole pair and photon $\hat{H}_{eh-p}$ and the photon energy $\hat{H}_p$:

$$\hat{H}_k = \frac{\hbar^2}{2m_r}\nabla_{r_{e-h}} + \frac{\hbar^2}{2M} \tag{3.66}$$

$$\hat{H}_{eh} = -\frac{e^2}{\epsilon r_{e-h}} \tag{3.67}$$

$$\hat{H}_{eh-p} = -\frac{e\hat{p}}{m_0\sqrt{\hbar/2\epsilon\omega V}}(\hat{a}_{\boldsymbol{k}_\parallel} + \hat{a}^\dagger_{\boldsymbol{k}_\parallel}) \tag{3.68}$$

$$\hat{H}_p = \hbar\omega(\boldsymbol{k}_\parallel)\hat{a}^\dagger_{\boldsymbol{k}_\parallel}\hat{a}_{\boldsymbol{k}_\parallel}. \tag{3.69}$$

Here $V = d \cdot S$ is the effective volume of the cavity, $k_\parallel$ is the inplane wavenumber of the photon mode and the center of mass motion of the electron-hole pair, k_z is the resonance wavenumber of the cavity: $k_z \sim 2\pi/L_c$, and the photon energy is $\hbar\omega(\boldsymbol{k}_\parallel) = \hbar c(k_z^2 + k_\parallel^2)^{1/2}$. The polariton wavefunction $|\Psi_{pol}\rangle$ to diagonalize the Hamiltonian is still a linear superposition of an exciton and a photon, yet the exciton wavefunction takes the variational form:

$$\phi_0(r) = \sqrt{\frac{2}{\pi}}\frac{\lambda}{a_B}e^{-\lambda r/a_B} = \frac{1}{S}\sum_{k_r}A_{k_r}e^{ik_r\cdot r}, \tag{3.70}$$

with λ as the variational parameter. The corresponding effective Bohr radius becomes a_B/λ. Here a_B is the 2D exciton Bohr radius $a_B = \hbar^2\epsilon_0/(2e^2 m_r)$ and k_r is the
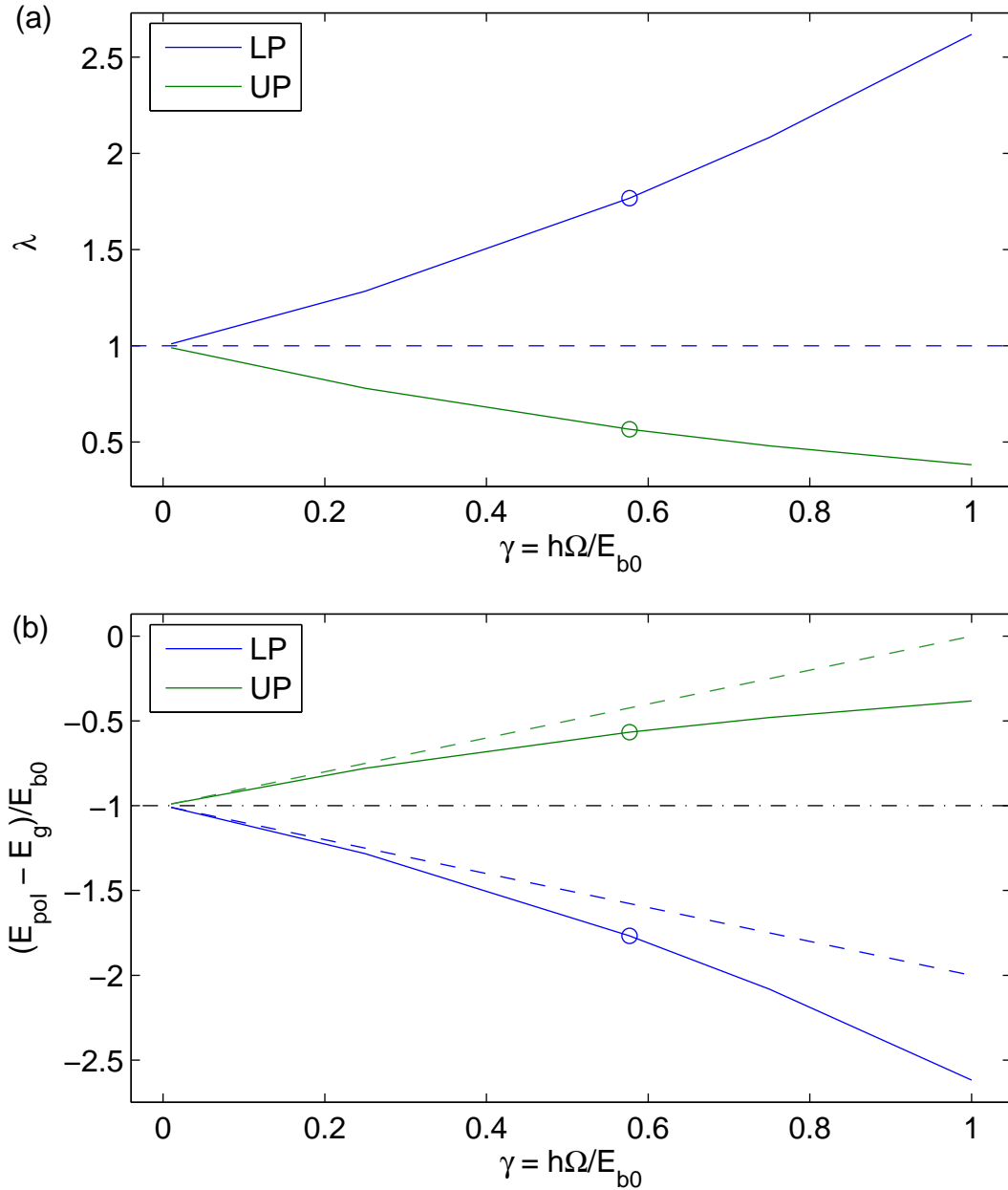
Figure 3.16: Dependence of the effective exciton Bohr radius a_B^* and polariton energies on the exciton-photon coupling strength. Solid lines are calculated using the *very strong coupling* variational method, dashed lines are results assuming an unchanged bare exciton Bohr radius: $a_B^* = a_B$. The circles denote the coupling strength of sample S-GaAs-I. (a) Inverse of the normalized Bohr radius a_B/a_B^*. (b) LP and UP energies normalized by the bare 2D exciton binding energy, relative to the bandgap energy E_g.

wavenumber of the relative motion of the electron and hole. Then we have:

$$|\psi_{pol}\rangle = X \sum_{k_r} \frac{1}{S} A_{k_r} |k_r, k_\parallel\rangle + C|k_\parallel, k_z\rangle, \tag{3.71}$$

$$|X|^2 + |C|^2 = 1.$$

And:

$$E = \langle \psi_{pol}|\hat{H}|\psi_{pol}\rangle$$
$$= E_{b0}[\alpha^2\lambda^2 - 2\alpha^2\lambda - \alpha\beta\gamma\lambda + \beta^2\Delta(0) + \Delta(k_\parallel)]. \tag{3.72}$$

Here $E_{b0} = \hbar^2/(2m_r a_B^2)$ is the binding energy of a 2D exciton, $\gamma \doteq \hbar\Omega/E_{b0}$, and $\Delta(k_\parallel) \doteq \hbar\omega(k_\parallel)/E_{b0}$ is the ratio of the coupling strength to the bare exciton binding energy. The bandgap energy E_g is used as the energy zero reference. Minimizing E with λ, we obtain the effective Bohr radius a_B/λ and the LP or UP energies E depending on $X > 0$ or $X < 0$.

As an example, we use the parameter for S-GaAs-I to calculate λ for various coupling strength, and plot in figure 3.16 the resulting $a_B^* = a_B/\lambda$ and E_{LP} and E_{UP}. The exciton Bohr radius a_B^* shrinks in the LP branch while increases in the UP branch. Both E_{LP} and E_{UP} are lowered compared to the value without taking into account the very strong coupling effect.

3.7   Polaritons for BEC Study

3.7.1   Uniqueness of Polaritons

As composite bosons with not only fermionic but also photonic constituents, polaritons are a unique system for exploring both cavity QED and many particle physics. A variety of quantum phases are predicted for polaritons, including BEC, superfluidity, crossover from BEC to Bardeen-Cooper-Schrieffer states (6; 7; 1; 8; 9). Compared to other BEC systems, such as atomic gases and excitons, polaritons have vastly

different length, energy and time scales. (section 1.2, table 1.1). Beside as an essentially different system of fundamental interest, polaritons also possess many unique advantages for BEC research.

First of all, the critical temperature of polariton condensation ranges from a few kelvin to above room temperature, which is four order of magnitude higher than that of excitons and eight orders of magnitude higher than that of atoms. It originates from the very light effective mass of polaritons due to the mixing with cavity photons ((2.16) and (3.59)).

From the experimental viewpoints, the microcavity polariton is a most accessible system. There exists a one-to-one correspondence between an internal polariton in mode $k_\parallel$ and an external photon with the same energy and inplane-wavenumber, propagating at an angle θ from the growth direction. The polariton is coupled to this photon via its the photonic component with a fixed coupling rate (3.64). Hence information of the internal polaritons can be directly measured from the external photon field by standard quantum optical techniques, including the polaritons' energy-momentum dispersions, populations per mode, distribution functions, and correlation functions. Conversely, polaritons are conveniently excited, resonantly or non-resonantly, by optical pumping. The excitation density spans the whole density range of interest.

A major enemy against quantum phase transitions in solids is the unavoidable compositional and structural disorders. By dressing the excitons with the microcavity vacuum field, extended coherence is maintained in the combined excitation in a microcavity polariton system, and the detrimental effects of disorders are largely suppressed.

Saturation and phase space filling pose another obstacle against BEC of composite boson in solids. In a microcavity system, multiple QWs can be used to distribute the exciton density for a given total polariton density: $n_{exc}^{QW} = n_{LP}/N_{QW}$, where N_{QW} is the number of QWs.

The main challenge for realizing of a thermodynamic phase transition and spontaneous coherence has always been efficient cooling of hot particles. It is particularly so for relatively short lived quasi-particles, excitons and polaritons, in solids. The small

effective mass hence small energy density of states of polaritons comes to rescue here. Due to the small DOS, a quantum degenerate seed of low energy polaritons is relatively easy to achieve. Hence bosonic final state stimulation effect is pronounced, which greatly accelerates energy relaxation of the polaritons.

Finally, the microcavity system of a given composition has two very useful adjustable parameters: the number of QWs N_{QW} and the cavity-exciton detuning Δ. For example, N_{QW} changes the exciton-photon coupling strength $\Omega \propto \sqrt{N_{QW}}$ as well as the polariton-polariton scattering rate $\propto n_{exc}^{QW} N_{QW}$. When Ω is increased to become comparable with the exciton binding energy, the *very strong coupling* effect further reduces exciton Bohr radius in the LP branch and increases the exciton saturation density. Detuning Δ is very conveniently changed due to the taper of the cavity thickness across each wafer. It tunes the exciton and photon fractions in the LPs, hence the dispersions and lifetimes of the LPs. It has important implications in LP equilibration which will be discussed in chapter 6.

3.7.2 Critical Densities of 2D Microcavity Polaritons

Microcavity polariton as a 2D system does not have a BEC transition at finite temperature in the thermodynamic limit. Yet BEC exists if we impose a spatially varying in-plane confinement potential or if the system size is finite (section 2.7). The former will be discussed briefly in chapter 7, while the latter is usually the scenario in this thesis. In figure 3.17, we compare the critical density of KT transition of LPs and quasi-BEC in a finite-size system calculated following Kavokin et al. (58).

3.7.3 BEC-BCS Crossover

An important parameter missing in the table 1.1 is the particle-particle interaction strength, or, the scattering length a. For bosonic atom gases, a is usually much less than the particle spacing, satisfying the diluteness condition. In di-atomic gases where each di-atomic molecule consists of two fermionic atoms, a can be defined for the interaction between two fermi-atoms. a has a hyperbolic dependence on an
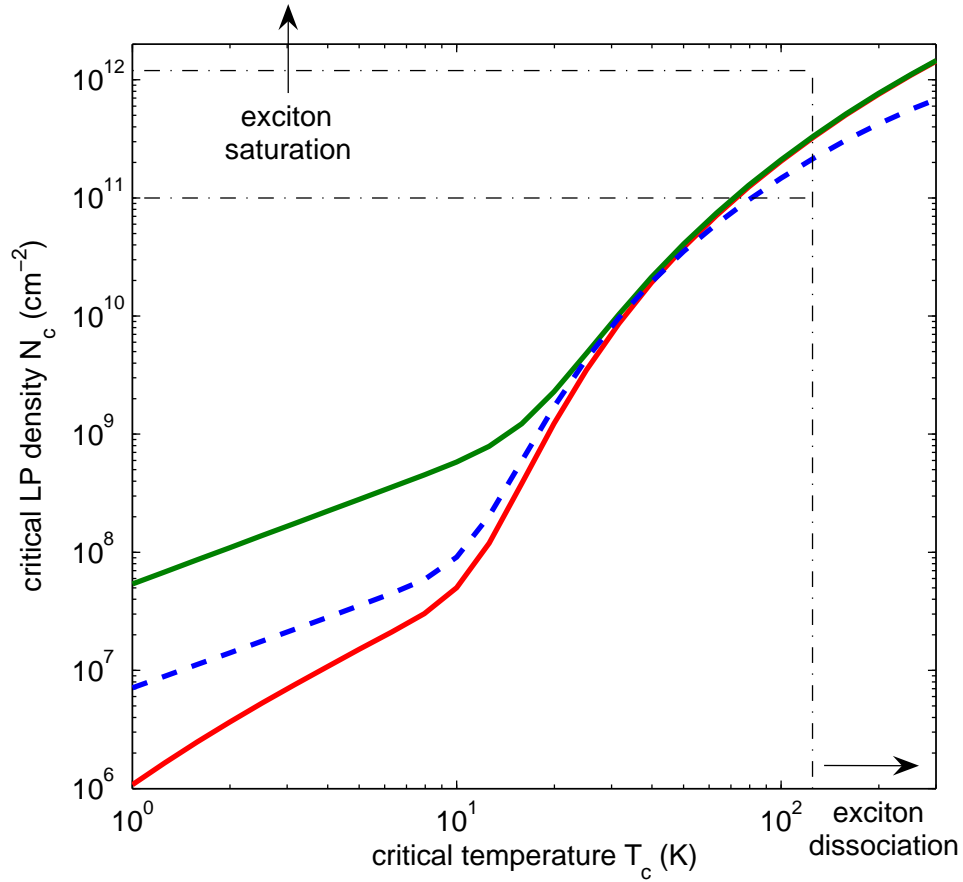
Figure 3.17: Critical density of KT transition (dashed line) and quasi-BEC in a systems of size $S = L^2$: $L = 20$ μm (the lower red solid line) and 1 m (the upper green solid line). The vertical dash-dotted line indicates the upper-bound of exciton-dissociation temperature. The horizontal dash-dotted lines indicate the exciton saturation density for a microcavity with a single QW (the lower one) and with twelve QWs (the upper one). Parameters of S-GaAs-I are used.

external magnetic field which tunes a from a small negative value ($a < 0, k_f|a| \ll$ 1, k_f is the wave-vector at the Fermi surface) to a very large negative or positive value at the unitary condition ($k_f|a| \gg 1$) near the Feshbach resonance and to a small positive value (59). Correspondingly, below a critical temperature, the system exhibits a crossover from a degenerate fermi gas described by standard BCS theory to a degenerate bose gas with a BEC phase.

A similar BEC to BCS crossover also exists in exciton and polariton systems (7; 1). Here the pairing is between an electron and a hole, and the crossover is controlled by the inter-particle spacing $n^{-1/d}$, which is in turn controlled by the external pumping

density. The exciton (polariton) gas behaves as a weakly interacting Bose gas when the density is low ($n_{exc} \ll n_{Mott}$), with the scattering length approximated by the exciton Bohr radius a_B. Increasing the exciton density to around n_{Mott}, a_B becomes comparable to particle spacing and the system is in the BEC-BCS crossover regime. At high densities, we have an electron and hole plasma with screened Coulomb interactions, which coherently couple to a cavity photon field.

In the current thesis, however, we focus on the BEC regime of polaritons, where the excitation density is below the exciton saturation density, and the bosonic description of polaritons and excitons are valid.

3.8   Summary

In summary, we reviewed in this chapter the definition and properties of quantum-well microcavity polaritons, and their uniqueness for BEC research. In the next chapter, we explain the actual samples used for this thesis and how they are characterized experimentally.

Chapter 4

Experimental Systems

4.1   Sample Materials and Structures

An optimal microcavity system for polariton BEC shall have:

1. High quality cavity, hence long cavity photon and polariton lifetime.

2. Large polariton-phonon and polariton-polariton scattering cross-section, hence efficient polariton thermalization.

3. Small exciton Bohr radius and large exciton binding energy, hence high exciton saturation density.

4. Strong exciton-photon coupling, hence small decoherence rate. It requires both large exciton oscillator strength and large overlap of the photon field and the QWs.

To address these issues, a careful choice of material is important. For given material, the exciton saturation density and exciton-photon coupling also depend on the structure design.

4.1.1   Choice of Material

The choice of direct bandgap semiconductor depends first on the epitaxial growth technology – that is, whether or not a high quality quantum structure can be fabricated. The best fabrication quality of both quantum well and microcavity has been achieved with Al_xGaAs ($0 \leq x \leq 1$), due to the close match of their lattice constants and relatively large bandgap difference: at 4 K, GaAs has a_{lat} =5.64 Åand E_g =1.519 eV, AlAs has a_{lat} =5.65 Åand E_g =3.099 eV. Nearly strain and defect free GaAs QWs are now conventionally grown between Al_xGaAs with inhomogeneous broadening of exciton energy limited mainly by mono-layer QW thickness fluctuation. Nearly defect-free microcavity structures are grown with ∼30 AlAs/GaAs pairs in DBRs and cavity $Q \sim 2 \times 10^4$.

One limitation on a higher Q is the number of layers in the DBR. It is difficult to grow a large number of layers in a structure, because growth conditions vary with time, also because effects of strain and defects in lower layers (layers grown earlier) accumulate and propagate to later grown upper layers. Another constraint on Q is the relatively small refraction index contrast between GaAs and AlAs (section 3.4). If GaAs QWs are used in a microcavity, DBRs must be made of $AlAs/Al_xGaAs$ with a large enough x so that the DBRs are not absorptive at the polariton energies. $x \leq 0.15$ is often used with $n_1/n_2 \sim 1.17$ for the DBR layers.

An alternative is to use In_xGaAs QWs instead, and use GaAs/AlAs DBRs. InAs has $a_{lat} = 6.05$ Å, $E_g = 0.417$ eV. With $0.03 < x < 0.1$, there is enough QW confinement and tolerable strain. However, In_xGaAs has a larger Bohr radius and smaller oscillator strength, rendering it less suitable for BEC study than GaAs-QW microcavities.

Another popular choice is the CdTe-based II-IV system, with CdTe QWs and Mg_xCdTe and Mn_xCdTe barrier and DBR layers. The larger lattice mismatch is compensated by larger binding energy and larger oscillator strength (hence more tolerant for inhomogeneous broadening), as well as larger refraction index contrast (hence less layers needed in DBRs). The smaller Bohr radius of CdTe excitons also allows a

larger saturation density. The problem with this material system is the less efficient polariton-phonon scattering. Thus a pronounced energy relaxation bottleneck often persists, which prevents condensation in the LP ground state (30; 31).

More recently, a lot of efforts are devoted to developing GaN and ZnSe based material systems with small lattice constants. They have a much larger exciton binding energy and bandgap, hence promise room temperature operation at visible or ultra-violet wavelengths. Yet the growth and fabrication techniques are still far from mature, and samples in the strong-coupling regime are rarely available at present.

In summary, we choose GaAs-based samples for studying fundamental properties of microcavity polaritons, mainly based on the following two considerations:

1. Best growth quality of the microcavity and quantum well – due to good lattice matching between AlAs and GaAs and well developed fabrication techniques.

2. Efficient energy relaxation to branch-bottom – due to relatively large Bohr radius and scattering cross-sections.

The compromise is a relatively low saturation density and small oscillator strength compared to systems with smaller Bohr radii. Fortunately, multiple narrow QWs can be used to alleviate these problems without much sacrifice in the sample quality.

Table 4.1 compares the most relevant parameters of these various materials, they are used for all calculations in this thesis.

4.1.2 Structure Design Considerations

Since the exciton-photon coupling scales as the square root of the field amplitude and field-exciton overlap, to achieve maximum exciton-photon coupling, a short cavity is preferred with narrow QWs placed at its antinode(s). A $\lambda/2$ cavity gives the largest field amplitude at the cavity center for given reflectance of the DBRs. A narrow QW in general leads to smaller Bohr radius and enhanced oscillator strength (section 3.3.2 and figure 3.7). To increase the field-exciton overlap, one can use multiple closely spaced narrow QWs, and even put QWs in the two antinodes next to the central one

Table 4.1: Comparison of Material Parameters

	GaAs	CdTe	GaN	ZnSe
refraction index n (at E_{exc})	3.60	3.26	2.44	2.8
lattice constant a (nm)	0.5642	0.6482	0.3189	0.5677
heavy hole in-plane mass $m_{hh\|}$ (m_e)	0.111	0.4	--	0.78
band gap E_g (eV)	1.519	1.60	3.507	2.670
QW thickness d (nm)	7	8	2-3	2-3
Bohr radius a_B (nm) (bulk/QW)	~15/9	~5/2.8	~3	~3
binding energy E_B (meV)	~10	~25	~20	~20
single-QW Rabi splitting Ω (meV)	4.3	7	--	--
exciton saturation density per QW I (cm^{-2})	4 x 10^{10}	5 x 10^{11}	10$^{11\sim12}$	10$^{11\sim12}$

- Temperature used is 4 K for GaAs and CdTe, and 300 K for GaN and ZnSe.
- A value is not quoted when no accurate value available.

— so long as the field amplitude is more or less uniform at all QW positions. The difference in field amplitude E at each QW has an effect similar to inhomogeneous broadening of the QW exciton linewidth (60). Using multiple and narrow QWs has another important benefit — an increased total saturation density of excitons, which scales with N/a_B^2. It becomes critical when studying the nonlinear properties of polaritons.

Details of the structure and compositions of samples used in this thesis are given in appendix A, including: S-CdTe, a double-CdTe QW $\lambda/2$ microcavity, and S-GaAs-I and S-GaAs-II, two sample both with twelve-GaAs QW in a $\lambda/2$ microcavity. Most studies are carried out with S-GaAs-I and S-GaAs-II, the structure is depicted in figure A.1. To maximize the overlap of the photon field and excitons, we use a $\lambda/2$-cavity and distribute the QWs among the three central anti-nodes of the cavity field. $N_{QW} = 12$ QWs are used, so the oscillator strength Ω is increased by a factor of $\sim \sqrt{12}$ to $\Omega = 7.5$ meV. Ω becomes comparable to the binding energy of a bare exciton $E_b \approx 10$ meV, thus the effect of 'very strong coupling' is expected to further enhance the exciton-photon coupling and shrink the exciton Bohr radius. Moreover, using twelve QWs also reduces the exciton density per QW by a factor of 12 for a given total polariton density. This helps to avoid exciton saturation before reaching the polariton phase transition threshold.

4.2 Reflection Measurement

One first experiments to carry out with a sample are to find its eigen modes, such as by a reflection measurement. Reflection measurement with low-intensity input light is a passive measurement which gives the eigen modes of the undisturbed system, as shown by the transfer matrix calculation results (section 3.4 and 3.5).

4.2.1 The Setup

Figure 4.1 shows two experimental setups for measuring reflectance of a microcavity sample at low temperature. The sample is attached to a copper sample holder in a
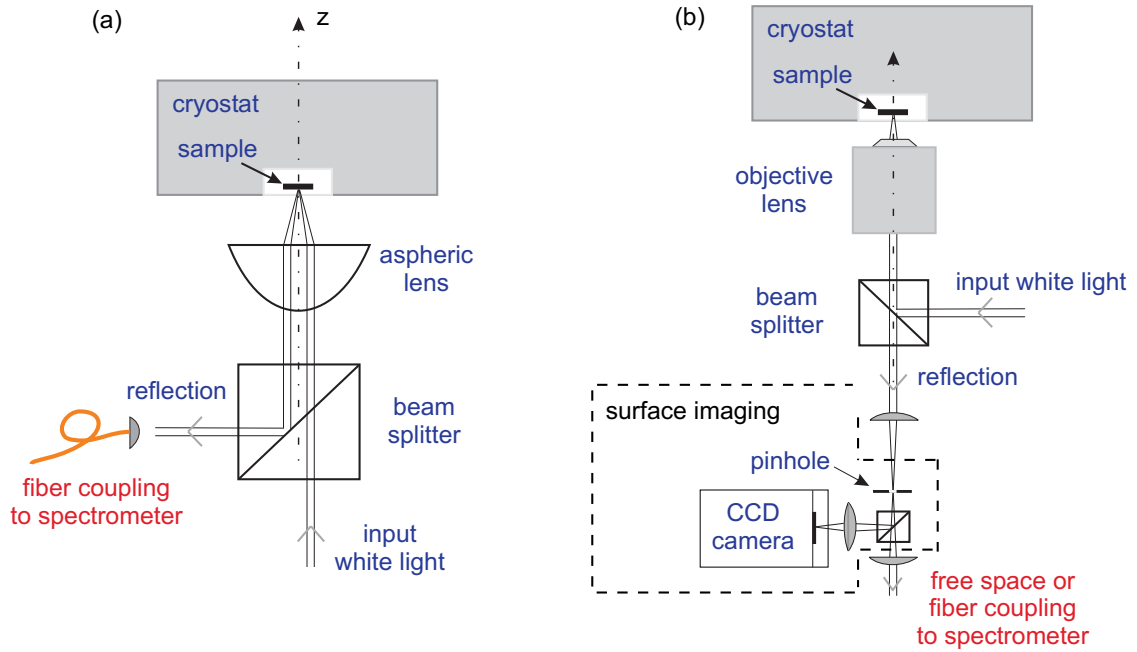
Figure 4.1: Setup for reflection measurement, (a) using an aspheric lens with a large diameter, (b) using an objective lens.

vacuum chamber by indium solder or vacuum grease, the sample holder is cooled by continuous flow liquid Helium.

The setup in figure 4.1 (a) uses a large diameter aspheric lens as both focusing and collection lens. An input beam is aligned parallel to the the optical optical axis with a displacement Δx, and is focused onto a spot ~ 100 μm in diameter on the sample surface with an incident angle $\theta \sim \arctan(\Delta x/f)$ (f is the focal length of the lens). The reflected beam is picked up by a thin mirror or a beam splitter and sent into a spectrometer which records its $I(\lambda)$. If the sample is replaced by a reference mirror with reflectance R_{ref}, then the ratio of the two reflected intensities corrected by R_{ref} gives the reflectance of the sample. This setup is relatively simple and angle-resolved reflectance is conveniently measured for $\theta < 20°$ with a resolution $\Delta\theta \sim 6°$. θ and $\Delta\theta$ are limited mainly by the input beam width (~ 4 mm) and effective lens diameter (~ 30 mm). This setup is most suitable when the sample surface is relatively far away from the cryostat's front window and there is no small-structures on the sample surface (such as steep change of cavity length or pillar structures, etc.). We normally use a 200 W halogen lamp as the input light, which has a relatively flat spectral
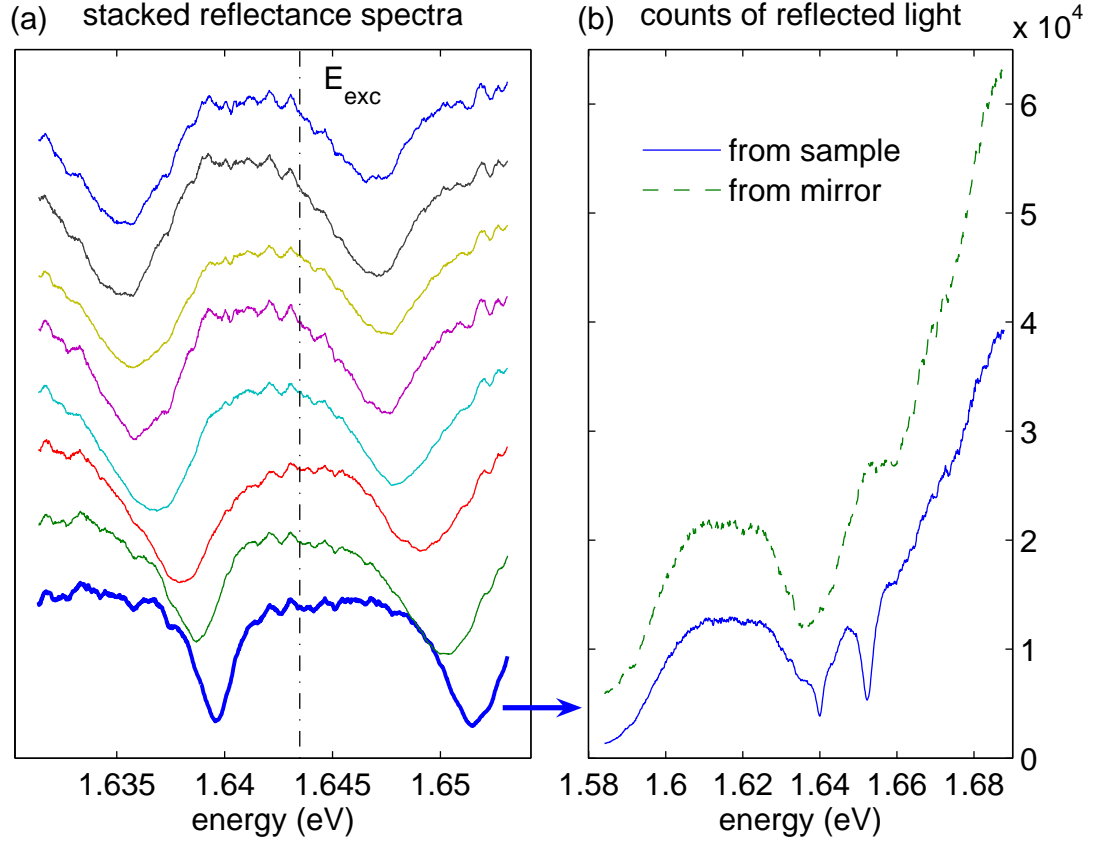
Figure 4.2: (a) Measured reflectance of sample S-CdTe-I. (b) Raw reflection spectra from the sample and from the reference mirror, corresponding to the bottom spectrum in (a).

distribution and supplies sufficient intensity at the near-infrared spectral region of interest.

Figure 4.2 (a) shows a set of reflection spectra measured for S-CdTe with this setup at detuning $\Delta \sim 0$ and $\theta = 0$. The dips at the resonances are deep and broad, indicating large linewidth of the uncoupled exciton and photon modes. Figure 4.2 (b) gives an example of the raw reflection spectra from the sample and from the reference mirror, the latter is a product of the white light spectral distribution and the spectrometer response function.

The setup in figure 4.1 (b) works in the same way except that an objective lens is used in place of the aspheric lens. An objective lens in general has a short working distance and small aperture, hence the sample surface needs to be very close to the
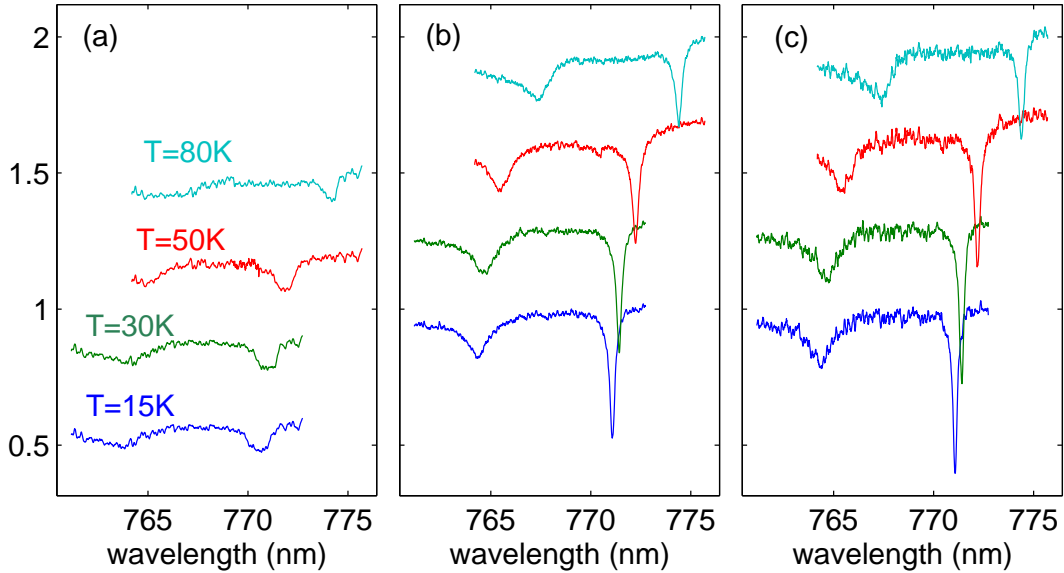
Figure 4.3: Reflectance spectra of sample S-GaAs-III at different temperatures, measured with different NA of the collection optics: (a) NA $\sim$ 0.5, (b) NA $\sim$ 0.2, (c) NA < 0.1.

window ($\sim$ 1 mm for Janis ST-500 cryostat), and angle-resolved measurement is difficult. The upside is that the input beam can be focused to a very tight spot by using a near-Gaussian input beam and an objective with a large numerical aperture (NA). Sample surface illumination and imaging are also conveniently integrated with this setup. Hence it is most useful when one wants to closely monitor the position of the spot on the sample surface.

With a proper choice of the objective's NA and a pinhole in the reflection path, $\Delta\theta$ can be controlled accurately. Smaller $\Delta\theta$ can be achieved at the expanse of collection efficiency and is only limited by the signal-to-noise ratio of the measured reflectance spectra. Figure 4.3 compares how the data quality is influence by NA (or, $\Delta\theta$) of the collection optics. With increasing NA, the resonance dip is broadened by contribution from modes with $k_\parallel > 0$, due to the relatively steep increase of LP energy with in-plane wavenumber.When too large a NA is used, shallow resonances are even masked by noise (such as the resonance at the shorter wavelength in the top of Figure 4.3 (a)).

4.2.2   Cavity Tuning

These reflection spectra reveal a few pieces of importation information about the sample. Firstly, we notice that, in figure 4.2 (a) and figure 4.4 (a), the double resonances tune with the position on the sample. This is because there is a natural wedge of the cavity length by growth, and the cavity resonance is tuned across the sample while the QW exciton resonance is constant within its linewidth. Anti-crossing of the double resonances vs. position on the sample clearly confirms that the sample is in the strong coupling regime. By fitting the tuning curves, we can find the exciton resonance and the normal mode splitting at zero detuning, as illustrated in figure 4.4 (b). Finally, the depth and width of the resonance dips are indicators of the quality of the microcavity. At a large negative detuning, the linewidth of a dip corresponding to the photon-like mode gives a good estimate of the linewidth, hence the lifetime, of the uncoupled cavity mode.

4.3   Photoluminescence Measurement

As discussed in section 3.5, an internal polariton of certain k decay with a fixed rate $\gamma_{LP}(k)$ to an external photon mode at certain angle θ with the same energy $E_{LP}(k)$ and inplane wavenumber k. Hence dynamical and statistical properties of polaritons are directly conveyed to the external photon flux; polaritons are directly and conveniently studied by their photoluminescence (which should be distinguished from the conventional photoluminescence due to radiative recombination of a quasi-particle). Conversely, polaritons can be resonantly pumped to a chosen state by a laser. In all the experiments discussed here, we use a mode-locked Ti-Sapphire laser with a pulse duration of ~ 3 ps and a repetition rate of 78 MHz.

4.3.1   Momentum Space Mapping

Figure 4.6 shows a typical setup for angle-resolved photoluminescence measurements. A doublet lens focuses the incident pump beam from a slant angle to a spot 15 to
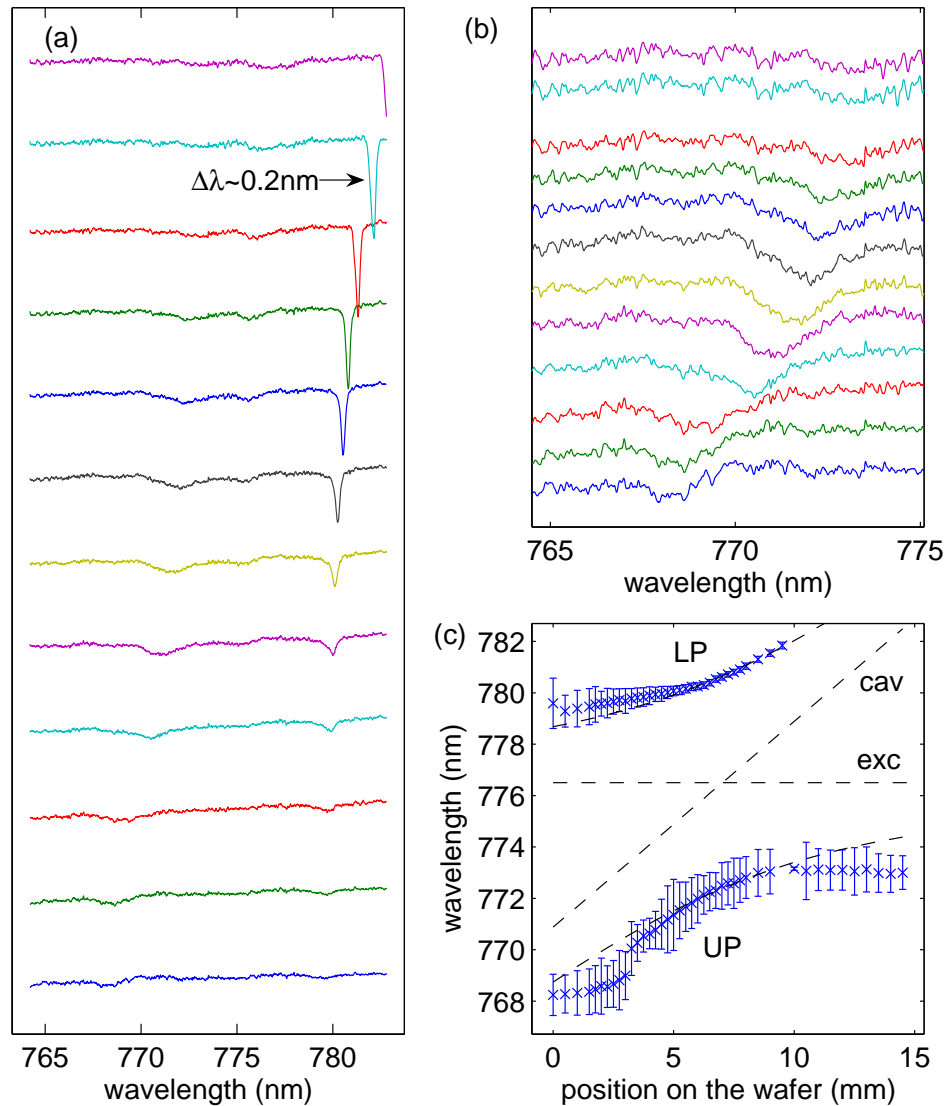
Figure 4.4: (a) Reflection spectra of S-GaAs-II at various positions on the sample, showing anti-crossing of the resonances. (b) Same as (a), focusing on the shallow UP resonance. (c) LP and UP energies obtain from (a) (crosses), error-bar corresponds to the width of the reflectance dip. Dashed lines are the fitted LP, UP, and uncoupled exciton and photon energies.
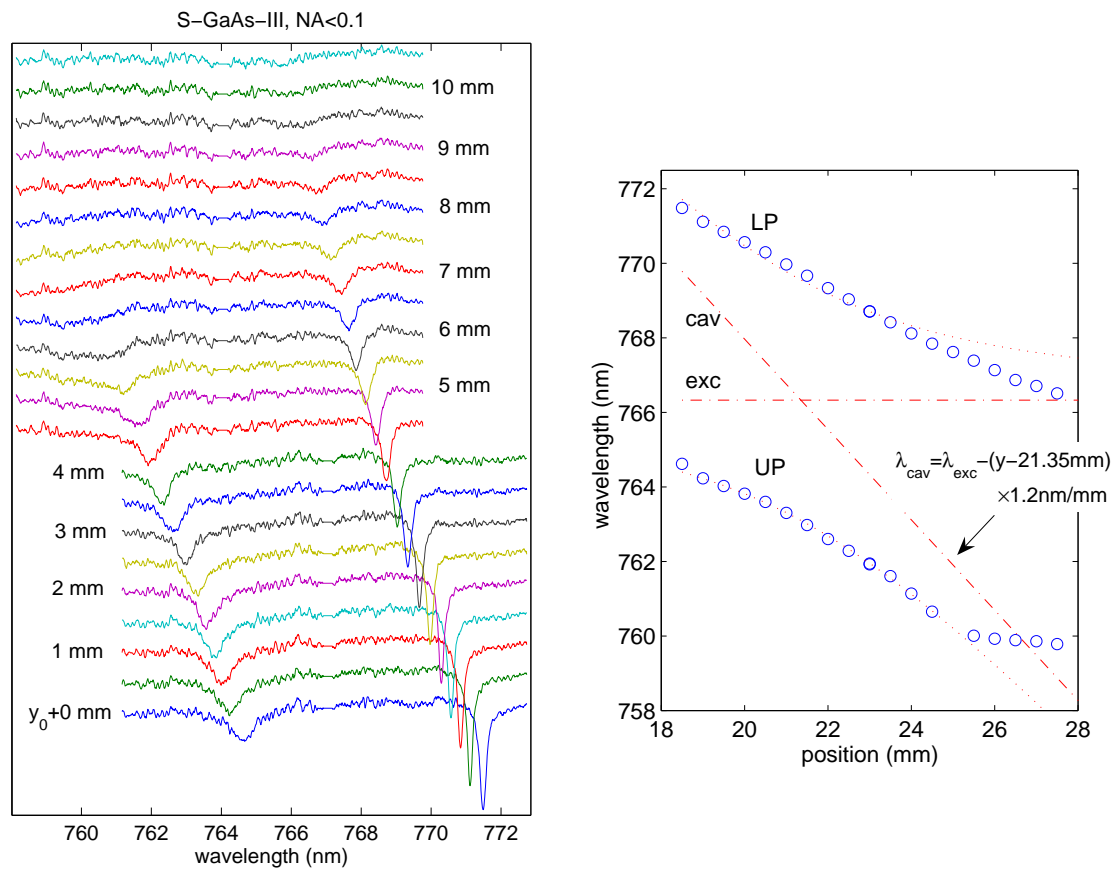
Figure 4.5: (a) Reflection spectra of S-GaAs-III at various positions on the sample, showing anti-crossing of the resonances. (b) LP and UP energies obtain from (a) (circles) fitted by equation (3.55), assuming the cavity tuning function shown (lines).
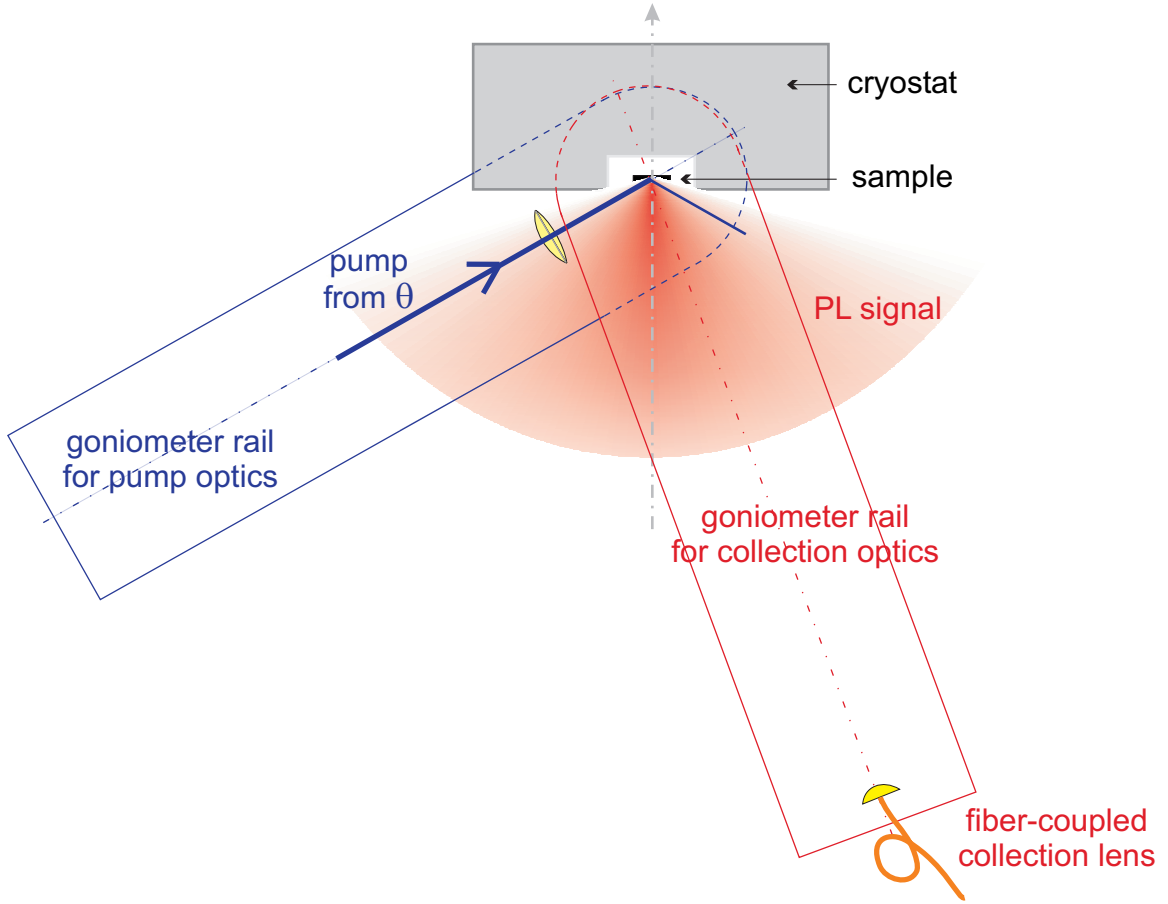
Figure 4.6: Illustration of the experimental setup for angle-resolved photolumines-cence measurement.

50 μm in diameter on the sample. The emission is collected by a fiber-coupled lens with an angular resolution of $0.5° - 1°$ which is in turn connected to a spectrometer. Both pump and collection optics are on the extended rails of a goniometer centered at the sample. In this way, a wide range of incidence and collection angles can be accessed corresponding to different momentum states of polaritons.

Figure 4.7 (a) shows a 2D plot of a serial of recorded spectra from S-GaAs-II at zero detuning. The collection angle θ is scanned from $-30°$ to $+30°$ with $1°$ increment. Pump is resonant with the bare exciton energy at 1.597 eV and arrives from $45°$ relative to the sample growth direction. UP is not populated $(E_{UP} - E_{LP} \sim 50 k_B T)$ and only the LP emission is detected. From the LP peak position at each angle, we map out the LP energy dispersion vs. the LP in-plane wavenumber $k_\parallel$ and compare it to the calculated ones. By integrating over each LP peak and taking into the account
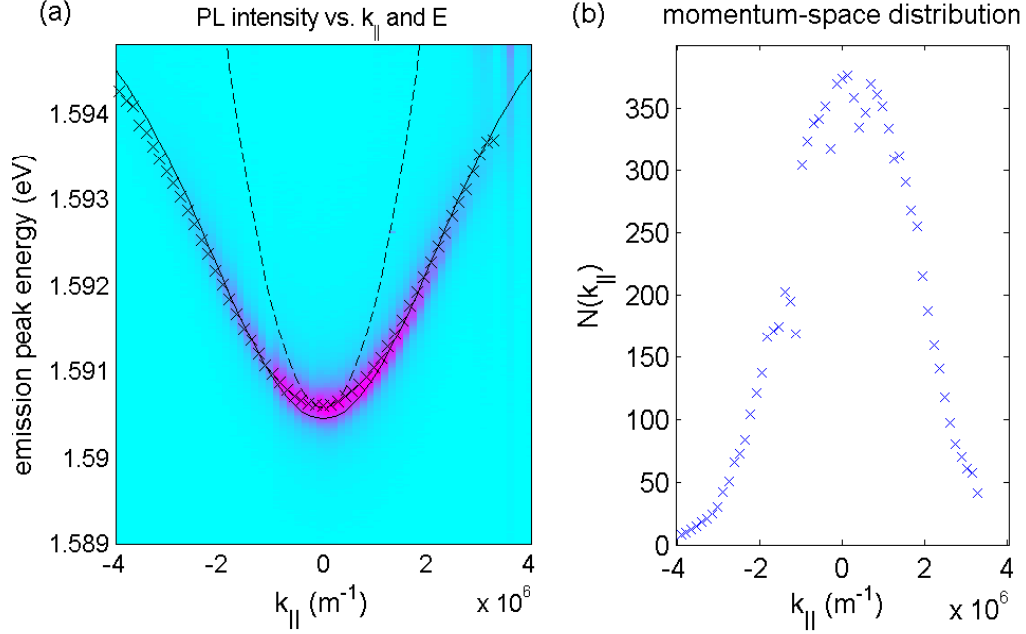
Figure 4.7: (a) A 2D plot of the photoluminescence intensity from S-GaAs-II at $\Delta = 0$ vs. energy and in-plane wavenumber. The crosses are emission peak positions, the solid line is the calculated LP dispersion, and the dashed line is the calculated cavity dispersion with its origin off set to compare with the LP dispersion. (b) The LP momentum distribution obtained from (a).

the LP DOS, the momentum distribution of LPs is obtained as shown in (b).

If serials of angle-scanned spectra are taken at different positions on the sample, we obtain a set of dispersion curves measured by photoluminescence. We can fit these curves with the LP dispersion in equation (3.55). The exciton resonance E_{exc} and LP-UP splitting $2\hbar\Omega$ are two common fitting parameters for all the curves, and detuning Δ at $k_{\parallel} = 0$ is a curve dependent fitting parameter. Good agreement between fitting and experimental curves are obtain as shown in figure 4.8, thus obtained E_{exc} and $2\hbar\Omega$ are also consistent with results from the reflection measurement.

4.3.2   Real Space Imaging

Complimentary to the momentum-space mapping, the setup in figure 4.9 images the real-space polariton distribution using an objective lens with a large NA (0.55–0.65). The image is recorded by a charge-coupled camera. The overall resolution is 1–2μm.
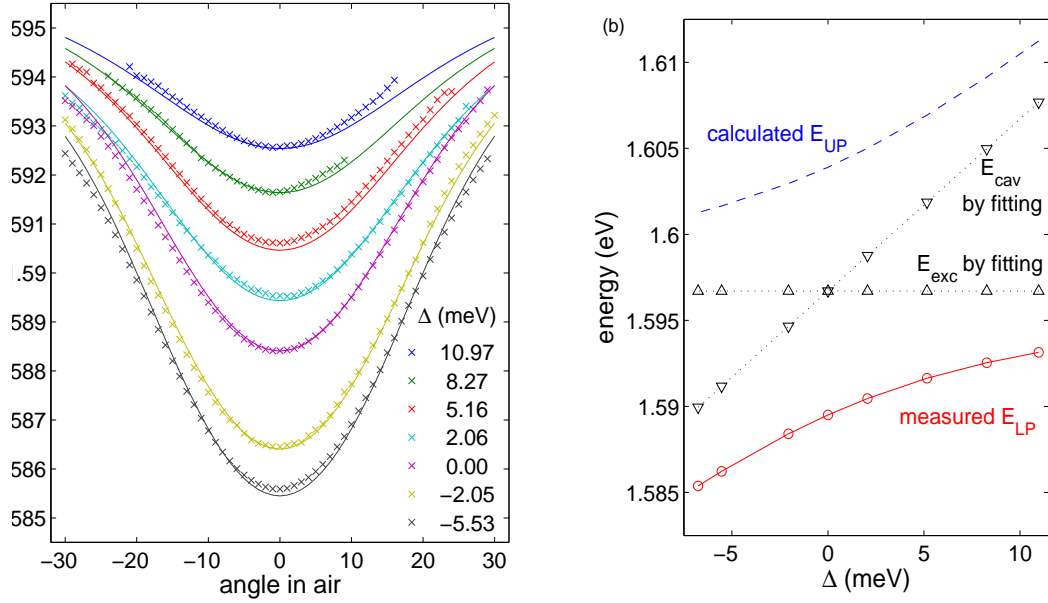
Figure 4.8: (a) Dispersions measured by photoluminescence at different positions on sample S-GaAsII with a weak pump (symbols), and fitting by (3.55) (lines). (b) Polariton energy dispersions vs. detuning. Fitting of the dispersions in (a) gives E_{exc} and E_{cav}, using which E_{UP} is also calculated.

The incident pump beam in this setup can arrive either from a large $\theta_{in} > 50°$ or from $z-$direction at $\theta_{in} = 0°$. The former case allows resonant pumping of corresponding polariton modes. The latter case allows a tightly focused pump spot down to $2\mu m$ in diameter, yet the objective also collects intense back reflected and scattered pump light and the pump wavelength often needs to be far off the signal's wavelength. Figure 4.10 (a)–(c) show three recorded luminescence images from of S-GaAs-I at zero-detuning position, pumped resonantly from $\theta_{in} = 50°$. Both the scattered pump and PL signals are detected in (a). A narrow bandpass filter in the collection path can be used to filter out either the scattered pump (in (b)) or the LP signal (in (c)). At a higher pump level, the LP signal grows to much stronger than the scattered pump, and only the LP signal is detected within the dynamic range of the streak camera, as illustrated in (d).

If a pinhole is placed at the image plane of the sample, it serves as a spatial filter for measuring photoluminescence from selected regions on the sample surface.
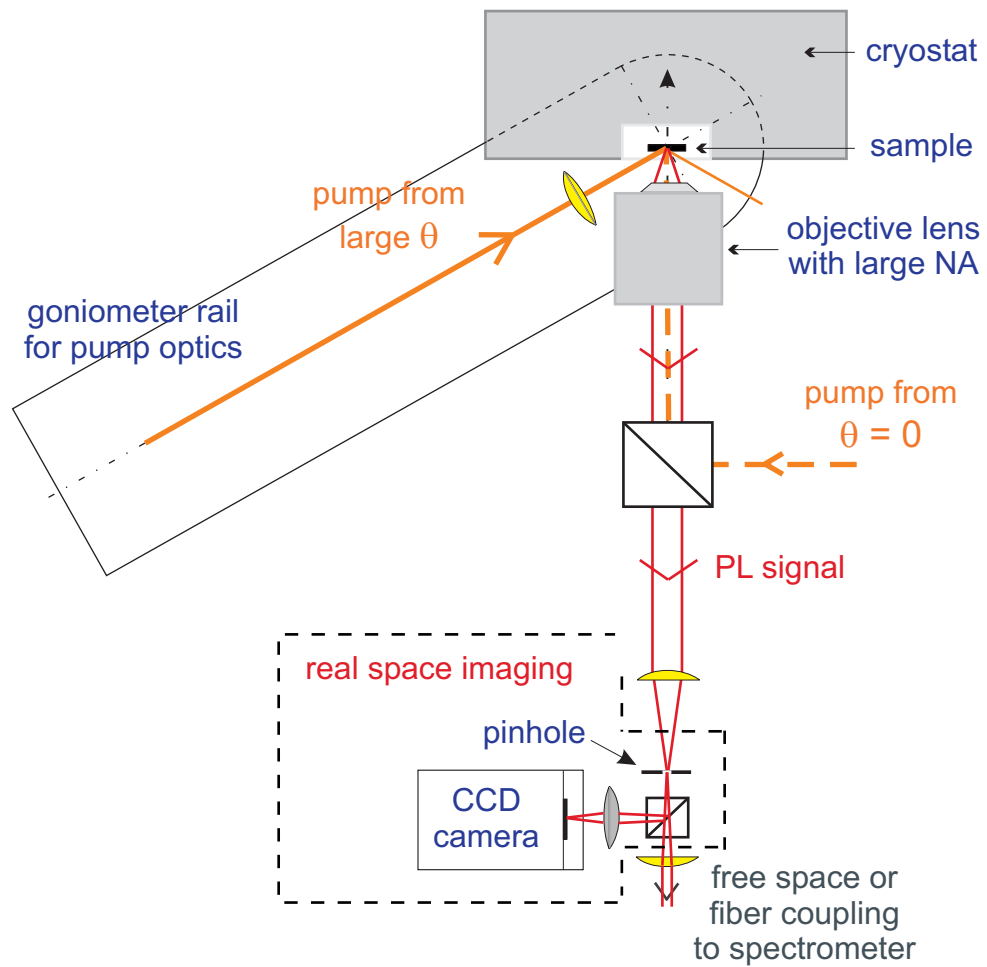
Figure 4.9: Illustration of the experimental setup for real space imaging.
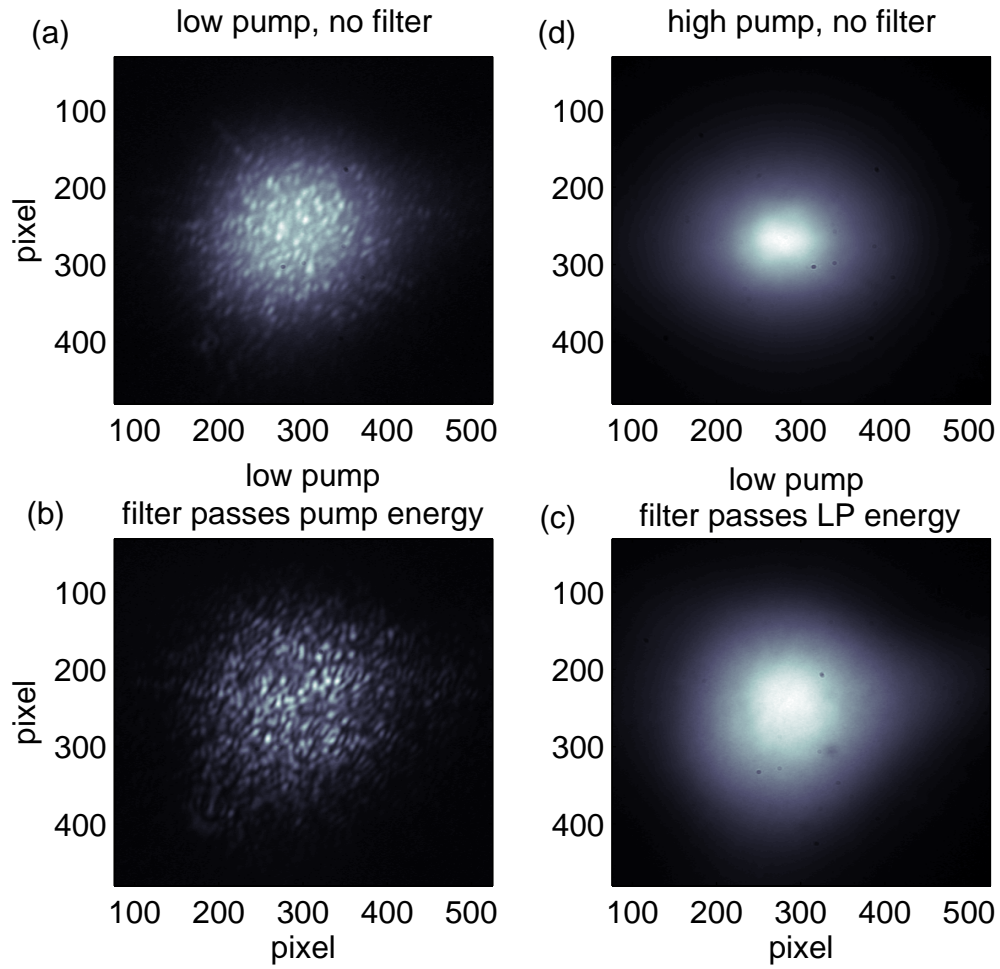
Figure 4.10: Real space images of S-GaAsI at zero-detuning position. (a), (b), (c) are of the same pump power, with (a) no filter, (b) with a bandpass filter set to pass pump energy, and (c) with a bandpass filter set to pass the LP energy. (d) is of a higher pump power without filter.
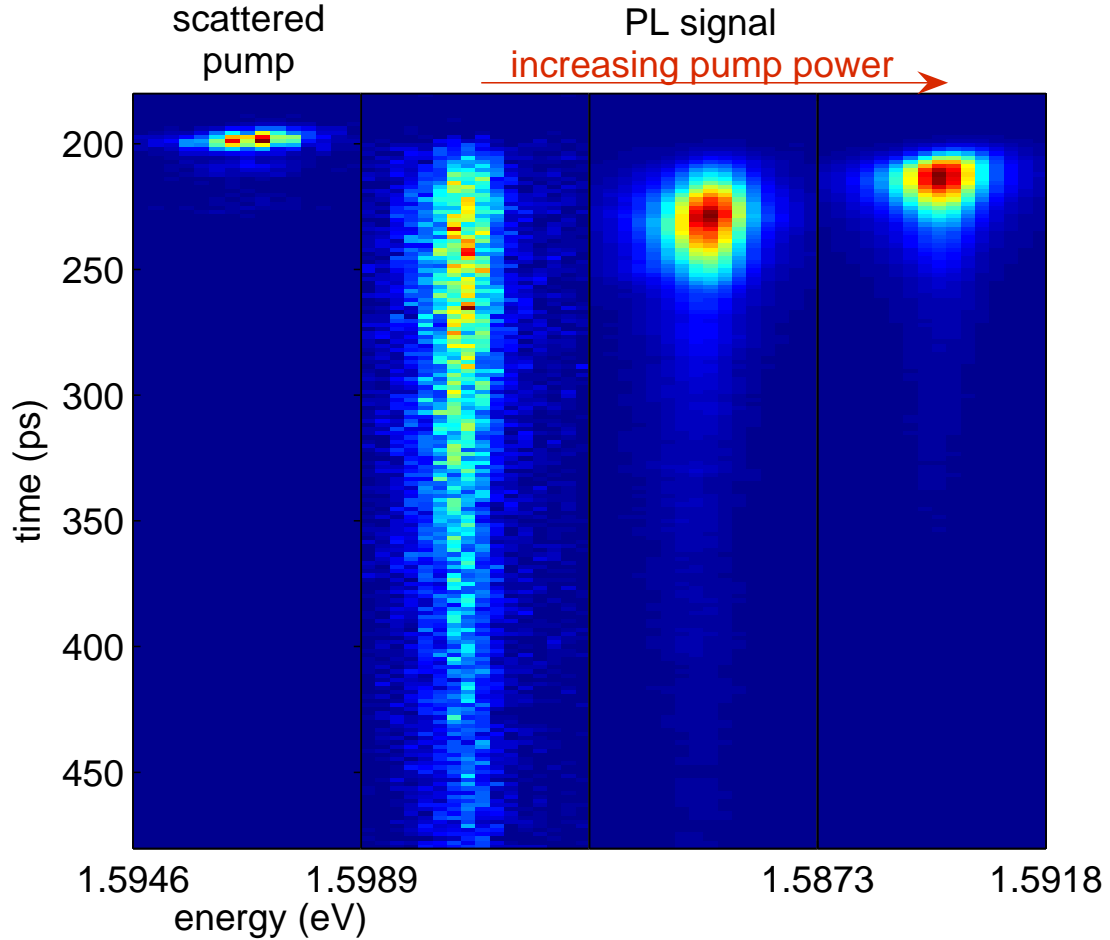
Figure 4.11: Streak camera images.

4.3.3 Time Resolved Measurement

If the collected light is sent to a streak camera, time resolved photoluminescence is measured. We use a Hamamatsu Streak Camera with a time resolution < 2 ps. A 50 cm monochromator is attached to the front of the streak camera which may degrade the time resolution. When using the lowest grating of the spectrometer with 100-grooves per millimeter and a spectral resolution of ~ 1 nm, the time resolution increases to ~ 3 ps. The streak camera is triggered by the same mode-locked Ti-Sapphire laser used for pumping. Instability of the mode-locked laser operating in the pico-second mode causes time jitters of the streak signal, hence in practice, with an average integration time of about one minute per spectrum, the time resolution is 4 to 5 ps.

Figure 4.11 shows a few examples of the measured, angle-resolved and time-resolved spectra. The first panel is in the spectral window near the pump energy, and a faint scattered pump signal is recorded, which serves as the time-zero in pulsed experiments.

4.3.4   Intensity Correlation Measurement

If the collected light is sent into a Hanbury Brown-Twiss (HB-T) type setup, the time domain auto-correlation $g^{(2)}$ of the emission measured. Figure 4.12 illustrates one HB-T setup we used. Emission light collected by a multi-mode fiber is sent to a 50/50 beam splitter and to two EG&G single-photo-counters-modules (SPCMs) consisting of low noise photo avalanche diodes. The output of the SPCMs are then sent to a time-to-amplitude converter (TAC) which is in turn connected to a multi-channel analyzer (MCA). The MCA records a histogram of the time intervals $\tau = t_1 - t_2$ between the detection of one photon at t_1 by a first SPCM (the one labeled as 'start') and the detection of a second photon at t_2 by the second SPCM (the one labeled as 'end').
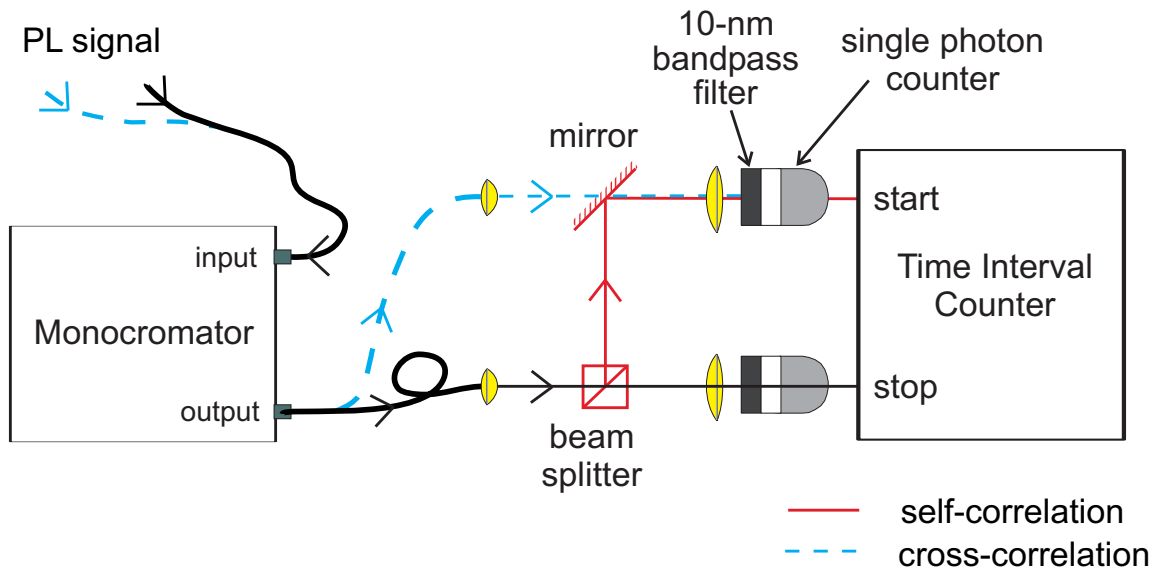
Figure 4.12: A realization of Hanbury Brown-Twiss measurement with single photon counters. For auto-correlation measurement, use a single-core fiber, the beam splitter and the mirror (red solid path). For cross-correlation, use a double-core fiber bundle to carry the two input and output signals (blue dashed path).
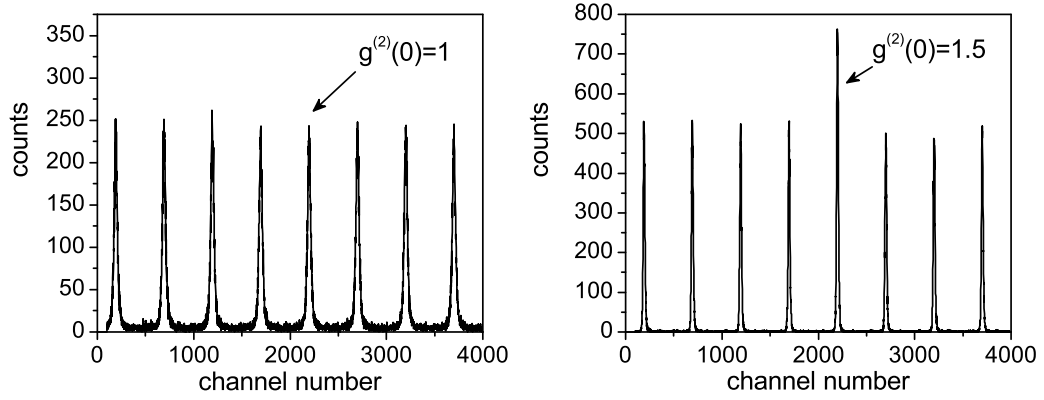
Figure 4.13: Histograms corresponding to $\tilde{g}^{(2)}(0) = 1$ and $\tilde{g}^{(2)}(0) = 1.5$.

We shielded the setup as well as the fibers with black flock paper and tape, and measured dark counts of the SPCMs are $150 \sim 300$ s^{-1} which sets the lower bound of the measurable intensity of the photon flux. After each detection event, the SPCM has a dead time of about 50 ns before it can detects a second event, hence the photon flux should be attenuated when necessary to keep a count rate well below ten million per second. The time resolution of the SPCMs are about $T_r \sim 0.5$ ns.

In our pulsed experiments, $T_r \sim 0.5$ ns is much shorter than the pulse repetition period $T_{rep} = 13$ ns, but much longer than the emission pulse width. Hence the recorded histograms consist of equally spaced peaks separated by T_{rep}, with the width of each peak determined by T_r. In between pulses, there is no photon flux, and only dark counts contribute to a non-zero floor of the histogram. A couple example histograms and corresponding $\tilde{g}^{(2)}(0)$ are shown in figure 4.13.

If we collect light from two different modes of the LPs, and send them into the SPCMs without passing the beam splitter (the blue dashed path in figure 4.12), we measure instead the cross-correlation function of the two modes.

4.4   Summary

In this chapter, we first reviewed a few important considerations for choosing a material system and designing a sample structure for microcavity polariton research.

Given QW-microcavity, the very first sample characterization is to find out wether or not strong-coupling regime is reached, by a measuring the anti-crossing behavior of resonance modes in the system, and the characteristic dispersions of the polaritons. Both can be measured by reflection or photoluminescence measurements. Photoluminescence measurement is a particularly powerful tool for microcavity polariton systems because the emitted photons carry direct and mode-specific information of the internal polaritons.

In the next chapters, we use the experimental tools introduced here to study the dynamical and statistical properties of the multiple-QW microcavities.

Chapter 5

Quantum Degeneracy Threshold

In previous chapters, we reviewed the basics of Bose-Einstein condensation and microcavity polaritons, discussed the advantages of polariton for BEC study, and introduced the experimental techniques for studying a polariton system. In this chapter and the next, we continue with an experimental exploration of polariton condensation. First and foremost: can we reach a quantum degeneracy threshold in a polariton gas?

5.1   Population Dynamics of LPs

To answer this question, we first look into the population dynamics of a microcavity polariton system. In general, hot polaritons are excited by a pumping laser at certain energy $E_{LP}(k_\parallel)$ and wavenumber $\boldsymbol{k}_\parallel$, they thermalize among all states with the same $|k_\parallel|$ and E_{LP} in sub-picosecond time scale via elastic Rayleigh scattering at weak disorder potentials. This momentum relaxation happens much faster than energy relaxation and decay of the LPs, hence we often consider the momentum relaxation as instantaneous and assume cylindrical symmetry of the system. Then these hot LPs thermalize to states with lower energies by phonon scattering and higher order scattering processes, while at the same time decay out of the system by the out-coupling of the photon component.

Rate Equation for LP Energy Relaxation

Assuming instant momentum relaxation and cylindrical symmetry, the polarization-independent dynamics of LPs can be described by the following semiclassical Maxwell-Boltzmann rate equations:

$$
\begin{aligned}
\frac{dN_{k_\parallel}}{dt} =& P_{k_\parallel} - \frac{N_{k_\parallel}}{\tau_{k_\parallel}} - \sum_{k_\parallel'} W_{k_\parallel,k_\parallel'} N_{k_\parallel}(N_{k_\parallel'}+1) + \sum_{k_\parallel'} W_{k_\parallel',k_\parallel} N_{k_\parallel'}(N_{k_\parallel}+1) \\
& - \sum_{k_{\parallel 1},k_\parallel',k_{\parallel 1}'} Y_{kk_1,k_\parallel'k_{\parallel 1}'} N_{k_\parallel} N_{k_{\parallel 1}}(N_{k_\parallel'}+1)(N_{k_{\parallel 1}'}+1) \\
& + \sum_{k_{\parallel 1},k_\parallel',k_{\parallel 1}'} Y_{k_\parallel'k_{\parallel 1}',kk_1} N_{k_\parallel'} N_{k_{\parallel 1}'}(N_{k_\parallel}+1)(N_{k_{\parallel 1}}+1),
\end{aligned}
\tag{5.1}
$$

where the subscript $k_\parallel$ denotes the mode of inplane wavenumber $k_\parallel$, $N_{k_\parallel}$ is the LP population per mode, $P_{k_\parallel}$ is the pumping at each mode, $\tau_{k_\parallel}$ is the LP decay rate, $W_{k_\parallel,k_\parallel'}$ is the acoustic phonon scattering coefficient from mode $k_\parallel$ to $k_\parallel'$, and $Y_{kk_1,k_\parallel'k_{\parallel 1}'}$ is the LP-LP scattering coefficient from initial states $k_\parallel$ and $k_{\parallel 1}$ to final states $k_\parallel'$ and $k_{\parallel 1}'$.

It is through the exciton component that LPs scatter with phonons and other LPs. The scattering coefficients for both processes are computed using the Fermi's Golden Rule. The LP-phonon scattering is mainly mediated by the deformation potential (61), it conserves the energy and in-plane wavenumber. k_z, however, is not conserved, due to the confinement in the $z-$direction. Hence phonon scattering is much stronger in a QW than in bulk. LP-LP scattering, or, exciton-exciton scattering weighted by the exciton fraction of the LPs, results from mainly the exchange Coulomb interaction of the electron and hole constituents in excitons, and the excitation saturation effect due to the Pauli exclusion principles. Normally the Coulomb exchange interaction is larger than the exciton saturation, both are of the order $(E_B^2 a_B^4)/L^4$. The total scattering rate is quadratic with the exciton density, for given n_{exc}^{QW} per QW, it scales with the number of QWs N_{QW}. In contrast, the phonon scattering rate is linear with the exciton density and stays the same for any N_{QW}.
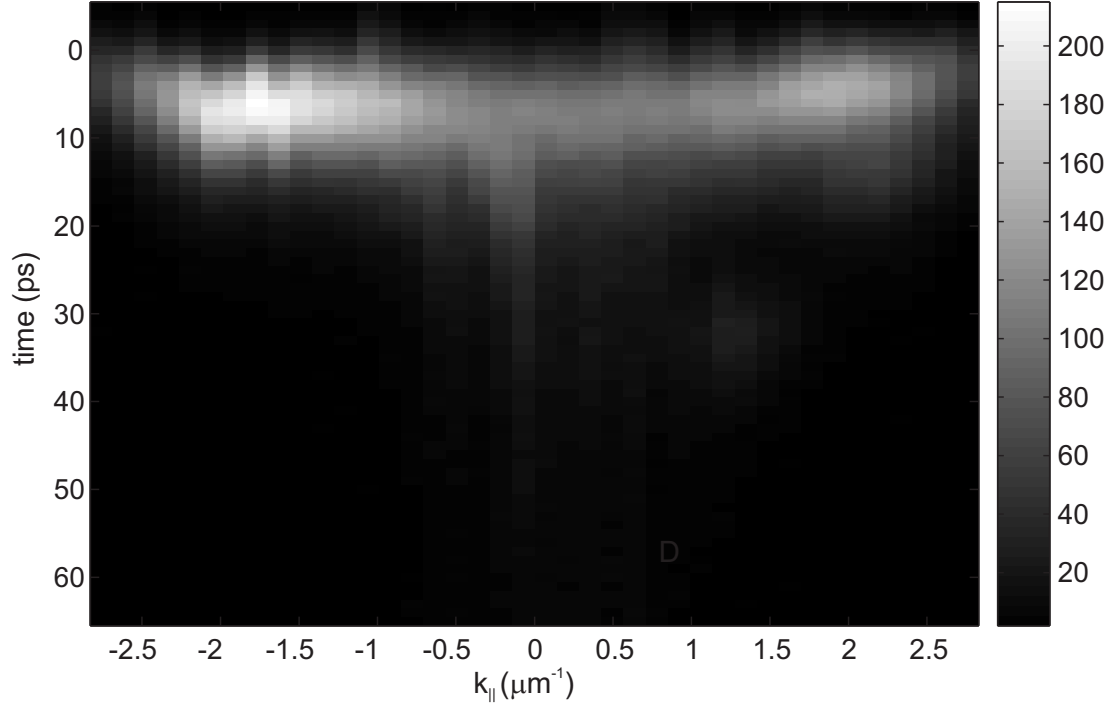
Figure 5.1: Evolution of LP population distribution $N_{LP}(k_\parallel)$ showing showing the energy relaxation bottleneck at $k_\parallel \sim 2~\mu m^{-1}$. Used detuning $\Delta = -4.3$ meV.

Bottleneck Effect at Low Densities

When pumping density is relatively low, commonly observed is an energy relaxation *bottleneck* as shown in figure 5.1.

It can be understood in light of the peculiar dispersion of the LPs. Above the bottleneck region, LPs are mostly exciton-like, lifetime is long, energy DOS is large, the change of energy with $k_\parallel$ is gradual – these exciton-like LPs are efficiently thermalized by phonon scattering. Below the bottleneck region, the LP energy DOS drops by four orders of magnitude (due to the decrease of the LP effective mass, see section 3.5), while their lifetime also shorten by two orders of magnitude to $1 \sim 10$ ps. At the same time, the LP energy decreases by 10 to 20 times the phonon energy at the temperature of 4.2 K. Hence when $N_{k_\parallel} \ll 1$, the phonon scattering, at a rate of about once per pico-second, becomes insufficient to thermalize the LPs before they decay. Detailed numerical and experimental studies of the bottleneck effect have been carried out by many groups (62; 63; 64; 30).

Stimulated Scattering at Higher Densities

When the pumping density increases, the dynamics changes drastically. Once $N_{k_{\parallel}}$ becomes non-negligible, the LP-LP scattering and the Bose statistics become important (65; 30). LP-LP scattering, which conserves the energy and momentum among the initial and final states of LPs, can transport a LP in the bottleneck region into the bottom of the branch in a single scattering event (while at the same time transporting a bottleneck LP to an exciton-like state at a higher energy). Hence it is a particularly efficient for overcoming the bottleneck effect. It increases quadratically with $N_{k_{\parallel}}$ and quickly becomes the dominant relaxation channel. At the same time, both LP-LP scattering and LP-phonon scattering are enhanced by the Bose final state stimulation effect (the scattering rate is enhanced from $\propto 1$ to $\propto (1 + N_{k_{\parallel}})$, where $N_{k_{\parallel}}$ is the final state population). Since the energy DOS of LPs decreases steeply with decreasing energy, the Bose final state stimulation leads to a much larger probability for scattering high energy LPs into low energy states than the reverse process.

These nonlinear effects at higher pumping densities accelerate LP energy relaxation, as demonstrated by the time evolution of the ground state LPs in figure 5.2, and by the disappearance of bottleneck in figure 5.3

5.2   The Experimental Strategy

The LP-LP scattering combined with the Bose final state stimulation give rise to very large nonlinearity in the microcavity system. To utilize this large nonlinearity and observe novel phenomena of polaritons, three strategies are generally adopted. The first strategy is to exploit directly the stimulated LP-LP scattering via a resonant parametric amplification scheme (65; 29). A coherent population of polaritons are built up in the signal and idler mode with the coherence inherited from the pump laser and seeded by the probe laser, analogous to the process of coherent four-wave mixing in nonlinear optics. It is a driven non-equilibrium transition with interesting potential applications for polariton-optics. The second strategy is to use a system with high exciton saturation density, so as to reach quantum degeneracy in the *bottleneck* states
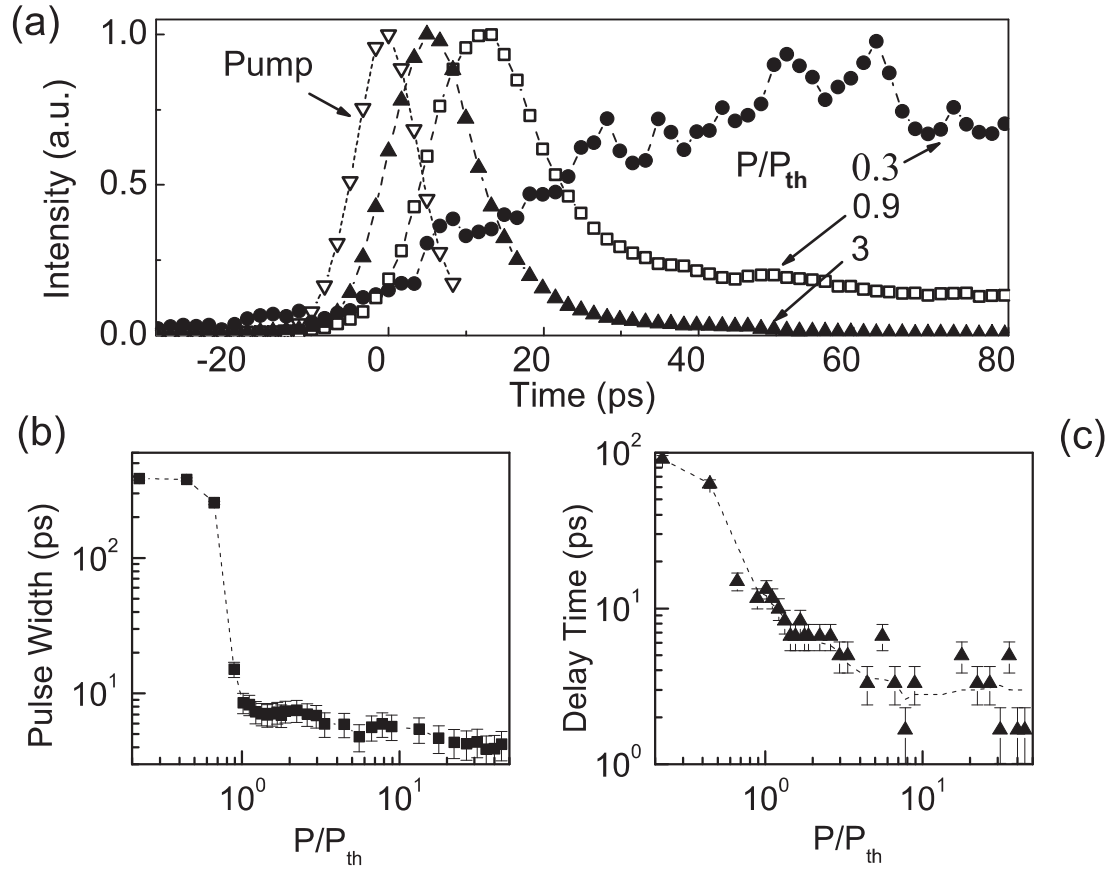
Figure 5.2: (a) The time evolution of the $k_{\parallel} = 0$ LP emission intensity. (b) Pulse FWHM ΔT_p vs. pump intensity P/P_{th}. (c) Turn-on delay time of the emission pulse vs. pump intensity P/P_{th}. From reference (3).

(30; 31). Excitations are created at energies well above a target mode, so that the pumped mode can not be scattered into the target mode with a single phase-coherent scattering event, instead, non-coherent energy relaxations are necessary to populate the target mode, such as multiple phonon emissions. Hence the pumping process can be described as the injection of incoherent hot excitons or even electron-hole plasma. LPs in the target mode acquire coherence only by stimulated scattering or spontaneous symmetry breaking at a phase transition threshold. The coherence is then carried into the light field when the photon component of the polaritons leaks out of the system. Degenerate population (Huang et al. (30)) and first-order coherence (Richard et al. (31)) were observed for a bottleneck polariton laser. However, the system is always far from equilibrium, there is a large degeneracy (in $|k_{\parallel}|$) in the
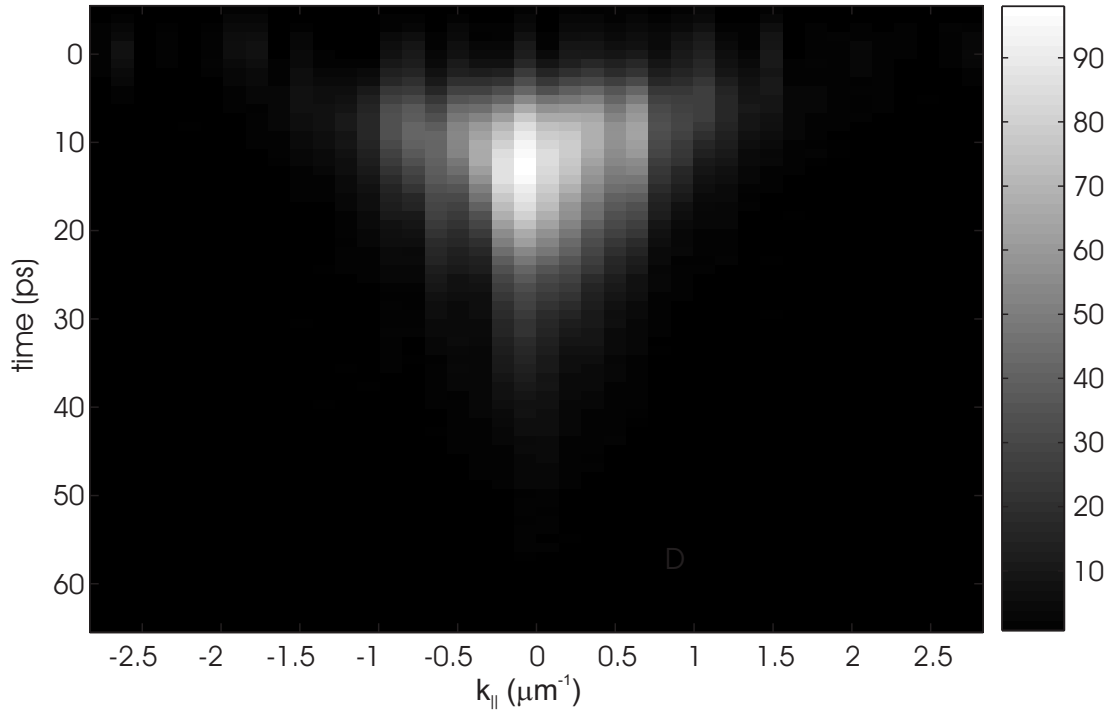
Figure 5.3: Evolution of LP population distribution $N_{LP}(k_\parallel)$ above the stimulated scattering threshold. Most LPs relax to and decay from the low energy LP states rather than from a bottleneck. Used S-GaAs-II, $\Delta = 6.7$ meV.

lasing modes at the bottleneck, and it is difficult to characterize the thermodynamic properties of the degenerate LP gas. The third strategy is similar to the second strategy, but the system is optimized such that quantum degeneracy is first reached in the the $k_\parallel = 0$ LP state (the LP ground state), thus thermal equilibrium of the quasi-particles may be established under proper experimental conditions and a closer comparison to BEC transition is possible. This thesis adopts the third strategy.

To ensure condensation in the LP ground state, we use a GaAs-based system which has relatively large scattering cross sections. To address the relatively low saturation density, 12 QWs are included in the structure. Multiple QWs on one hand reduced the exciton density per QW for a given total LP density, on the other hand increased the exciton-photon coupling to reach the *very strong coupling* regime (56), which leads to reduced exciton Bohr radius for the LP branch hence further increased exciton saturation density. The experimental scheme is depicted in figure 5.4. A laser pump resonantly excites hot LPs at $k_\parallel = 5 \sim 6\ \mu m^{-1}$, so as to minimize the
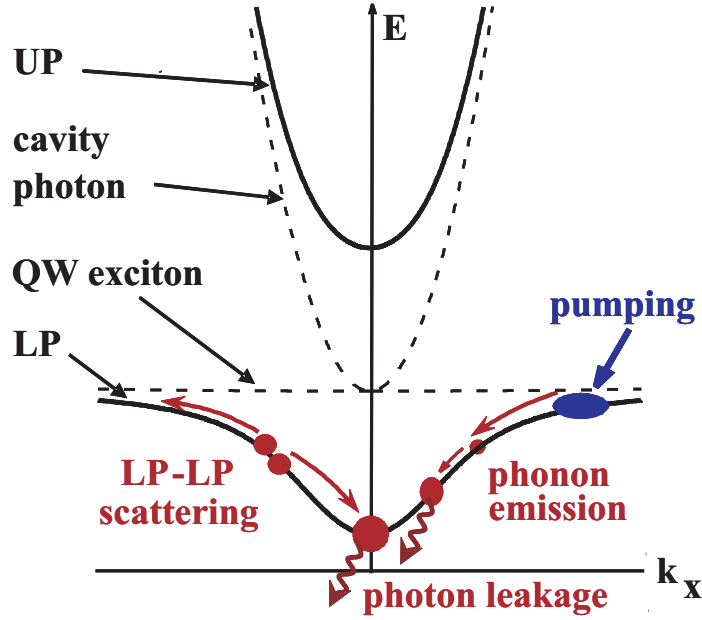
Figure 5.4: Schematics of the experimental principle for LP condensation.

excitation of free electrons and holes, which usually increase the exciton decoherence rate. The $k_\parallel = 5 \sim 6\ \mu\text{m}^{-1}$ is well above the inflection point of $k_\parallel \sim 2\mu\text{m}^{-1}$ so that the coherent LP amplification is avoided.

5.3   Quantum Degeneracy in the LP Ground State

In the experimental scheme described above, using S-GaAs-II, we measure the pump power dependence of the ground state LP emission and observe a sharp super-linear increase of the emission intensity with the pump rate (figure 5.5).

The emission intensity is proportional to the LP population $N_{LP}(k_\parallel)$ in the corresponding $k_\parallel$ mode and is estimated by taking into account the collection efficiency of the optical setup. $N_{LP}(0)$ is of the order unity at the threshold. This indicates that the nonlinear threshold in the input-output relation originates from the onset of the stimulated scattering of LPs into the $k_\parallel \sim 0$ LP state.

The threshold pump power density is $P_{\text{th}} \sim 300\text{W/cm}^2$. The corresponding injected carrier density per QW n_{QW} can be estimated using the following parameters:
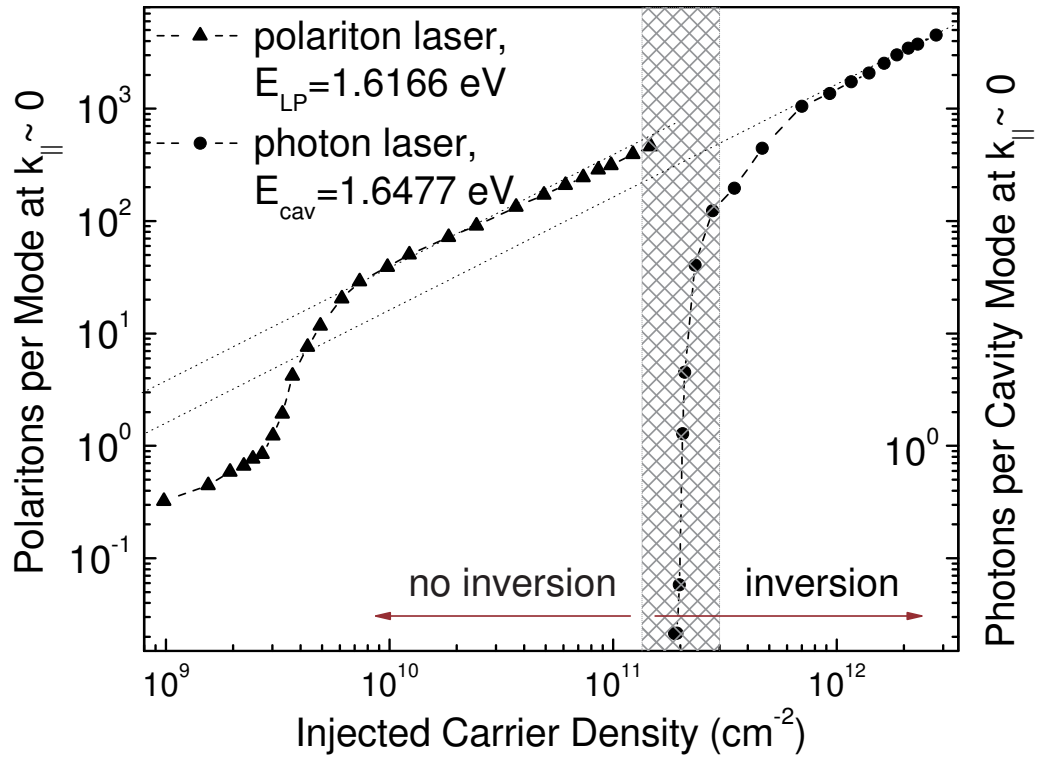
Figure 5.5: Number of LPs and cavity photons per mode vs. injected carrier density for a polariton condensate (triangles, the scheme in figure 5.4 and in the left panel of figure 5.8) and a photon laser (circles, the scheme in the right panel of figure 5.8), respectively. The gray-zone marks the population inversion densities from band edge to 15 meV above the band edge.

the number of pump photons per pulse is $\sim 5 \times 10^7$, the net absorption of the micro-cavity system is $\sim 0.12\%$ calculated by the transfer matrix method, and the number of QWs is N_{QW}=12. For a spot of $D \approx 15\mu m$ in diameter, $n_{QW} \approx 3 \times 10^9$ cm^{-2} per pulse per QW. It is a factor of thirty smaller than the saturation density and two orders of magnitude smaller than the Mott density (n$\sim 1/\pi a_B^2$) and the transparency condition of $\sim 10^{11}$ cm^{-2} electron-hole pairs per QW. The total LP population is $n_{LP} = 12 n_{QW} \sim 4 \times 10^{10}$ cm^{-2} per pulse.

5.3.1   Dispersion Characteristics

As a further confirmation that LPs are the normal modes of the nonlinear system, we measure its energy dispersion versus the transverse wavenumber $k_\parallel$ by angle re-solved PL measurement (section 4.3.1), with an angular resolution of 0.5°. It agrees very well with the LP dispersion curve calculated with the transfer matrix method (figure 5.6(a,b,c)). Below the polariton laser threshold, the energy of the LP photolu-minescence is shifted slightly below the calculated dispersion curve (figure 5.6(a)) due to the Stokes shift of QW excitons. The shift is more noticeable at larger emission angles where the LP inhomogeneous linewidth is wider due to an increasing fraction of the exciton component and larger TE-TM splitting of the cavity modes (66). The blue-shift of the whole dispersion curve with increasing pump rate reflects that the LP nonlinearities stem from the Coulomb interaction and Pauli exclusion principle of the constituent fermions. As seen in figure 5.6(b), blueshifted and non-shifted dis-persions coexist, which is mainly due to the non-uniform spatial distribution of the injected carriers. As will be discussed in section 6.2, the spatial distribution of the LPs changes abruptly at the threshold, leading to a high concentration of LPs in the center of the laser spot, surrounded by a broad distribution of LPs at a lower density. The blueshifted dispersion corresponds to the central region and the non-shifted dis-persion corresponds to the peripheral, non-lasing region. Well above the threshold, the non-shifted dispersion is no longer seen, because the intensity of the blueshifted LP emission dominates the light emission (Figure 5.6(c)). And the measured disper-sion follows unambiguously the calculated LP dispersion which takes into account the

blueshift of the excitons.
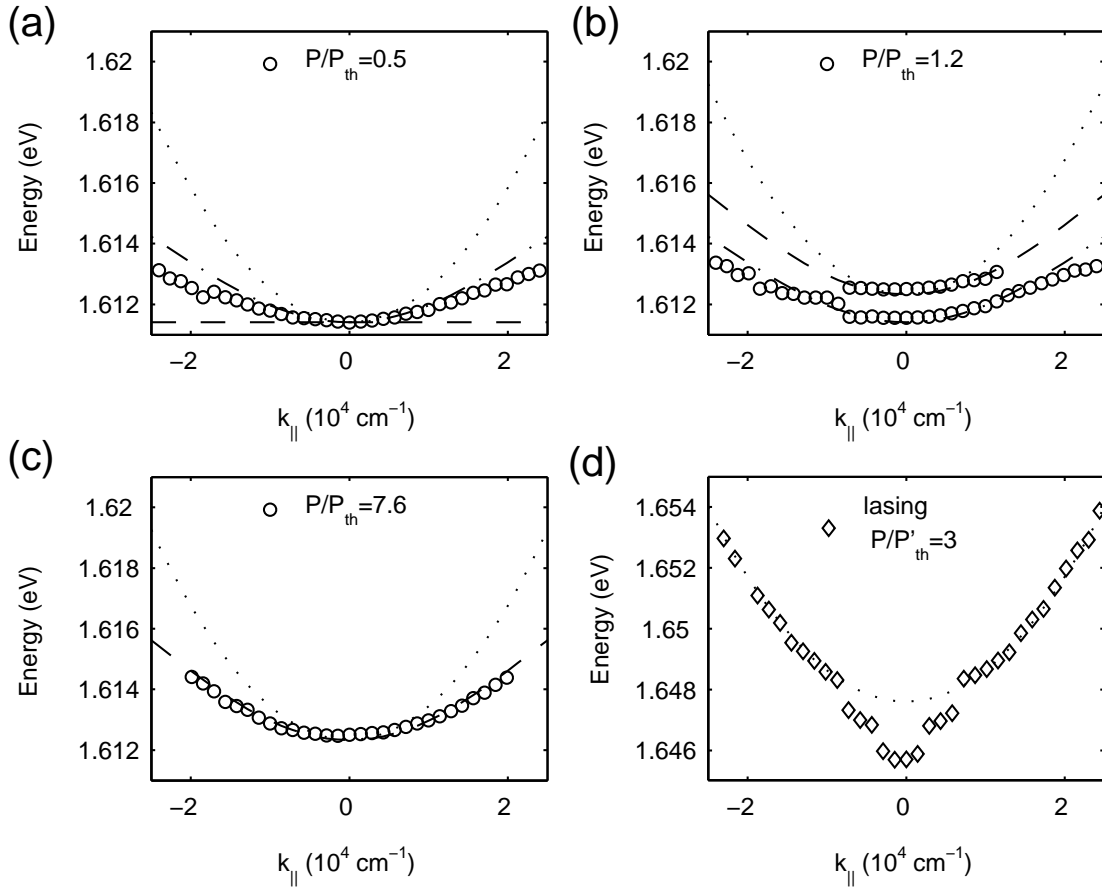
Figure 5.6: Comparison of the measured and calculated dispersion curves. (a),(b),(c) Measured LP dispersion curves (circles) and calculated cavity photon (dotted line), unshifted LP (dash-dot line), and blue shifted LP (dash line) dispersion curves in scheme I, P_{th}=300 W/cm². Origin of the cavity photon dispersion is artificially shifted for comparison. (d) Measured (diamonds) and calculated (dotted line) cavity photon dispersion curves, P'_{th}=2 KW/cm².

5.3.2 Polarization Dependence

In the above experiment, the pump is linearly polarized since this configuration renders the lowest threshold density, a factor of two smaller than that of a circularly polarized pump (figure. 5.7 (a) and (b)). A straightforward interpretation follows from the fact that the cavity resonances are different for TE and TM polarized light, thus a linearly polarized pump light is more efficiently absorbed than a circularly

polarized pump light.

Using a quarter-wave plate and a polarizer, we collected separately the left- and right-circularly polarized components of the emission, denoted as σ_1 and σ_2 hereafter. We define the degree of circular polarization $\eta = \frac{I_{\sigma_1} - I_{\sigma_2}}{I_{\sigma_1} + I_{\sigma_2}}$ to describe the difference between their intensities I_{σ_1} and I_{σ_2}. According to the selection rule, the pump light with polarizations σ_1 or σ_2 excite the spin-up or spin-down LPs. Below threshold, the thermalization time is longer than the spin relaxation time. Hence, equal populations of spin-up and spin-down LPs are formed at $k_\parallel = 0$, and thus random polarization was observed regardless of the polarization of the pump. With increasing pump rate, the thermalization process is accelerated. Under the pumping of left-circularly polarized light, the LP population corresponding to I_{σ_1} accumulates faster than that corresponding to I_{σ_2}, leading to an increase in η. As a result, stimulated LP-LP scattering and dynamic condensation occur first for co-polarized LPs, η escalating to larger than 0.9, as shown in Figure 5.5(a), while I_{σ_2} continues to grow linearly.

Under the pumping of linearly polarized light, the initial spin-up LP population corresponding to I_{σ_1} was barely larger than I_{σ_2}. Yet still I_{σ_1} rapidly overwhelms I_{σ_2} by spontaneous symmetry breaking when reaching the threshold P_{th}. At a pump density approximately three times P_{th}, the spin-down LP population corresponding to I_{σ_2} also reaches its threshold and increases nonlinearly. Resultantly, a fast increase of σ around P_{th} is followed by a sharp decrease around $3P_{th}$. The result indicates that spin flip relaxation between LPs is slow compared to the stimulated LP-LP scattering. Therefore, the two kinds of LPs independently relax, condense, and decay. A more complicated yet quantitative explanation may also be possible. For example, in a rate equation model by A. Kavokin $et.al.$ (58; 33), TE-EM splitting of LPs is taken into account, which causes coherent oscillation of circular polarizations, in addition to the dephasing of the polarization due to LP-phonon scattering. The model also predicts a lower threshold for linearly polarized pumping and gives numerical results qualitatively in agreement with the data shown in figure 5.7.
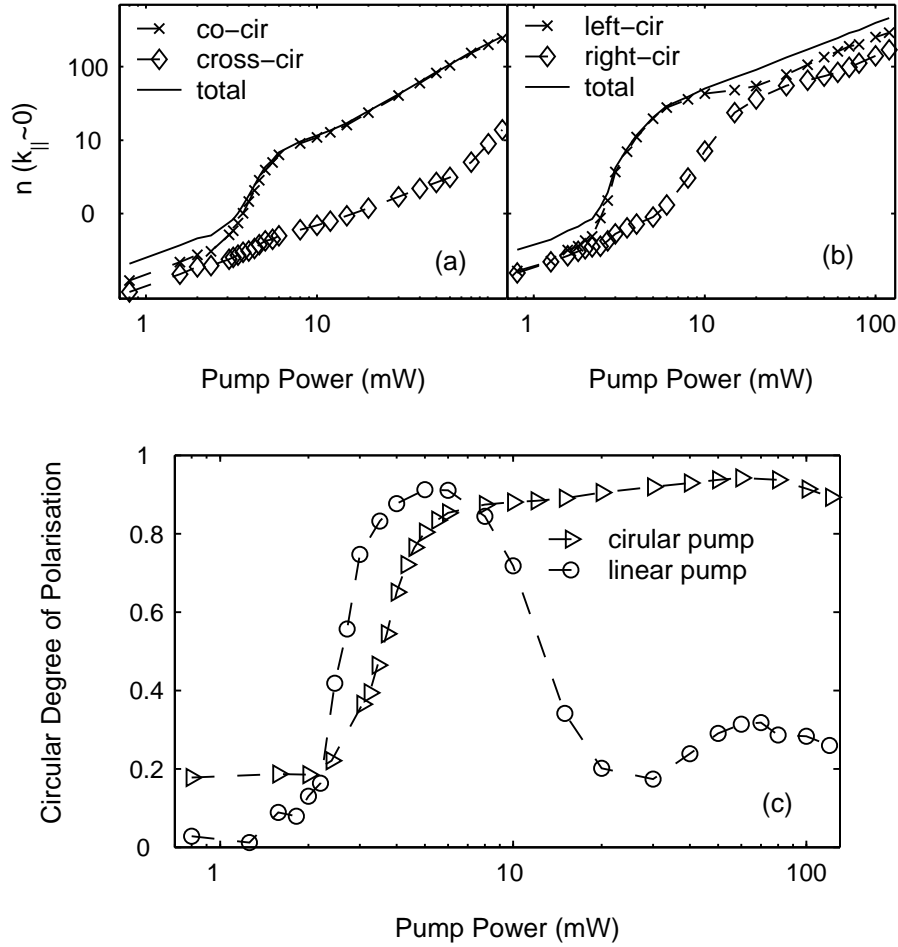
Figure 5.7: Polarization properties of LP emission. Emission intensity of LPs near $k_\parallel = 0$ vs. pump power under (a) circularly polarized pump, and (b) linearly polarized pump. The two circular-polarization components of the emission and the their total intensity are plotted. (c) depicts the circular degree of polarization vs. pump power with circularly polarized (triangles) and linearly polarized (circles) pumps.

5.4   Comparison with a Photon Laser

Since the sample's cavity layer thickness is tapered by growth, detuning of the cavity resonance relative to the exciton resonance changes across the sample. We can compare the LP quantum degeneracy threshold to a conventional photon laser threshold using the same sample and experimental setup. We focus the pump laser to a position on the sample, where the cavity mode is blue-detuned to 15 meV above the band edge. The pump energy was tuned accordingly to be resonant with the cavity mode energy at $k_\parallel = 5.33 \times 10^4$ cm^{-1}. Emission detected from the normal direction
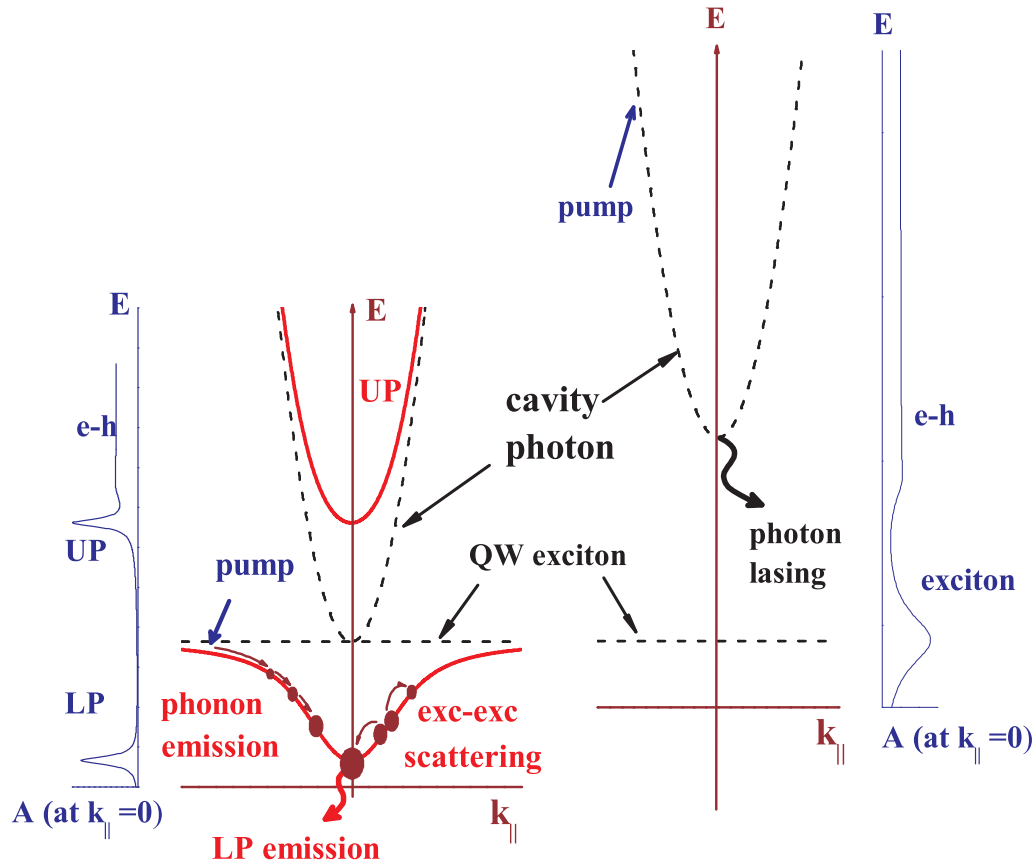
Figure 5.8: Schematics of the experimental principles for a photon laser (right panel) compared to LP condensation (left panel).

is at the cavity resonance, a photon lasing threshold is observed. The experimental scheme is depicted in the right panel of figure 5.8.

Photon Lasing Threshold

A threshold behavior is also observed in this case, and is compared to the LP condensation case in figure 5.5. Here the injected carrier density at threshold is about $n'_{QW} = 3 \times 10^{11}$ cm^{-2} per pulse per QW, which is approximately the density required for electronic population inversion at 15 meV above the band edge. This result is in agreement with the standard laser mechanism. That is, when the active volume of

the laser is large compared to its optical mode volume, the threshold of a semiconductor laser is solely determined by the electronic inversion condition (67). The cavity photon number per mode is estimated to be of the order of unity at threshold. This indicates that the nonlinear increase in the input-output relation originates from the onset of the stimulated emission of photons into the $k_{\parallel} = 0$ cavity photon mode.

Photon Laser Dispersion

The energy dispersion versus the transverse wavenumber is also measured for the photon laser, as shown in figure 5.6(d). The measured dispersion curve agrees very well with the bare cavity mode dispersion except for a redshift of the lasing modes at $k_{\parallel} \sim 0$ due to the mode-pulling effect in semiconductor lasers (68). The emission energies are mainly determined by the cavity resonance, while the electronic population inversion with a maximum gain at a lower energy pulls the lasing energy slightly toward the gain maximum.

The difference in the dispersion characteristics shown in figure. 5.6 (c) and (d) again confirms that the two nonlinear thresholds seen in figure. 5.5 correspond to a LP quantum degeneracy threshold and a photon lasing threshold, respectively.

5.5   Summary

In this chapter, we studied the energy relaxation of polaritons, we show that the polariton gas reaches a quantum degeneracy threshold at a density that LP-LP scattering and Bose final state stimulation are important.

We also compared the degenerate polariton gas to a conventional semiconductor laser. A photon laser results from the phenomenon of stimulated 'emission' of photons into photon modes with an occupation number larger than one. The quantum degeneracy threshold of polaritons is triggered by the same principle of bosonic final state stimulation, yet the physical process is different – it is stimulated 'scattering' of massive quasi-particles (the LPs) from non-lasing modes into the degenerate mode(s).

The nonlinear increase of the photon flux is a natural outcome of thermodynamic energy relaxation of the LPs. Hence the observed threshold of the polariton system requires no electronic population inversion. The threshold density is two orders of magnitude lower than that of a photon laser threshold. It serves as a proof-of-principle demonstration for polaritons as a new energy efficient source of coherent light.

Above the quantum degeneracy threshold, a macroscopic population of LPs spontaneously built up in the LP ground state, resembling Bose-Einstein condensation (BEC). To elucidate the physics of the degenerate polariton gas, we investigate its quantum statistical properties in the next chapter.

Chapter 6

Quantum Statistics of Condensed Polaritons

In Chap. 5, we show that stimulated scattering of LPs overcomes the bottleneck effect above a threshold pumping density, the population in the ground state increases nonlinearly with the pump and quickly builds up to be much larger than one, crossing the quantum degeneracy threshold. Quantum degeneracy is often associated with a transition to a macroscopic quantum state, such as a BEC state. To search for direct manifestation of such a phase transition, we study the quantum statistics of the polariton gas in this chapter.

6.1   Coherence Properties

In a condensate, thermal fluctuations are suppressed and the macroscopic population in the ground state can be described by a single-particle wavefunction. The distinction between a thermal mixture and a quantum mechanical pure state is best manifested in the second-order and higher-order coherence functions.

6.1.1   Definition of $g^{(2)}(0)$

The time-domain second order coherence function $g^{(2)}(\tau)$ is defined as:

$$g^{(2)}(\tau) = \frac{\langle \hat{E}^{(-)}(t)\hat{E}^{(-)}(t+\tau)\hat{E}^{(+)}(t+\tau)\hat{E}^{(+)}(t)\rangle}{\langle \hat{E}^{(-)}(t)\hat{E}^{(+)}(t)\rangle^2}, \tag{6.1}$$

where $\hat{E}^{(-)}(t)$ and $\hat{E}^{(+)}(t)$ are the negative and positive frequency parts of the electric field operator at time t, respectively (69). $g^{(2)}(\tau)$ measures how the state at t is correlation with the state at $t+\tau$. If $\hat{E}(t)$ and $\hat{E}(t+\tau)$ are uncorrelated,

$$g^{(2)}(\tau) = \frac{\langle \hat{E}^{(-)}(t)\hat{E}^{(+)}(t)\rangle\langle \hat{E}^{(-)}(t+\tau)\hat{E}^{(+)}(t+\tau)\rangle}{\langle \hat{E}^{(-)}(t)\hat{E}^{(+)}(t)\rangle^2} = 1.$$

If $\hat{E}(t)$ is multi-mode, the ensemble average in (6.1) again gives $g^{(2)}(\tau) = 1$. For a single mode state, $g^{(2)}(\tau) \equiv 1$ when $\tau \to \infty$, while the maximum correlation (or anti-correlation) is measured by $g^{(2)}(\tau = 0)$ which has the following property:

$$g^{(2)}(0) = 2, \qquad \text{thermal state}$$

$$g^{(2)}(0) = 1 - \frac{1}{n}, \qquad \text{number state}|n\rangle$$

$$g^{(2)}(0) = 1, \qquad \text{coherent state}$$

6.1.2 $g^{(2)}(0)$ of the LP Ground State

$g^{(2)}(\tau)$ is conventionally measured by a Hanbury Brown-Twiss setup discussed in section 4.3.4 (a sketch of the HB-T setup in figure 4.12 is reproduced in figure 6.1).

The pulsed LP emission centered at $E_{LP}(k = 0)$ was collected in the direction normal to the sample surface and filtered by a monochromator with a resolution of $\Delta\lambda$=0.1 nm, resulting in a pulse with a coherence time of $\Delta\tau_c = \sqrt{8\ln 2}\,\lambda^2/(c\,\Delta\lambda) \sim$ 4 ps. The filtered pulse is then sent to the HB-T setup. Since the polariton dynamics is much faster than the time resolution of the photon counters, we essentially measure the area under each peak of the recorded histogram, which gives the numerator in
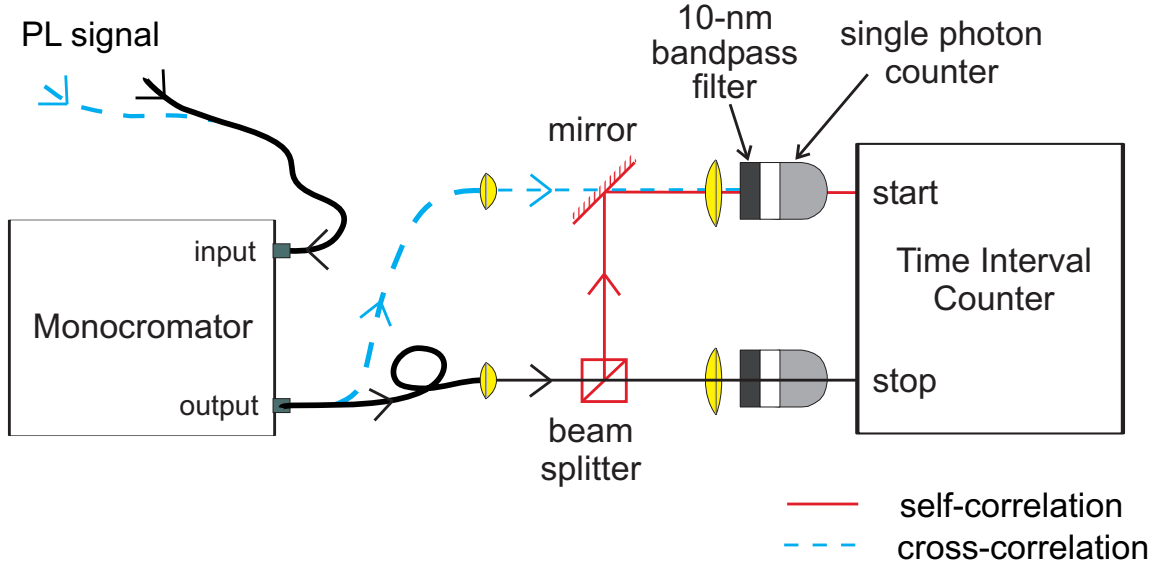
Figure 6.1: A realization Hanbury Brown-Twiss measurement with single photon counters. For auto-correlation measurement, use a single-core fiber, beam splitter and mirror (red solid path). For cross-correlation, use a double-core fiber bundle to carry the two input and output signals (blue dashed path).

the following equation:

$$\overline{g^{(2)}}(j) = \frac{\langle n_1(i)\, n_2(i+j)\rangle_i}{\langle n_1\rangle\langle n_2\rangle},$$ (6.2)

where $n_1(i)$ and $n_2(i+j)$ are the photon numbers detected by the two photon counters in pulses i and $i+j$ respectively. In the limit of low average count rates (< 0.01 per pulse in our experiment), $\overline{g^{(2)}}(j)$ approximates $g^{(2)}(\tau)$ time averaged over each pulse. For $j \neq 0$, coincidence counts are recorded from adjacent pulses which are uncorrelated and have $\overline{g^{(2)}}(j) \equiv 1$. Assuming same statistical properties of all pulses, the area of these peaks at $j \neq 0$ gives the denominator in equation (6.2).

Below threshold, the emission is expected to be in a thermal state, for which $g^{(2)}(0) = 2$ and $g^{(2)}(\tau \gg \Delta\tau_c) = 1$ (70). The FWHM temporal width of the pulse is about 350 ps below threshold (Figure 5.2), much longer than the coherence time of the pulse $\Delta\tau_c \sim 4$ ps. Since the measured $\overline{g^{(2)}}(0)$ is an integration of $g^{(2)}(0)$ over the whole pulse as given in equation (6.2), and $g^{(2)}(\tau) \approx 1$ during most of the pulse, $\overline{g^{(2)}}(0)$ is also close to 1. At threshold, the pulse width shortens to ~ 8 ps and becomes comparable to $\Delta\tau_c$. Hence $\overline{g^{(2)}}(0)$ becomes a good approximation of $g^{(2)}(0)$. Here, we observed bunching of the emitted photons, with a maximum $\overline{g^{(2)}}(0)$ of 1.77 at
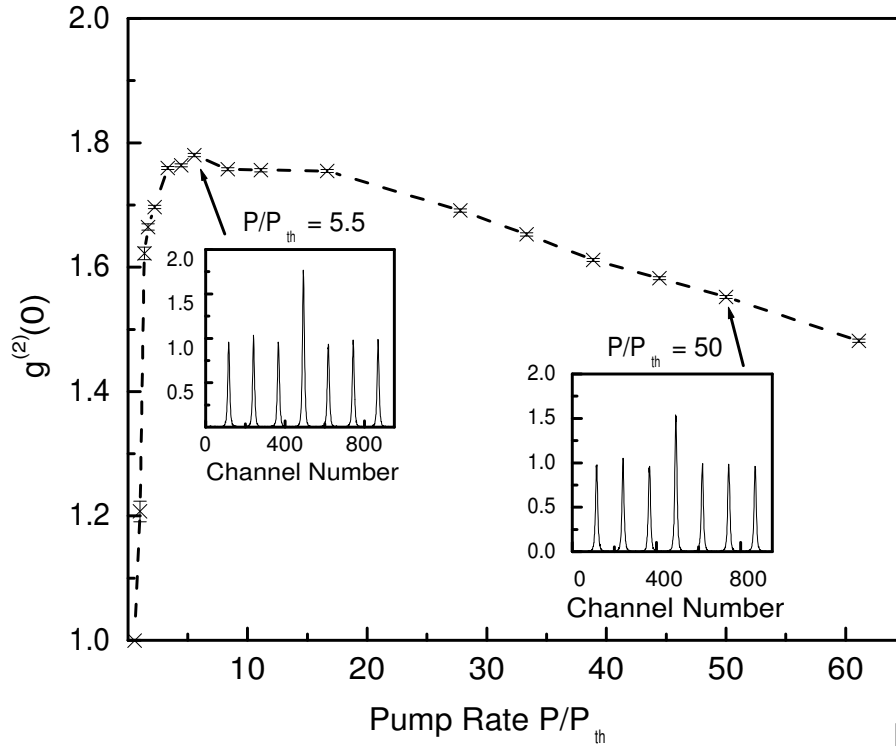
Figure 6.2: The second order coherence function $\overline{g^{(2)}}(0)$ vs. pump intensity P/P_{th}. From reference (3).

$P/P_{th} \sim 1.1$. This bunching effect, which is obscured by the time integration effect below threshold, is expected for a thermal state. Far above threshold, the pulse width only decreases further, therefore $\overline{g^{(2)}}(0)$ remains a good estimate for $g^{(2)}(0)$. However the $\overline{g^{(2)}}(0)$ measured in this region decreases, demonstrating the formation of second-order coherence in the system, or in other words, the polariton gas starts to acquire macroscopic coherence.

$\overline{g^{(2)}}(0)$ decreases only very slowly with increasing density above threshold, indicating a relatively small condensate fraction which builds up only very gradually with increasing total density of LPs. This is typical of two-dimension systems with relatively strong interactions, where there is large quantum depletion of the condensate. Due to the dynamical nature of the current experiments, the condensate fraction may also be evolving with time within the pulse.

6.2   Spatial Distributions

The presence of a condensate is expected to change the spatial distribution in characteristic ways. If there is a harmonic potential, the spatial distribution features a Thomas-Fermi profile, and the width of the distribution scales inversely proportional to the width in the momentum space. In the current microcavity without intentional in-plane confinement potential, the spatial properties are governed by two factors: a non-uniform spatial distribution due to the Gaussian profile of the excitation laser — characterized by a full-width half-maximum (FWHM) ω_p $\sim$20 μm, and the finite extension of the macroscopic coherence as a 2D system — characterized by the size ω_c of the condensate. Neglecting diffusion, LPs exist only within the excitation spot. A complete quasi-BEC means that macroscopic coherence extends to comparable to the excitation spot size. The excitation density is highest at the center of the spot, hence the central part reaches the degeneracy threshold first, and form a quasi-condensate with a spatial extension $\omega_c << \omega_p$. With increasing excitation density, the condensate grows to a larger size, also requiring a larger threshold density $n_c(\omega_c)$ (section 2.7).

To study this behavior, we measure the real space distribution of the LPs as shown in figure 6.3. A two-dimensional Gaussian profile of the LP population is observed below threshold with a FWHM spot size $\omega \approx 15$ μm. Due to the steep incidence-angle of the pump laser, the spot is slightly elliptical, i.e., wider along the pump incidence direction x and narrower along the orthogonal direction y (figure 6.3(a) and figure 6.4(a)). Close to threshold, a sharp peak emerges at the center of the spot, reducing the spot size to a minimum value: $\min(\omega) = 3$ μm at $P/P_{\text{th}} \sim 1$ (figure 6.3(b)).

Increasing the pump rate above threshold, the emission spot size increases gradually. A trivial explanation of the increase is that, with increasing pump rate, a larger and larger area has a local density above the stimulated scattering threshold. This interpretation is express by the following equation assuming a fixed threshold density:

$$\omega' = \omega_p \sqrt{1 - \log_2(1 + \frac{1}{p})}, \tag{6.3}$$
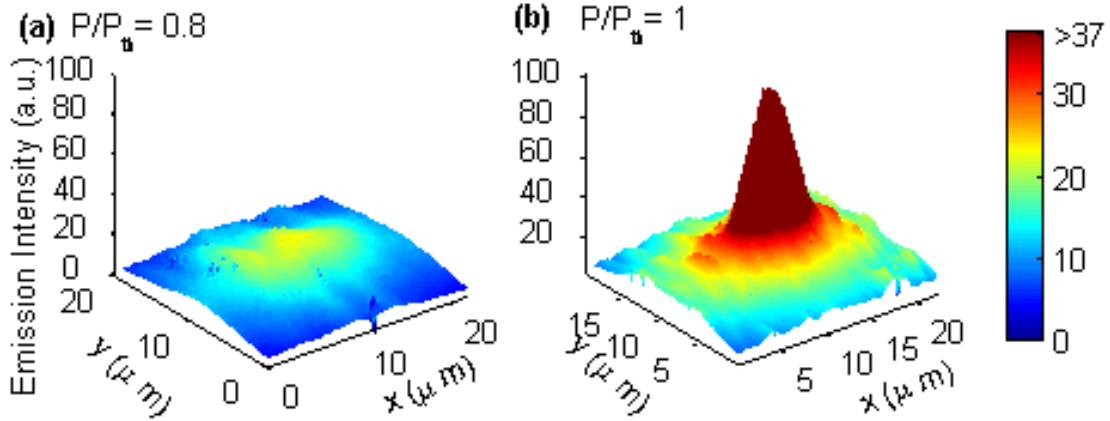
Figure 6.3: Spatial profiles of LPs at *(a)* $P/P_{\text{th}} = 0.8$ and *(b)* $P/P_{\text{th}} = 1$.

where $p = P/P_{th}$ is the pump rate normalized by threshold pump power P_{th}, ω_p is an effective pump spot size including the carrier diffusion. Using ω_p as a fitting parameter, the best least-square fitting of the data is shown in figure 6.4 (c), the deviation is obvious, the measured spot size increases much slower than predicted by equation (6.3).

Alternatively, we may assume that the observed spot size above threshold reflects the size of the condensate in which macroscopic coherence is established. In 2D, the critical density of BEC $n_c(\omega)$ depends on the size of the system ω. $n_c(\omega)$ increases with ω as given by equation 6.5, hence the region above threshold grows slower than modeled by (6.3). Taking into account this effect, (6.3) is modified as:

$$\omega(p) = \omega_p \sqrt{1 - \log_2(1 + \frac{1}{p} \frac{n_c(\omega(p))}{n_c(\omega_c)})}. \tag{6.4}$$

Here $\omega_c \doteq \omega(p = 1)$ is the FWHM of the condensate when it first appears, and corresponds to the smallest measured size. As a coarse estimate, we assume the system size is $L = 2\omega$, and use $n_c(\omega)$ for a boson gas with fixed mass $m = 2m_{cav}$,
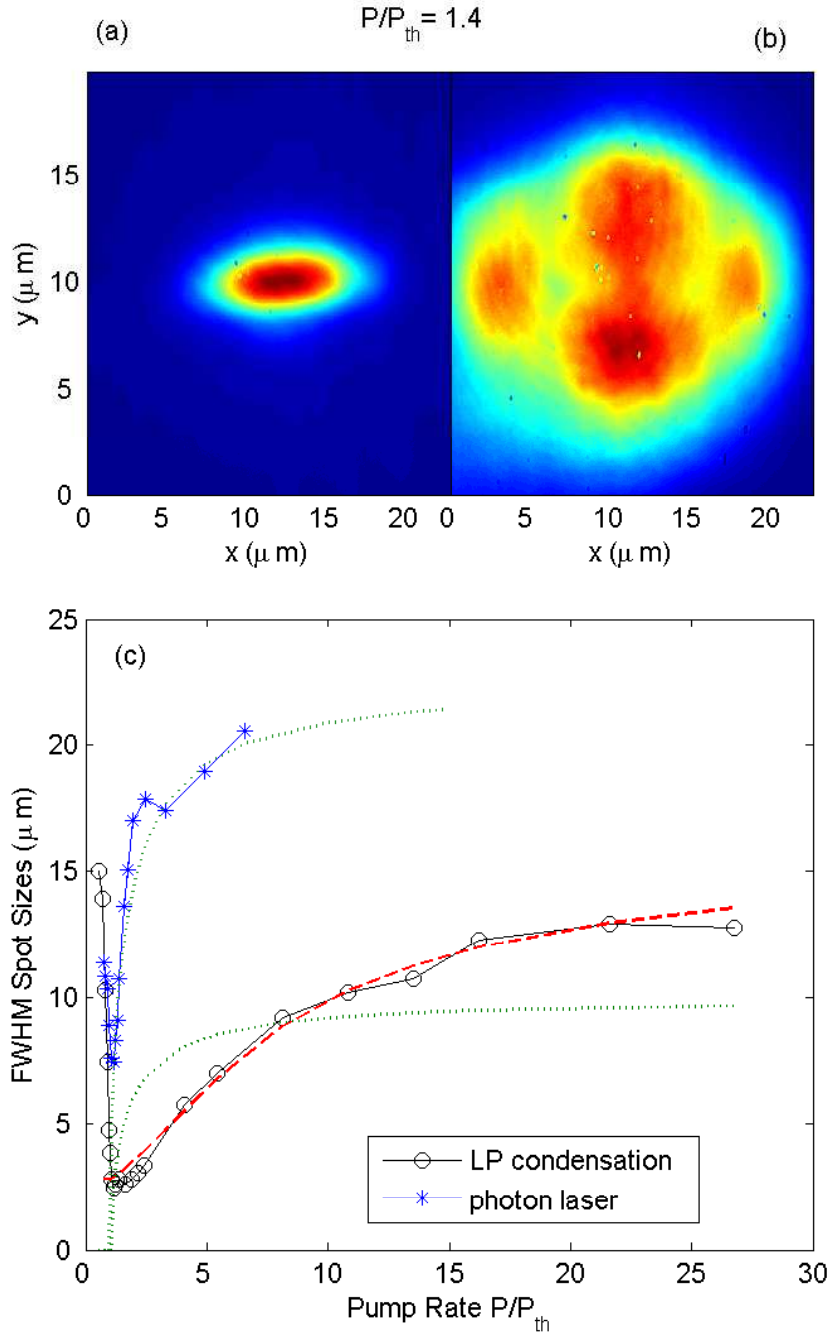
Figure 6.4: (a) and (b) depicts the spatial profiles of LPs and lasing cavity mode at 1.4 times the threshold pump powers, respectively. (c) compares the expansion of the spot-size vs. pump rate for the LP condensate (circles) and the photon laser (stars). The red dashed line is fitting by (6.4), with $\omega_p = 16.5\ \mu m$, $\omega_c = 2.8\ \mu m$. The green dotted lines are fitting by (6.3) assuming a pump spot size of $\omega_p = 9\ \mu m$ for the LP condensate and $\omega_p = 23\ \mu m$ for the photon laser.

then we have (see section 2.7, equation (2.42)):

$$n_c(\omega) = \frac{2}{\Lambda_t^2} \ln(\frac{L}{\Lambda_t}), \tag{6.5}$$

$$\Lambda_t = \frac{2\pi\hbar^2}{mk_BT}.$$

Λ_t is the LP de Broglie wavelength. Substitute (6.5) to (6.4), we obtain:

$$\omega = \omega_p \sqrt{1 - \log_2\left[1 + \frac{1}{p}\frac{\ln(2\omega/\Lambda_t)}{\ln(2\omega_c/\Lambda_t)}\right]}. \tag{6.6}$$

Using ω_p and ω_c as fitting parameters, we obtain fairly good agreement between data and the above equation (figure 6.4 (c)). It suggests that the slow increase of the observed spot size may be a signature of a coherent quasi-condensate of LPs.

Comparison to a Photon Laser

For comparison, we also measure the spatial profile of a photon laser (section 5.4, the right-panel scheme in figure 5.8).

A reduction in the spot size is also observed at the lasing threshold, with a minimum diameter of 7 μm. In sharp contrast to the polariton condensation, the increase of the spot size above threshold is much faster and is very well explained by the classical local oscillator model of equation (6.3) (figure 6.4 (c)). It confirms that when the system is operated as a conventional photon laser, gain is determined by local density of the electron-hole pairs with a threshold density independent of the system size.

Moreover, there are multiple transverse modes in the spatial profile above threshold (Figure 6.4(b)), as is typical in large-area vertical cavity surface emitting lasers. Coherence in this case is present only in the photon field but not in the electronic media. In the case of polariton condensation, however, a uniform Gaussian profile is maintained up to very high pump rates, without obvious multiple transverse modes (Figure 6.4(a)), which again indicates coherence among the polaritons above the condensation threshold.

6.3   Momentum Distribution

Another direct and important measure of the quantum statistics of a system is its distribution function in momentum space. As discussed in section 3.5, microcavity system has the unique advantage that LP's momentum distribution can be directly measured via angle-resolved PL measurement.

6.3.1   Time Integrated Momentum Distribution

We first measure the time integrated momentum distribution of LPs at zero detuning. We make two observations of the time evolution of the ground state LP population in section 5.1 (figure 5.2). Firstly, the energy relaxation time of the LPs is longer than or comparable to the ground state LP lifetime, thus the LP distribution does not change significantly within LP's lifetime. Secondly, the duration of the emission pulse of the ground state LPs is comparable to its lifetime. Hence the instantaneous distribution function of the LPs, when at the peak density of the ground state LP, may be estimated by a time integrated measurement.

We convert the time-integrated intensity of the angle-resolved LP emission into the number density of LPs by taking into account the $k_\parallel$-dependent density of states and the radiative lifetime of the LPs. In Figure 6.5(a), the LP number density vs. in-plane wavenumber $k_\parallel$ is compared with the classical Maxwell-Boltzmann (MB) distribution, $N(E) \propto \exp(-\frac{E_{\mathrm{LP}}(k_\parallel)}{k_B T_{\mathrm{LP}}})$, and the quantum mechanical Bose-Einstein (BE) distribution, $N(E) \propto 1/[\exp(\frac{E_{\mathrm{LP}}(k_\parallel)-\mu}{k_B T_{\mathrm{LP}}}) - 1]$, where k_B is the Boltzmann constant, and the LP ground state energy is used as the energy zero reference: $E_{\mathrm{LP}}(k_\parallel = 0) = 0$. Fitting parameters are the effective polariton temperature T_{LP}, the chemical potential μ, and an overall scaling factor. The dimensionless chemical potential is defined as $\alpha = -\mu/k_B T_{\mathrm{LP}}$. A lowest $k_\parallel = \Delta k \equiv 0.2 \times 10^4$ cm^{-1} is used, corresponding to a quantization area of $L^2 = (15~\mu m)^2$, which is approximately the pump spot size. Δk also corresponds to an experimental angular resolution of about $0.3°$.

Below threshold, neither distribution fits the data well, probably because most of the polaritons decay radiatively before the system can reach thermal equilibrium
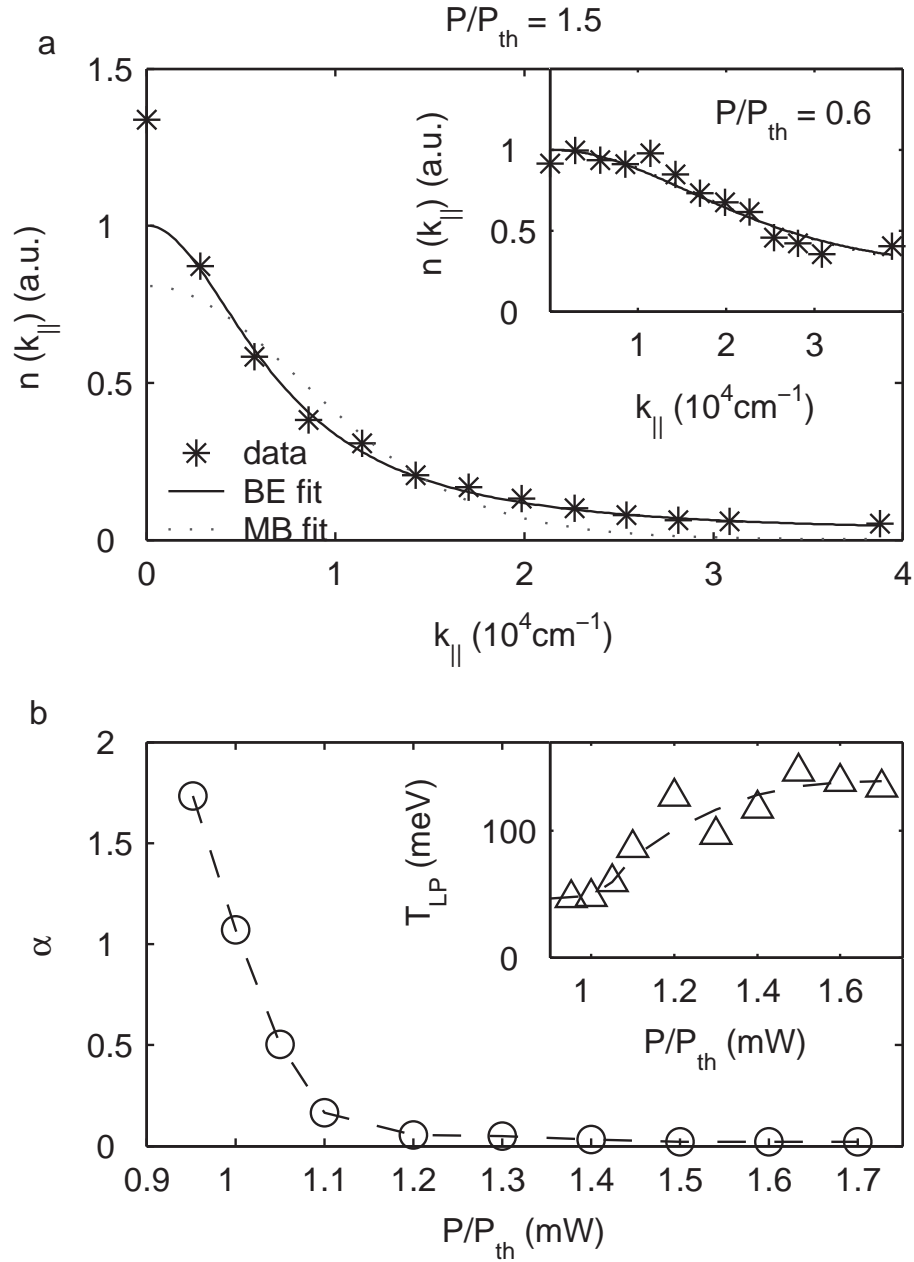
Figure 6.5: Momentum space distribution of LPs. (a) The measured LP population per state vs. $k_\parallel$ (stars), compared with BE (solid line) and MB (dotted line) distribution functions at pump rates $P/P_{th} = 1.5$ and $P/P_{th} = 0.6$ (inset). At $P/P_{th} = 0.6$, the fitted BE and MB distribution curves almost overlap. (b) The dimensionless chemical potential α vs. pump rate P/P_{th}, and the fitted effective LP temperature T_{LP} vs. pump rate (inset). The dashed lines are a guide for the eye. From reference (4).

(inset of figure 6.5(a)). Close to threshold, the BE distribution fits the data reasonably well, with a fitted T_{LP} ∼50 K, $\mu \sim -4.4$ meV, and thus $\alpha \sim 1$. This marks the transition to a quantum degenerate gas. Also there is an extra peak above the thermal BE distribution appearing at $k_{\parallel} \sim 0$. This implies that LPs start to accumulate in states with small $k_{\parallel}$, and hence the dynamic condensation of LPs is accelerated.

Above threshold, surprisingly good agreement with a BE distribution is obtained, except for the extra population in the condensed $k_{\parallel} \sim 0$ state (Figure 6.5(a)). α decrease rapidly near the threshold and reaches a minimum of α ∼0.02 at P/P_{th}=1.7 (figure 6.5(b)). This demonstrates that the LPs form a degenerate Bose gas, and establish quasi-equilibrium among themselves via the very efficient stimulated LP-LP scattering.

The fitted LP effective temperature T_{LP} is higher than the lattice temperature of 4 K, and it increases with increasing pump rate (inset of figure 6.5(b)). This implies that the LP-phonon scattering does not provide sufficient cooling to the injected hot excitons, and thermal equilibrium with the phonon bath is not reached. The high effective temperature of the LPs also suggests that the polariton condensate may survive at lattice temperatures higher than 4 K. Note that when $\alpha < 1$, the fitting of T_{LP} bears a much larger error compared to μ, because the total population is also a fitting parameter and the shape of the curve becomes rather insensitive to the temperature.

Far above threshold, the LP-LP interaction becomes strong. Therefore the condensate begins to be depleted. At the same time, the dynamics becomes faster and the time integrated data is no longer a good approximation of the instantaneous distribution.

6.4 From Quasi LP-Equilibrium to Thermal Equilibrium with Lattice

6.4.1 Time Constants of the Dynamical Processes

Whether or not LPs can be sufficiently cooled to reach thermal equilibrium with the phonon bath requires further investigation of the dynamical processes of the system.

As discussed in section 5.1, there are mainly three dynamical processes of the LP system:

1. LP decay via the out-coupling of its photon component,

2. LP-LP scattering,

3. LP-phonon scattering.

LP decay is characterized by the decay time $\tau_{LP} = \tau_{cav}/C_{k_\parallel}$, where $C_{k_\parallel}$ is the photon fraction of the LP defined in (3.54). The cavity lifetime is $\tau_{cav} = 1 \sim 10$ ps. For a given cavity, τ_{LP} increases with decreasing photon fraction. τ_{LP} is the shortest timescale for most microcavities at low pumping densities, leaving the system is in non-equilibrium, sometimes with a pronounced bottleneck.

LP-LP scattering is a nonlinear process, its timescale τ_{LP-LP} shortens with increasing LP density. When τ_{LP-LP} becomes shorter than τ_{LP}, LPs overcome the energy relaxation bottleneck and reach quantum degeneracy threshold. Due to the very efficient LP-LP scattering among states below the bottleneck, these LPs thermalize among themselves before they decay, and form degenerate BE distribution as observed in the previous section. However, LP-LP scattering conserves the total energy and momentum of the LPs, hence does not reduce the temperature of the LP gas. And a $T_{LP} \gg T_{lat}$ is observed.

The only mechanism to cool the LPs is the LP-phonon scattering. The linear LP-phonon scattering is a rather slow energy relaxation process at low densities with a more or less fixed timescale $\tau_{phonon} = 10 \sim 50$ ps. Fortunately, when $n_{k_\parallel \sim 0} > 1$ in a degenerate gas, LP-phonon scattering can be significantly enhanced by the Bose final

Polariton decay vs. Two relaxation processes

LP decay	LP-LP scattering	LP-phonon scattering

LP decay by leakage of photon component at $1/\tau_{LP}$	establishes equilibrium within LPs at $1/\tau_{LP-LP}$	establishes equilibrium with the lattice at $1/\tau_{lattice}$

Non-equilibrium	Quasi-equilibrium among LPs	Thermal equilibrium with host lattice
$\tau_0 < \tau_{LP-LP} < \tau_{lattice}$	$\tau_{LP-LP} < \tau_0 < \tau_{lattice}$	$\tau_{LP-LP} < \tau_{lattice} < \tau_0$
T_{LP} not defined	$T_{LP} > T_{lattice}$	$T_{LP} = T_{lattice}$
	⇩	
(bottleneck)	quasi-condensation	thermal equilibrium condensation

Figure 6.6: Time Constants and Equilibrium Conditions

state stimulation effect. If τ_{phonon} shortens to less than τ_{LP}, LPs may have enough time to reach thermal equilibrium with the phonon bath within their lifetime.

Chart 6.6 summarizes the crossover from a non-equilibrium regime to a thermal equilibrium regime, depending on the timescales of the different dynamic process of the system.

To go from a quasi-LP equilibrium to a thermal-equilibrium with the lattice, we need faster LP-phonon scattering and slower LP decay. For this purpose, there exists a simple and useful controlling parameter for the microcavity system: the detuning $\Delta = E_{cav} - E_{exc}$. At positive Δ, the excitonic fraction $X_{k_{\parallel}}$ increases, the LP effective mass is heavier and the energy density of states $\rho(E) \propto (1-|X_{k_{\parallel}}|^2)^{-1}$ increases. Hence LP-phonon scattering rates to low energy states ($\propto X_{k_{\parallel},i} X_{k_{\parallel} \sim 0} \, \rho(E_i)$) as well as LP-LP scattering rates to low energy states ($\propto X_{k_{\parallel},i_1} X_{k_{\parallel},i_2} X_{k_{\parallel},f_1} X_{k_{\parallel} \sim 0} \, \rho(E_{i_1})\rho(E_{i_2})\rho(E_{f_1})$) become larger. The flatter dispersion also requires less phonon scattering events to thermalize the LPs below bottleneck. At the same time, the LP lifetime $\tau_{LP} \approx$

$\tau_{cav}/(1 - |X_{k_\parallel}|^2)$ becomes longer. All these are favorable for LPs to reach thermal equilibrium.

The compromise is a higher critical density, stronger exciton localization, and shorter dephasing time of the LPs. At very large positive detunings, these detrimental effects prevent clear observations polariton condensation.

Hence the pre-requisite for thermal equilibrium LP condensation is that: LPs can reach quantum degeneracy threshold in a certain range of $\Delta > 0$, and the corresponding LP energy relaxation time $\tau_{relax}(\Delta)$ is shorter than $\tau_{LP}(\Delta)$. If both conditions can be satisfied, we confirm the establishment of thermal equilibrium by time-resolved momentum distribution, and compare the effective LP temperature T_{LP} with T_{lat}.

S-GaAs-II is used for this experiment, pump is linearly polarized and focused to a 50 μm-diameter spot on the sample. The emitted light is collected with an angular resolution of $0.5°$ in air by an optical fiber and sent to a spectrometer with an energy resolution of < 0.1 meV, or a streak camera with a time resolution of ~ 4 ps. The instantaneous LP number density $N_{LP}(k_\parallel, t)$ is converted from the count rate $N_c(\theta(k_\parallel), t)$ according to: $N_c(\theta(k_\parallel), t) = \eta f_p N_{LP}(k_\parallel, t) M(\theta(k_\parallel))/\tau_{LP}(k_\parallel)$, where $\theta(k_\parallel)$ is the far field emission angle of LPs. $\tau_{LP}(k_\parallel)$ is the radiative lifetime of the LPs. $M(\theta(k_\parallel))$ is the number of transverse states at $k_\parallel$ subtended by the acceptance angle of the detector $\Delta\theta \approx 0.01$. $f_p = 78$ MHz is the repetition rate of the pumping laser.

6.4.2 Quantum Degeneracy Threshold at $\Delta > 0$

We first study the detuning dependence of the quantum degeneracy threshold. As shown in figure 6.7, while the lowest threshold density is at $\Delta \approx 0$, a clear threshold exists for all $\Delta > 0$ up to $\Delta \sim 10$ meV. The mean-field blueshift of the LP energy at $k_\parallel = 0$ is less than 1 meV in these measurement, dispersions are also measured below and above threshold to confirm that the system is in the strong coupling regime. At large positive detunings $\Delta > 10$ meV , the blueshift of $E_{LP}(k_\parallel = 0)$ is relatively large, the LP dispersion becomes less distinct from a flat exciton dispersion, and it is difficult to distinguish LP condensation from lasing of localized excitons. Hence
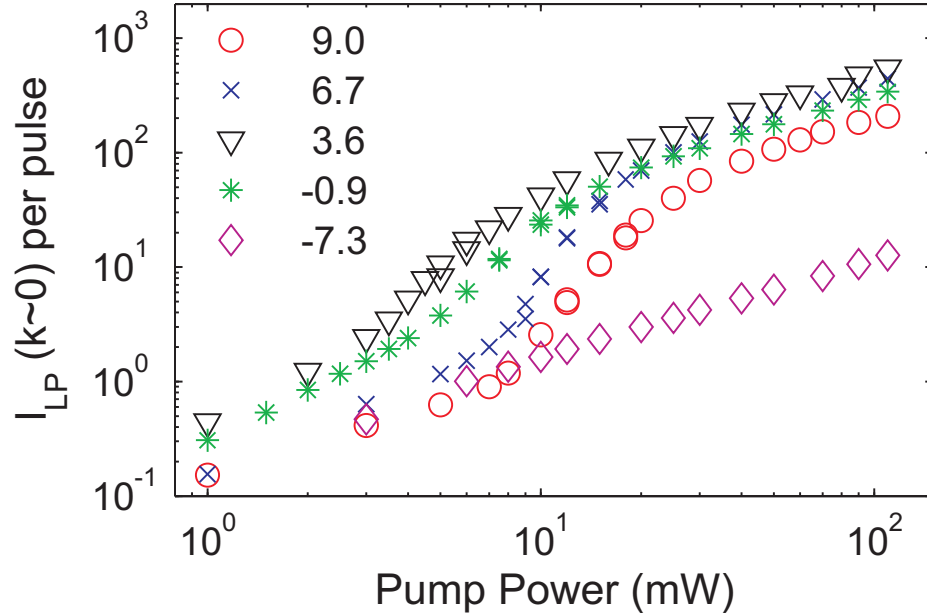
Figure 6.7: LP number per pulse $I_{LP}(k_\parallel \approx 0)$ vs. pump power at different detunings. No threshold is observed for $\Delta = -7.3$ meV.

we focus on $\Delta < 10$ meV. At negative detunings, quantum degeneracy is reached at bottleneck region first, and a clear threshold is absent in the LP ground state, the system stays in a highly non-equilibrium state.

6.4.3 τ_{relax} vs. τ_{LP}

Next we study the LP energy relaxation time τ_{relax} vs. the LP lifetime τ_{LP} for the LP ground state by time resolved measurement. Figure. 6.8 (a) shows the time evolution of $N_{LP}(k = 0)$. To estimate τ_{relax}, we model the system with two coupled modes, the $k_{k_\parallel} \approx 0$ LP ground state and a hot LP reservoir state. The dynamics is then described by the following two coupled rate equations:

$$
\begin{aligned}
\frac{\partial N_R}{\partial t} &= P(t) - \frac{N_R}{\tau_R} - \frac{N_R}{\tau_{relax}} \\
\frac{\partial N_0}{\partial t} &= -\frac{N_0}{\tau_0} + \frac{N_R}{\tau_{relax}}.
\end{aligned}
\tag{6.7}
$$

Here N_R and N_0 are the hot LP reservoir and LP ground state populations, respectively. $P(t)$ is an external pump represented by a Gaussian pulse, centered at $t = 0$
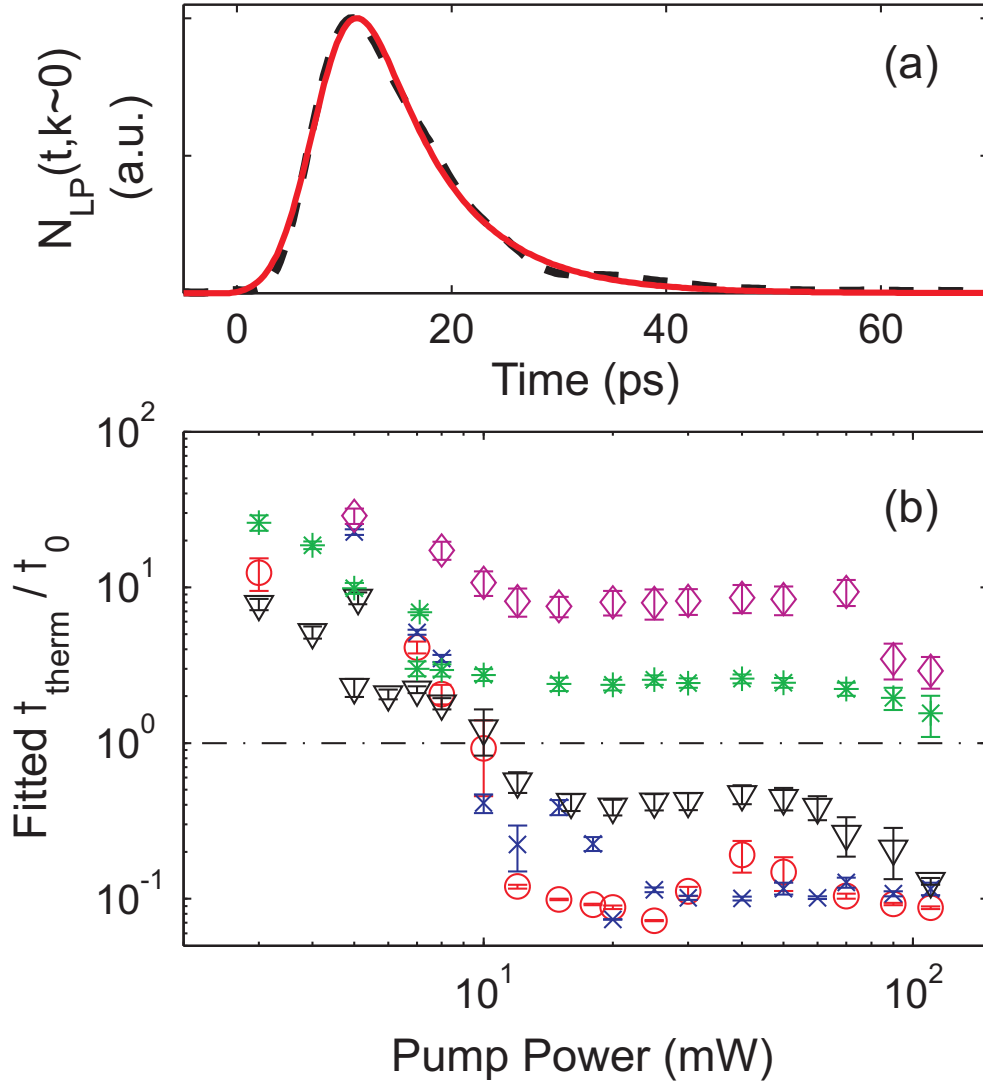
Figure 6.8: (a) Time evolution of ground state LP emission intensity $N_{LP}(k_\parallel \approx 0)$. The dashed line is data taken for $\Delta = 6.7$ meV, $P = 20$ mW, deconvolved with the streak camera resolution of 4 ps. The solid line is a fit to Eq. (6.7). (b) Normalized thermalization time τ_{relax}/τ_0 vs. pump power at different detunings. Below the dash-dotted line, τ_{relax} becomes shorter than τ_0, so thermal equilibrium is expected. Detunings in meV are given in the figure legend.

with a pulse width of 3 ps. τ_{relax} is the thermalization time from the reservoir to the ground state. τ_R and τ_0 are the lifetime of the LPs in the reservoir and the ground state, respectively. τ_0 can be determined from the cavity lifetime of $\tau_{cav} = 1.5$ ps and the detuning-dependent photon fraction C_Δ of the LP ground state: $\tau_0 = \tau_{cav}/|C_\Delta|^2$. We use the normalized $N_0(t)$ to fit the experimental curve. τ_R is much longer than τ_0 and τ_{relax}, we found it to have little influence on the fitting, so we set τ_R to infinity. τ_{relax} is the single fitting parameter. Despite the simplicity of the model, good agreement between data and the fitting curve is obtained as shown in figure. 6.8 (b).

In figure. 6.8 (b), we plot the normalized LP relaxation time τ_{relax}/τ_0. For all detunings there is a steep decrease of τ_{relax} near the quantum degeneracy threshold, reflecting the onset of stimulated scattering into the LP ground state. At a positive detuning of $\Delta = 6.7$ meV, τ_{relax} shortens from more than $20\tau_0$ below threshold to around τ_0 near threshold, and saturates at about $0.1\tau_0$ well above threshold. We expect that thermal equilibrium with the phonon bath may therefore be established above threshold with a quantum degenerate LP population in the ground state. For negative detunings, τ_{relax}/τ_0 saturates above unity and the system is expected to stay in non-equilibrium.

6.4.4   Time-Resolved Momentum Distribution

Finally to study if thermal equilibrium is formed when $\tau_{relax} < \tau_{LP}$, we measure the time-resolved momentum distribution of LPs. Figure 6.9 are contour plots of the time evolution of $N(k,t)$. At a positive detuning of $\Delta = 6.7$ meV (figure 6.9 (a)), LPs quickly concentrate to lower $k_\parallel$ states and mostly decay from there, as show by the bright emission at $k_\parallel \sim 0$ and the absence of a detectable bottleneck at all times. Peaked at $k_\parallel \sim 0$, the distribution is smooth at all times in the range of $k_\parallel$ we measured, showing that energy relaxation is fast compared to LP decay. In contrast, at a negative detuning of $\Delta = -4.3$ meV (Figure 6.9 (a)), strong bottlenecks are present at early times after the pump pulse. Though the population is gradually transported to lower $k_\parallel$ states, homogeneous k-distribution is hardly ever formed. This is because of the slow energy relaxation by inefficient LP-LP and LP-phonon

scattering. Particularly interesting is the case of a small $|\Delta|$. As show in figure 6.10, bottlenecks exist at an early time soon after the arrival of the pump, when there is not enough LP population in states with smaller $k_\parallel$ to trigger stimulated scattering. After about 10 ps, most of the injected population are still in the system and some population are accumulated in states with small $k_\parallel$, bottleneck disappear due to enhance LP-LP scattering into the $k_\parallel \sim 0$ states. At a still later time, most LPs decay out of the system and the stimulated scattering diminishes, since the $k_\parallel \sim 0$ LPs have a shorter lifetime than LPs at larger $k_\parallel$, bottleneck appears again.

Next we compare the instantaneous momentum distribution with BE and MB distributions. The collection efficiency η for this experiment is calibrated by replacing the sample with a fiber tip. Hence T_{LP} and $N_{LP}(0,t)$ are the only two fitting parameters:

$$
\begin{aligned}
N_{MB}(k_\parallel) &= N_0 \exp(-\frac{E_{\mathrm{LP}}(k_\parallel)}{k_B T_{\mathrm{LP}}}), \\
N_{BE}(k_\parallel) &= 1/[\exp(\frac{E_{\mathrm{LP}}(k_\parallel)}{k_B T_{\mathrm{LP}}})(1 + N_0^{-1}) - 1].
\end{aligned}
\tag{6.8}
$$

The normalized chemical potential α is defined as:

$$
\alpha = -\mu/k_B T_{\mathrm{LP}} = \ln(1 + N_0^{-1}).
\tag{6.9}
$$

At positive detunings $\Delta > 1$ meV, no bottleneck is observed at any pump level. Above threshold, about 30 ps after the pump pulse, the experimental data are very well described by a BE distribution, but not at all by a MB distribution, as shown in figure 6.11 (a). From BE distribution fitting, we obtain a T_{LP} close to the lattice temperature T_{lat}, and a normalized chemical potential $\alpha = 0.01 - 0.5$. Note that quantum degeneracy threshold $N_0 = 1$ is reached at $\alpha = \ln 2 \approx 0.7$. The results indicate that LPs are well thermalized with the phonon bath, forming a quantum degenerate Bose-Einstein distribution at the lattice temperature. This is consistent with the observation that $\tau_{relax} \ll \tau_0$ at these positive detunings above threshold.

At small detunings $|\Delta| < 1$ meV, although a bottleneck exists at most pump levels,
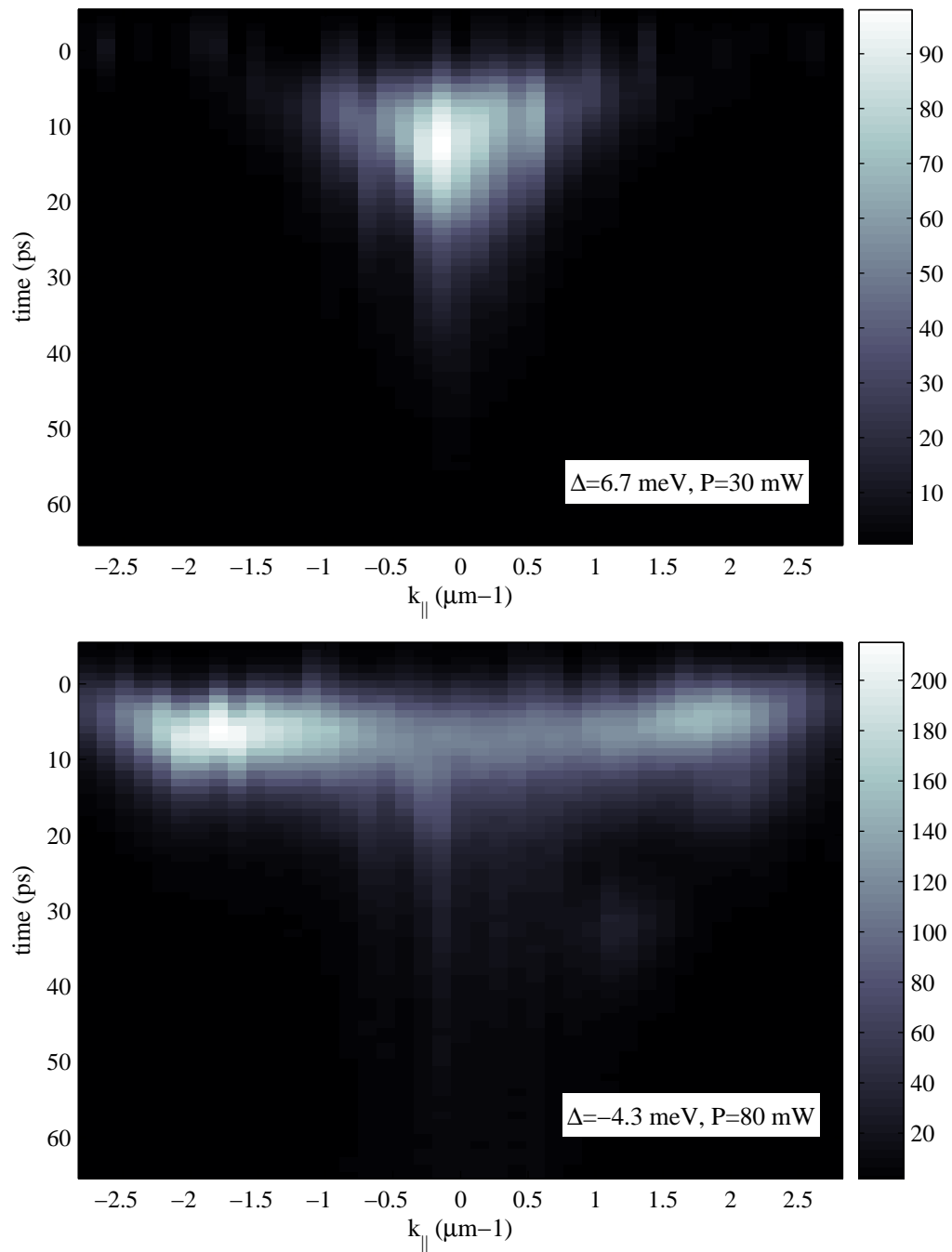
Figure 6.9: $N(k_\parallel, t)$ at (a) $\Delta = 6.7$ meV, P=30 meV; (b) $\Delta = -4.3$ meV, P=80 meV
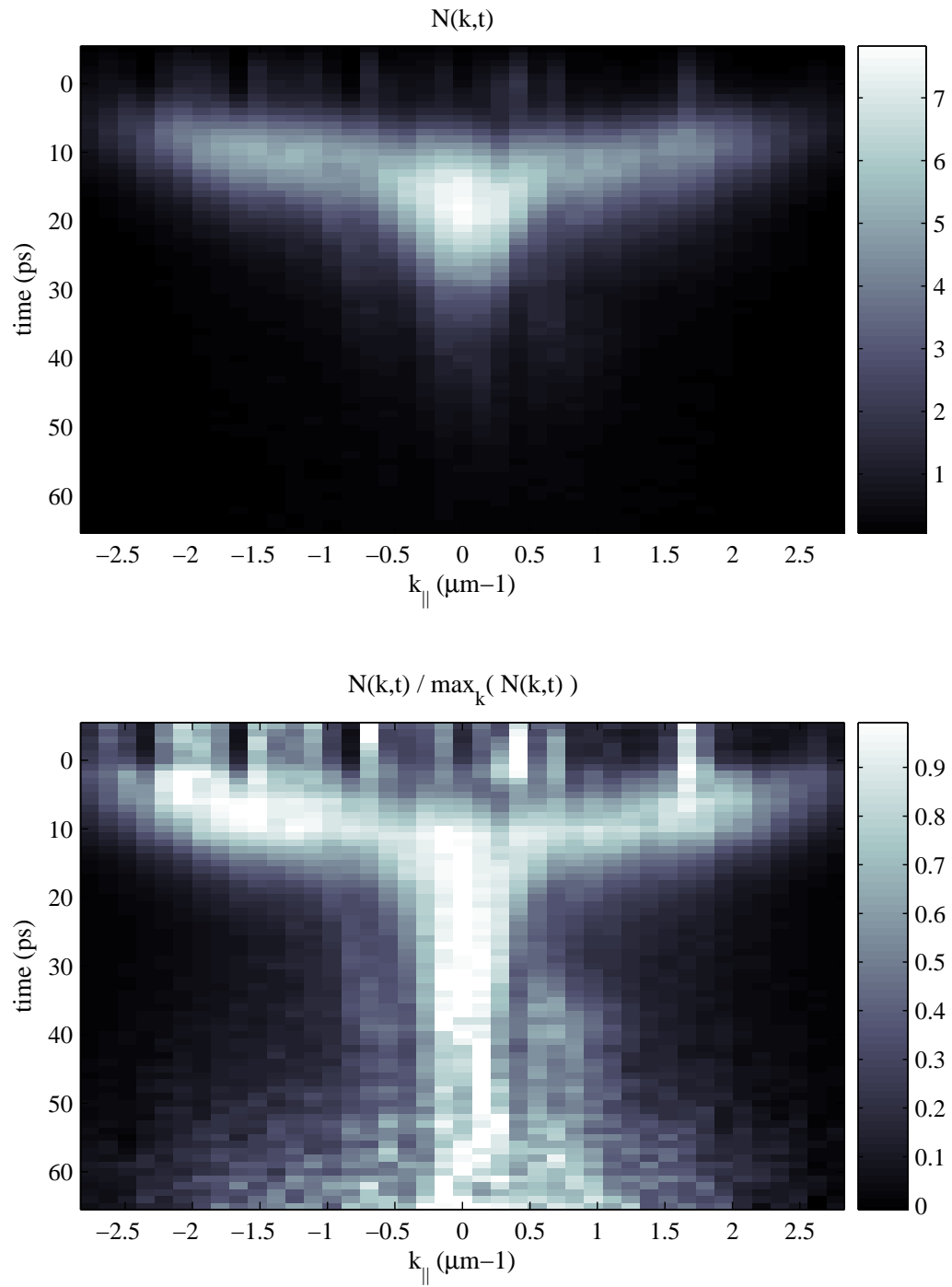
Figure 6.10: (a) $N(k_\parallel, t)$ and (b) normalized $N(k_\parallel, t)$ at $\Delta = -1$ meV, P=12 meV.
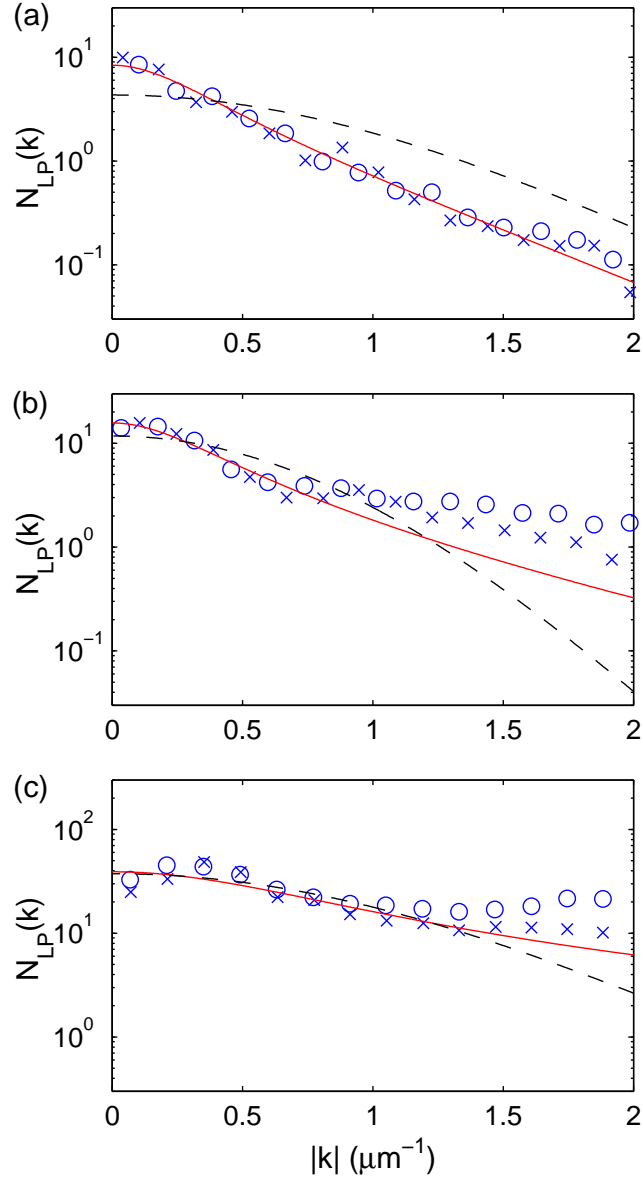
Figure 6.11: LP number per state $N(t, k_\parallel)$ vs. in-plane wavenumber $|k_\parallel|$ for different detunings at a time when T_{LP} reaches T_{min}: **(a)** $\Delta = 6.7$ meV, $P \approx 4P_{th}$; **(b)** $\Delta = -0.9$ meV, $P \approx 4P_{th}$; **(c)** $\Delta = -3.85$ meV, $P \approx 6P_{th}$. Crosses are data taken from the incidence direction of the pump, open circles are from the reflection direction, solid lines are fitting by BED, and dashed lines by MBD. Parameters for the curves are: **(a)** $T_{MB} = 4$ K, $T_{BE} = 4.4$ K, $\mu_{BE} = -0.04$ meV; **(b)** $T_{MB} = 4$ K, $T_{BE} = 8.1$ K, $\mu_{BE} = -0.13$ meV; **(c)** $T_{MB} = 8.5$ K, $T_{BE} = 182$ K, $\mu_{BE} = -0.4$ meV. From reference (4).
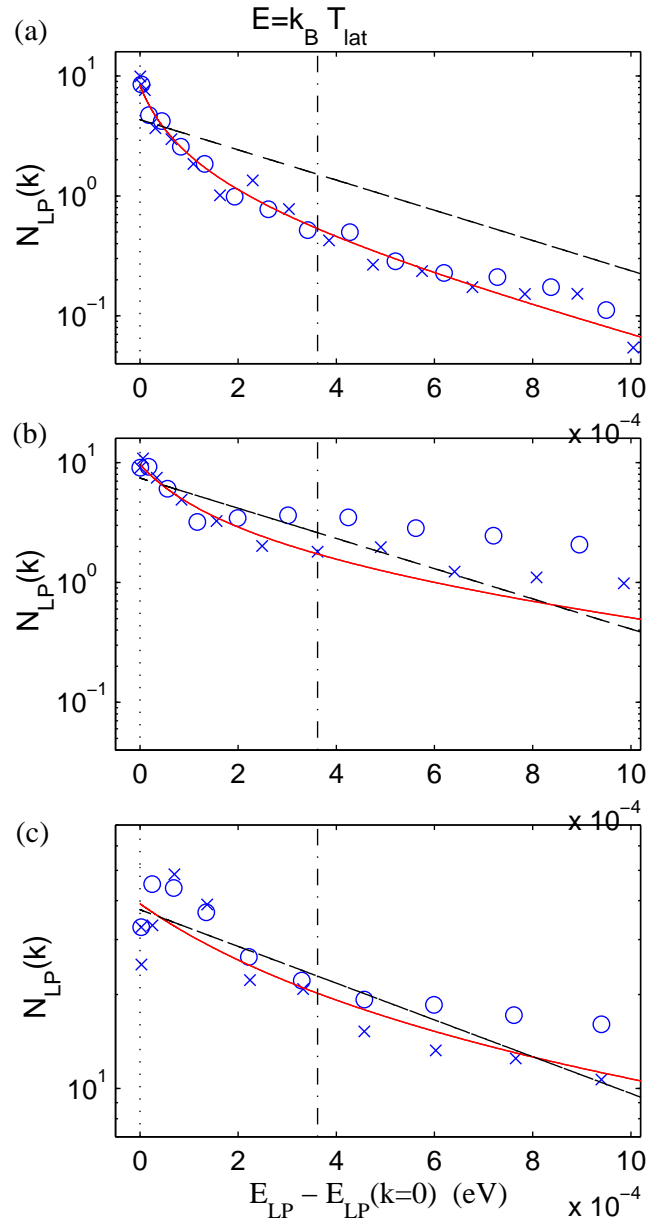
Figure 6.12: $N(t, E)$ vs. in-plane wavenumber $E-E_0$. Same parameters as figure 6.11.

quantum degeneracy threshold is still achieved at $k_\parallel \approx 0$. The momentum distribution in the region $|k_\parallel| < 0.4$—$1\mu m^{-1}$ agrees well with BE distribution (Figure 6.11 (b)). However, the fitted T_{LP} is larger than $3T_{lat}$. This suggests that LPs with small $k_\parallel$ can temporarily reach quasi-equilibrium among themselves via efficient LP-LP scattering, yet decay out of the system before they can be sufficiently cooled by phonon emission. It agrees qualitatively with the time integrated data before. At large negative detunings $\Delta < -1$ meV, a strong bottleneck prevents the system from reaching thermal equilibrium (Figure 6.11 (c)).

In figure 6.13 we plot the time evolution of the fitted LP temperature T_{LP} and normalized chemical potential α. For detunings $\Delta = 6.7$ and 9.0 meV, at 30—40 ps after the arrival of the pump pulse, phonon-scattering cools the system to a lowest temperature of $T_{min} \approx T_{lat}$ with a fitted chemical potential $\alpha \approx 0.1$. The quantum degenerate LP gas remains in thermal equilibrium at T_{lat} for a duration of about 20 ps. At the tail of the pulse, the LP population largely decays out of the system, μ increases to about $k_B T_{LP}$ and stimulated scattering diminishes. Since LPs at small $k_\parallel$ decay faster than those at larger $k_\parallel$, the temperature of the system starts to rise. The smallest chemical potential $\alpha = 3 \times 10^{-3}$—$10^{-1}$ is found at 10—20 ps after the pump pulse when $N_{LP}(t)$ is at its peak. For smaller detunings, T_{min} is higher than T_{lat}, so thermal equilibrium is not reached.

Note that the BE fitting is not as good at the beginning the very tail of the pulse, when T_{LP} is not close to its minimum value. T_{LP} and μ_{LP} obtained in these cases do not correspond to an actual temperature or chemical potential, since equilibrium is not fully established in the system. However, these T_{LP} and μ_{LP} still suggest a qualitative trend how the system evolves. For example, a higher fitted temperature always corresponds to broader distribution, and a more negative fitted chemical potential corresponds to a smaller occupancy per state, or vice versa. So we included in figure 6.13 the fitted T_{LP} and μ_{LP} from the beginning of the pulse as a reference to help understand the dynamics.

We choose a time 5—10 ps after the LP temperature reaches T_{min}, when the BE distribution agrees very well with the data, and plot the pump power dependence
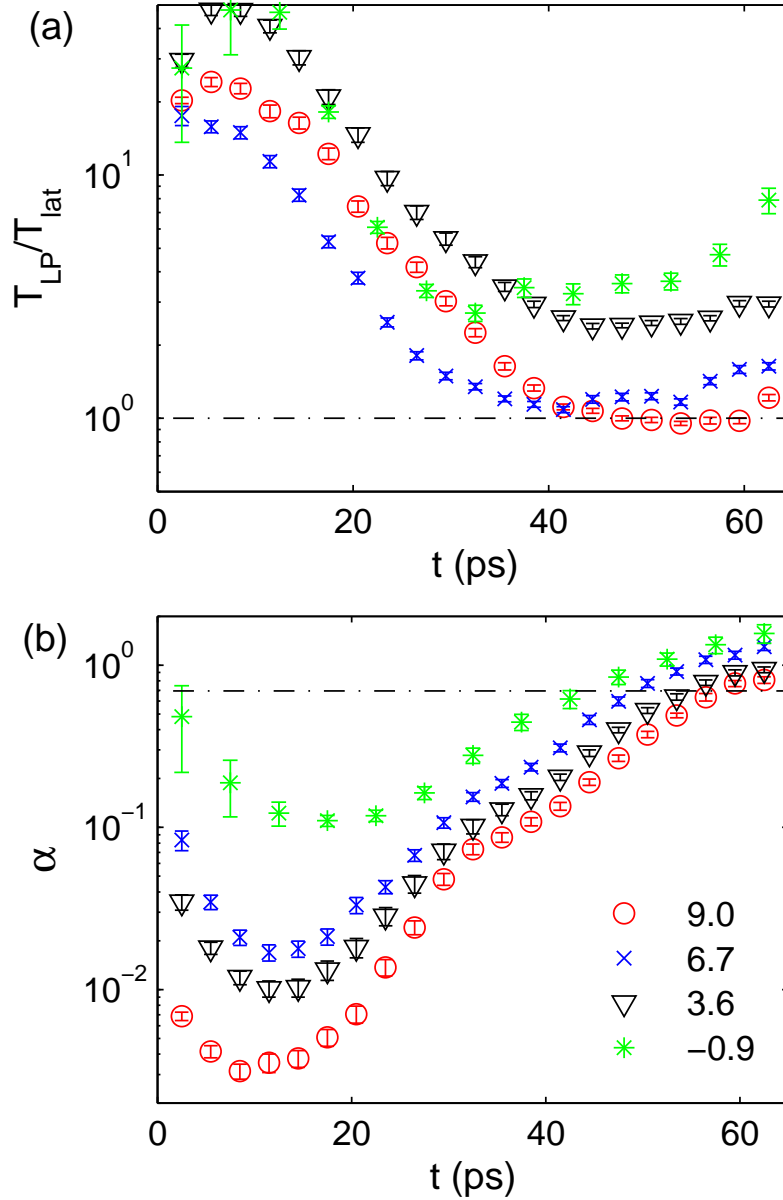
Figure 6.13: Time evolution of **(a)** normalized LP temperature T_{LP}/T_{lat} and **(b)** normalized chemical potential $\alpha = -\mu/k_B T$, obtained from BED fitting of the LP momentum distribution, at $T_{lat} = 4.2$ K and $P \approx 3P_{th}$. Δ in meV is given in the legend. From reference (4).
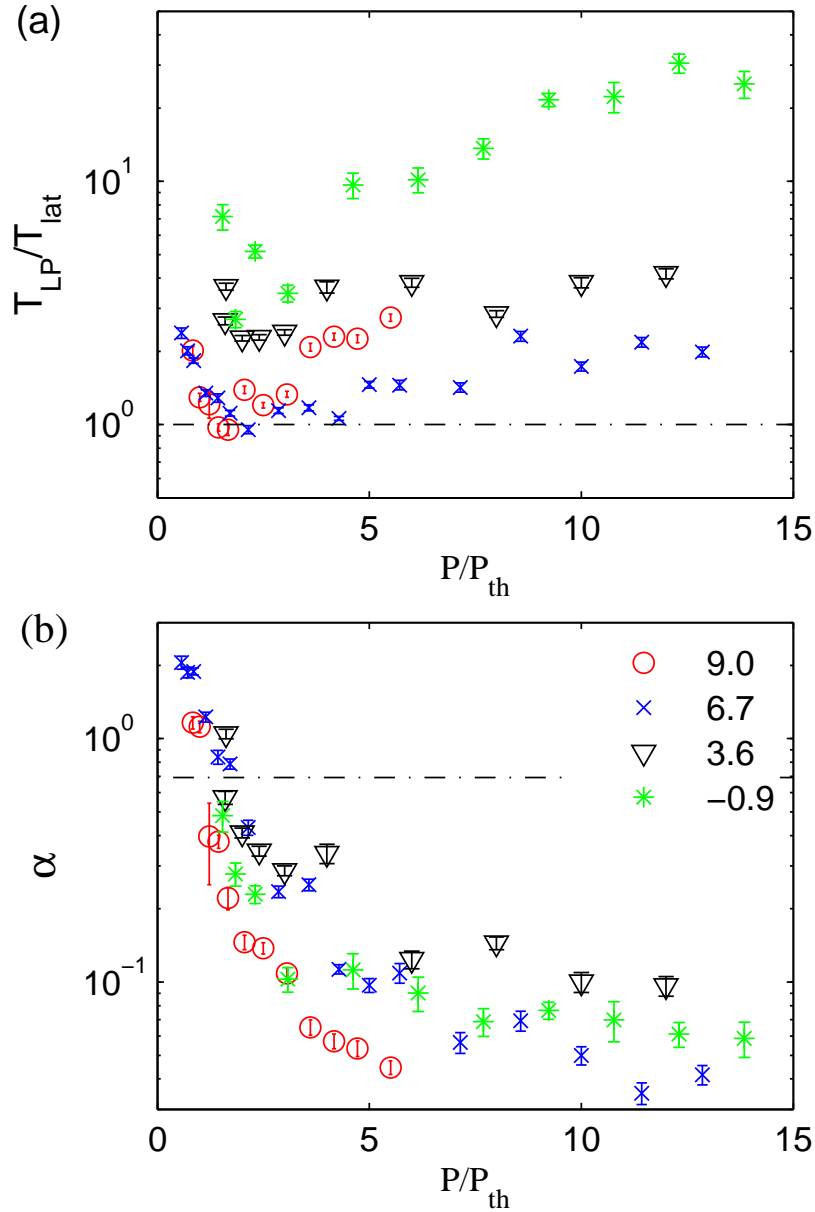
Figure 6.14: Pump dependence of **(a)** T_{LP}/T_{lat} and **(b)** $\alpha = -\mu/k_B T$, obtained from BED fitting of the LP momentum distribution. Time t is chosen as when T_{LP} is at its minimum. $T_{lat} = 4.2$ K. Δ in meV is given in the legend. From reference (4).

of T_{LP} and α in figure 6.14. α decreases with increasing pump level, crossing the quantum degeneracy threshold $\alpha = 0.7$ at $P \approx P_{th}$. This is because the stimulated scattering into the LP ground state becomes prominent when the LPs are quantum degenerate. In Figure 6.14 (a), T_{LP} drops to a minimum value at $P = 2$—$4P_{th}$. At approximately the same pump level, the thermalization time τ_{relax} reaches its minimum (Figure 6.8 (c)). At high pump levels, we notice that T_{LP} increases, possibly because T_{lat} increases due to insufficient heat dissipation of the sample to the copper cold finger.

6.4.5   Discussion

Momentum distribution provides insight to the quantum statistics of the LP system and reveals competition between the LP thermalization and decay. By adjusting the detuning Δ, we can control the lifetime and thermalization time of the LPs, hence the formation an equilibrium phase, as summarized in figure 6.6 and figure 6.15. At positive detunings and at pump levels above the quantum degeneracy threshold, the relaxation time τ_{relax} of the system is one tenth of the lifetime $\tau_{LP}(0)$ of the LP ground state, thermal equilibrium with the phonon bath is established for a period of about 20 ps, with a chemical potential μ_{LP} of about $-0.1k_B T$. Near resonance ($|\Delta| < 1$ meV), τ_{relax} is comparable to $\tau_{LP}(0)$. stimulated LP-LP scattering is still effective to achieve a quasi-equilibrium BE distribution among LPs in $k_\parallel < 1$ μm^{-1} at a temperature T_{LP} significantly higher than the lattice temperature T_{lat} with a chemical potential $\mu_{LP} = -0.01$ to $-0.1k_B T$. At large negative detunings, τ_{relax} is longer than $\tau_{LP}(0)$, so the system never reaches equilibrium.

6.5   Summary

In this chapter, we focus on the GaAs-based multiple-QW microcavity system to study the quantum statistical properties of polariton condensation. We found a decrease of the second order coherence of the ground state LPs, which indicates the formation of macroscopic coherence in the system. We observed a slow increase of the size of
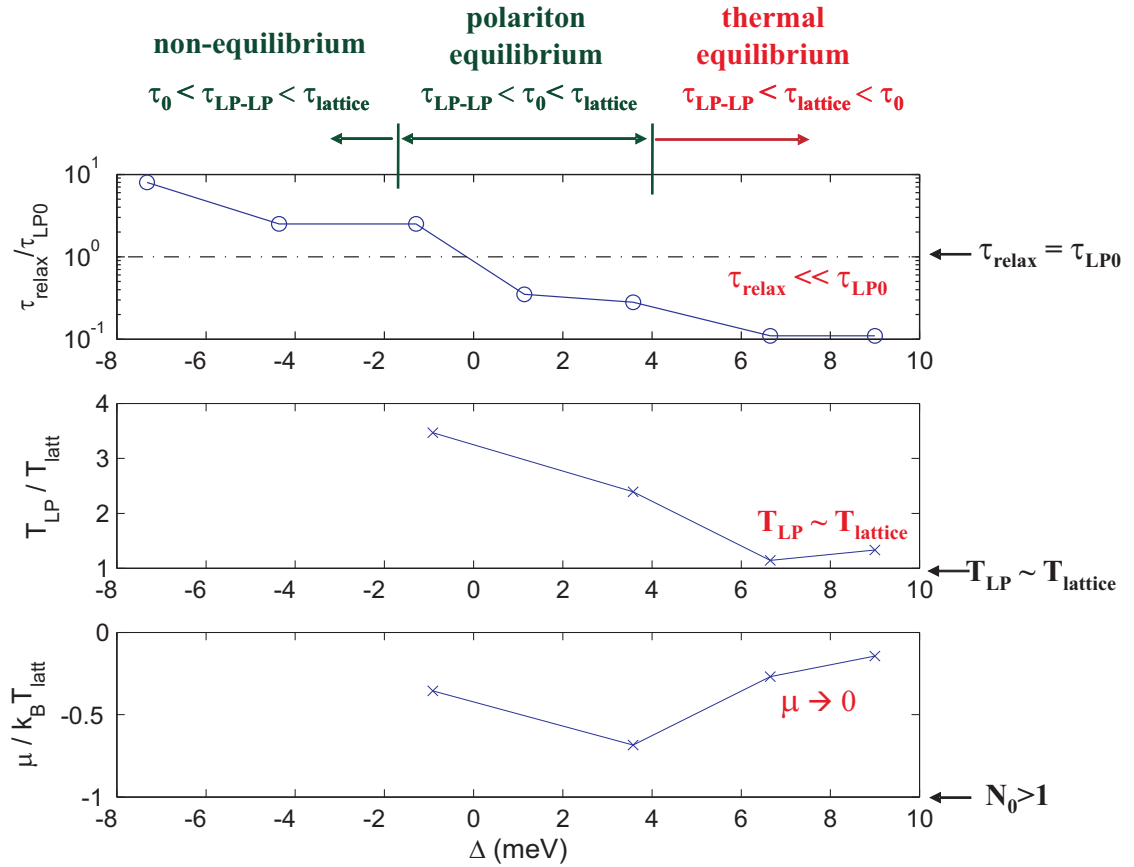
Figure 6.15: Detuning dependence of T_{LP}, α and τ_{rel}/τ_{LP}

the condensate as a result of its low dimensionality. And we measured a quantum degenerate BE distribution of the LPs above the quantum degeneracy threshold. These results all suggest that a phase transition has taken place in the system with a finite condensate fraction.

By controlling the detuning of the photon resonance relative to the exciton resonance, we can tune the energy relaxation dynamics, and observed a decrease of the LP effective temperature to the phonon bath temperature. Thermal equilibrium with the lattice is established in the condensed LP gas at positive detunings. A degenerate LP system, capable of reaching thermal equilibrium, is also valuable for studying the evolution from non-equilibrium to equilibrium phases, the distinction between classical and quantum systems, and the formation and dynamics of the order parameter of a quantum phase.

Quantitative dynamical models including LP-LP interactions will help to further elucidate the physics behind the data. It will also be interesting to evaluate how the quantum statistical properties of such a highly degenerate system are influenced by the finite energy linewidth of the LP modes, the non-uniformity of the spatial distribution, and the rather high group velocity of the LPs.

Chapter 7

Conclusion

In search of a phase transition in solids, we focus on GaAs-based twelve-QW micro-cavities in this thesis, and obtained the following results:

1. We observed a quantum degeneracy threshold of ground state LPs, at a density below the electronic population inversion density and two orders of magnitude lower than that of a photon laser realized in the same system.

2. At the quantum degeneracy threshold, we observed spontaneous build-up of a circular polarization of the emission of the LPs.

3. We demonstrated the formation of macroscopic coherence in the degenerate ground state by the measurement of the time-domain second order coherence function.

4. We observed an abnormal shrinkage of the spot-size of the emission, possibly explained by the system-size dependent critical density of BEC in two dimensions.

5. We measured an energy relaxation time τ_{relax} shorter than the lifetime τ_{LP} of the LPs in a range of positive detunings.

6. We observed thermal equilibrium condensation of the LPs when $\tau_{relax} < \tau_{LP}$.

The LP gas forms a quantum degenerate Bose-Einstein distribution at the lattice temperature for a duration of a few times of τ_{LP}. The corresponding chemical potential is close to zero.

Since the quantum degeneracy threshold is reached well below the electronic population inversion density, and it originates from a physical mechanism fundamentally different from that of a conventional photon laser, the microcavity polariton system promises a new source of coherent light with a fundamentally lower threshold than existing sources.

To make it into a practical device, however, one would prefer discrete mode structures which leads to clean single mode coherent emission, and most desirable is a system that survives at room temperature. Some preliminary efforts along these lines were also started in this thesis.

Transversely Confined Microcavity Polaritons

We imposed transverse optical trapping of the LPs by fabricating small pillar structures. Although discrete modes of LPs were observed, no clear evidence of quantum degeneracy threshold was obtained. This is partly because the cavity degrades in a pillar structure, leading to larger decoherence. In addition, when the laser pump arrives from a slant angle (to resonantly pump the high energy LPs), much of the light enters from the side wall of the pillar and induces excessive free electrons and holes. Consequently, a transition to the weak coupling regime took place before the LPs reach the quantum degeneracy threshold.

Surface passivation may help to resolve these problems. Alternatively, a new structure became available recently with built in optical-trapping by growth (71), and avoids both of the aforementioned problems.

Room Temperature Polaritons

Exciton binding energy imposes an upper bound on the host lattice temperature of a polariton system: $k_B T < E_B$. To have polaritons at room temperature, we look into

materials with large exciton binding energy, hence small Bohr radius and often large bandgap (in the visible to violet spectral region). We collaborated with a group which reported room temperature polaritons in a ZnSe-based quantum well microcavity in 2002, Pawlis et al. (72). Unfortunately the growth and fabrication process is still very difficult and not easily repeatable. We have not been able to observe polaritons again in this material system.

Other interesting candidates include GaN (73; 74) and ZnO. The common difficulty of these new systems is the lack of lattice-matched substrate and mirror materials. Thus the main challenge remains in fabrication of high quality samples with smaller inhomogeneous broadening, longer non-radiative lifetime, and with minimal build-in piezo-electric field that separates the electron and hole and reduces the exciton oscillator strength.

From a fundamental viewpoint, it will be interesting to directly measure the first and second order spatial coherence of a polariton condensate. A quantitative dynamical model is still in need which includes the LP-LP interaction, the finite lifetime of the LPs and the non-uniform spatial distributions. The thermal equilibrium condensate of LPs will be useful for further studies to elucidate the physics behind collective phenomena of polaritons, such as what is the exact ground state of the system, if a phase mode and superfluidity exist, and how the macroscopic coherence is established out of an original non-equilibrium gas, etc. Finally, the experimental challenge remains in accessing the part of the phase diagram at high polariton density with low decoherence rate (1), and to demonstrate, for example, the predicted BEC to BCS crossover.

Appendix A

Sample List

The samples discussed in this dissertation include:

1. S-CdTe,

2. S-GaAs-I,

3. S-GaAs-II.

A.1 S-CdTe

Sample S-CdTe is provided by Regis André at Dépt. de Recherche Fondamentale sur la Matire Condensée, CEA Centre d'Etudes de Grenoble, France. It consists of two QWs in a $\lambda/2$ cavity on CdTe substrate. The QWs 8 nm wide and made of CdTe. The cavity layer is $Cd_{0.6}Mg_{0.4}Te$. The top (air-side)DBR consists of 16.5 pairs of $\lambda/4$ $Cd_{0.75}Mn_{0.25}Te$ and $Cd_{0.6}Mg_{0.4}Te$ layers, with $Cd_{0.75}Mn_{0.25}Te$ layers at both the air and cavity interfaces. The bottom (substrate-side) DBR consists of 20 pairs of $\lambda/4$ $Cd_{0.75}Mn_{0.25}Te$ and $Cd_{0.6}Mg_{0.4}Te$, with $\lambda/4$ $Cd_{0.75}Mn_{0.25}Te$ at the cavity interface. At 4 K, the bare cavity lifetime is measured to be ~ 2 ps, the heavy hole exciton resonance is at 1.647 eV, and the normal mode splitting is 8.4 meV.

A.2   S-GaAs-I

Sample S-GaAs-I is provided by Jacqueline Bloch at CNRS, Paris, France. It consists of twelve QWs in a $\lambda/2$ cavity on GaAs substrate. The QWs are 7 nm wide and made of GaAs, separated by 3 nm AlAs barrier layers. The twelve QWs are grouped into three stacks, four in each stack, and placed at the central three anti-nodes of the cavity field: the center of the cavity, and the center of the first DBR pairs next to the cavity. The cavity layer is AlAs. The top DBR consists of 17.5 pairs of $\lambda/4$ $Ga_{0.8}Al_{0.2}As$ and AlAs layers, with $Ga_{0.8}Al_{0.2}As$ layers at both the air and cavity interfaces. The bottom DBR consists of 21 pairs of $\lambda/4$ $Ga_{0.8}Al_{0.2}As$ and AlAs layers, with $Ga_{0.8}Al_{0.2}As$ layers at the cavity interfaces. At 4 K, the bare cavity lifetime is measured to be $\sim$ 2 ps, the heavy hole exciton resonance is at 1.615 eV, and the normal mode splitting is 14.9 meV.

A sketch of the sample is shown in figure A.1 with the design-thickness of each layer labeled.

A.3   S-GaAs-II

Sample S-GaAs-II is provided by Rudolph Hey at Germany. It has the same structure as S-GaAs-I except that:

1. The $\lambda/4$ $Ga_{0.8}Al_{0.2}As$ layers in the DBRs are replaced by $\lambda/4$ $Ga_{0.85}Al_{0.15}As$ layers.

2. The QW layer thickness is 6.8 nm and the barrier layer thickness is 2.7 nm.

3. At 4 K, the bare cavity lifetime is $\sim$ 1.5 ps, the heavy hole exciton resonance is at 1.597 eV, and the normal mode splitting is 14.4 meV.

A sketch of the sample is shown in figure A.2 with the design-thickness of each layer labeled.

568Å

16x { 659Å

568Å

435.5Å

4 GaAs quantum wells 70Å
AlAs barriers 30Å

348Å

425Å

4 GaAs quantum wells 70Å
AlAs barriers 30Å

425Å

348Å

4 GaAs quantum wells 70Å
AlAs barriers 30Å

435.5Å

$Ga_{0.8}Al_{0.2}As$ 20x {   568Å

AlAs   659Å

Substrate
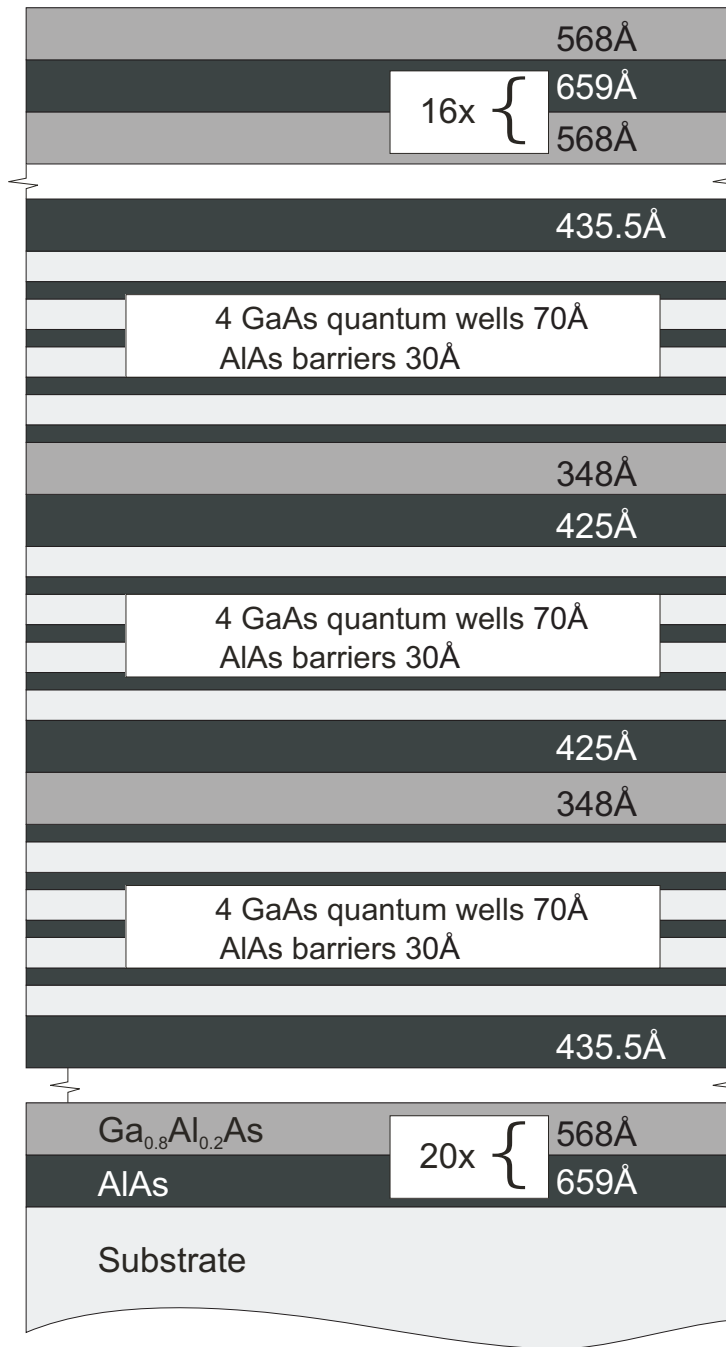
Figure A.1: Sketch of S-GaAs-I
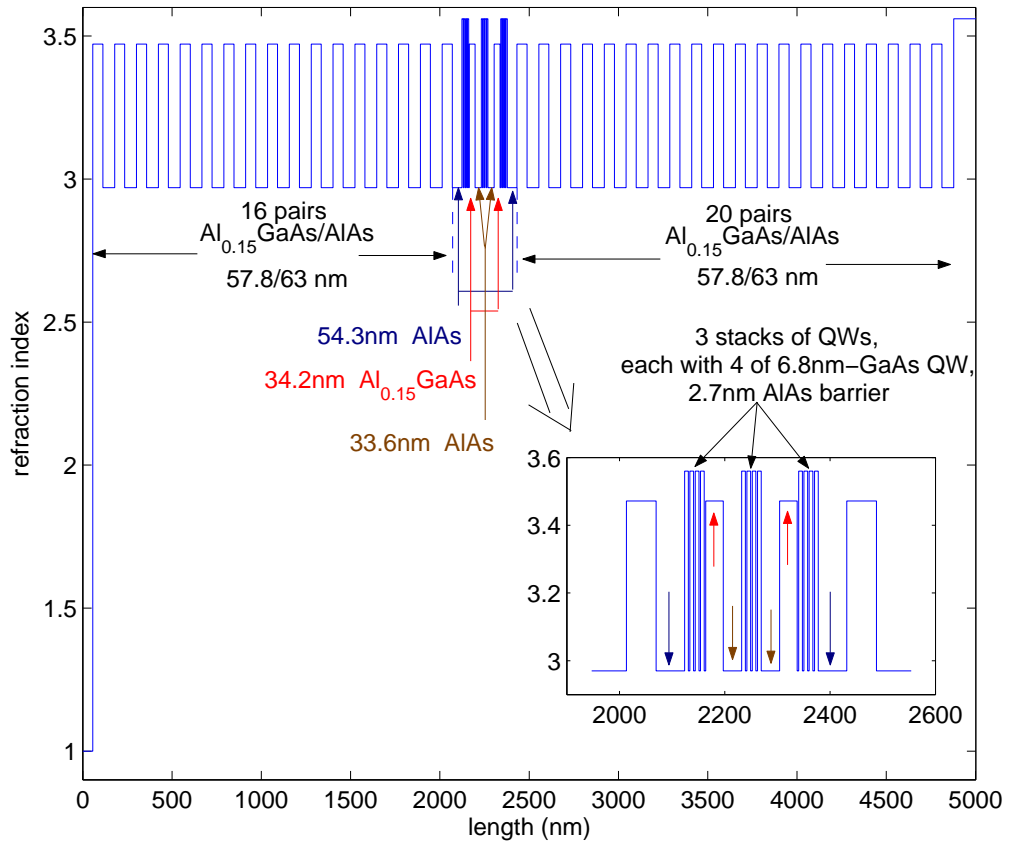
Figure A.2: Sketch of S-GaAs-II

Appendix B

Interference in matter-wave amplification

We investigate the quantum interference effects in two types of matter-wave mixing experiments: one with initial matter waves prepared in independent Fock states (type I) and the other with each individual particle prepared in a same coherent superposition of states (type II). In the type I experiment, a symmetric wavefunction of bosons leads to constructive quantum interference and shows final state stimulation, while an anti-symmetric wavefunction of fermions results in destructive quantum interference and inhibited matter wave mixing. In the type II experiment, a coherent superposition state leads to constructive quantum interference and enhanced matter wave mixing for both bosons and fermions, independent of their quantum statistics.

With the realization of Bose-Einstein condensation (BEC) in atoms, bosonic final state stimulation involving atom condensates has been studied in superradiance of atoms (75) , four-wave mixing (FWM) (76) , and matter wave amplification (77; 78). Following these work, it was pointed out that these phenomena are not unique in boson systems but also possible in fermion systems (79; 80). In these experiments ((75)- (78)), the input matter waves, characterized by their momenta, are all prepared from a same condensate by a coherent partition process of each individual particle. Hence the observed nonlinearity can be understood as collective enhancement effect, analogous to super-radiance in an ensemble of two-level atoms in Dicke state or Bloch
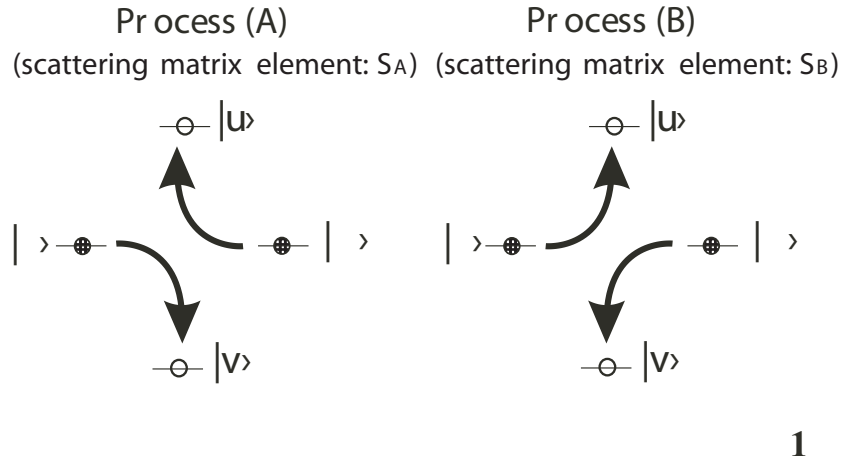
Figure B.1: Illustration of the two scattering processes (A) and (B) in FWM experiments.

state (81; 82), and does not depend on the quantum statistics of the particles. We call such experiments *type II* in this paper. In another kind of experiment, which we call *type I* here, all input matter waves consist of independent real populations of the particle. In this case, final state stimulation occurs in a boson system, while inhibition of matter-wave mixing is expected in a fermion system. Type I experiment has not yet been performed with atomic BECs, but has been recently demonstrated with exciton-polaritons in semiconductors (65; 30).

In this paper, We investigate the two types of matter-wave mixing in terms of the quantum interference among different paths, naturally originating from the symmetrization (anti-symmetrization) procedure for type I, or artificially created from the coherent superposition state for type II. Figure B.2 shows a model FWM experiment where two input states $|\phi\rangle$ and $|\psi\rangle$ elastically scatter into two output states $|u\rangle$ and $|v\rangle$ via the two possible processes (A) and (B), with scattering amplitudes S_A and S_B, respectively (83). The scattering processes are governed by a unitary

operator $\hat{U}_{int}$, s.t.,

$$S_A = \; _2\langle u|_1\langle v|\hat{U}_{int}(t)|\phi\rangle_1|\psi\rangle_2 = \; _2\langle v|_1\langle u|\hat{U}_{int}(t)|\psi\rangle_1|\phi\rangle_2, \tag{B.1}$$

$$S_B = \; _2\langle v|_1\langle u|\hat{U}_{int}(t)|\phi\rangle_1|\psi\rangle_2 = \; _2\langle u|_1\langle v|\hat{U}_{int}(t)|\psi\rangle_1|\phi\rangle_2. \tag{B.2}$$

B.1 Type I experiment

In type I experiment, the four initial matter waves have definite populations (Fock states). Let's first consider the case where there is one particle in each of the two input states and one particle in one output state, with the initial state of the system:

$$\begin{aligned}
|i_I\rangle &= \sum_{i\neq j} \hat{P}_{ij}[|\phi\rangle_1|v\rangle_2|\psi\rangle_3] \\
&= \frac{1}{\sqrt{6}}[|\phi\rangle_1|v\rangle_2|\psi\rangle_3 \pm |v\rangle_1|\phi\rangle_2|\psi\rangle_3 \pm |\psi\rangle_1|v\rangle_2|\phi\rangle_3 \\
&\quad + |v\rangle_1|\psi\rangle_2|\phi\rangle_3 \pm |\phi\rangle_1|\psi\rangle_2|v\rangle_3 + |\psi\rangle_1|\phi\rangle_2|v\rangle_3],
\end{aligned} \tag{B.3}$$

where $\hat{P}_{ij}$ is the symmetrization or anti-symmetrization operators (83). The upper sign is for bosons, and the lower sign is for fermions, in accordance with symmetrization postulate for bosons and fermions, respectively. Scattering results in final states with two particles in state $|v\rangle$ and one particle in state $|u\rangle$. Take a final state $|v\rangle_1|v\rangle_2|u\rangle_3$ as an example (figure B.2(a)), it can be reached by scattering (A) or (B) from each of the first four terms in the initial state $|i_I\rangle$. The corresponding scattering amplitudes for the four paths are $S_A C$, $\pm S_A C$, $\pm S_B C$, and $S_B C$, where C is a real normalization factor, $C = 1/\sqrt{6}$ in this example. Thus the total scattering amplitude for bosons adds up to $2(S_A + S_B)C$ as a result of constructive quantum interference; while for fermions it is suppressed to zero due to destructive quantum interference. This illustrates how quantum interference leads to final state stimulation for bosons, and inhibited FWM for fermions.

In general, if the initial matter waves of a boson system consists of n_1 particles in $|\phi\rangle$, n_2 particles in $|\psi\rangle$, n_3 particles in $|v\rangle$, and $n = n_1 + n_2 + n_3$ particles in total, the

(a)   Type I experiment

	initial state	scattering	final state
	$+|\phi\rangle_1|v\rangle_2|\psi\rangle_3$	S_A	
$(1\leftrightarrow2)$	$\pm|v\rangle_1|\phi\rangle_2|\psi\rangle_3$	S_A	
$(1\leftrightarrow3)$	$\pm|\psi\rangle_1|v\rangle_2|\phi\rangle_3$	S_B	$|v\rangle_1|v\rangle_2|u\rangle_3$
$(1\leftrightarrow2,\ 2\leftrightarrow3)$	$+|v\rangle_1|\psi\rangle_2|\phi\rangle_3$	S_B	

total scattering amplitude : $\begin{cases} 2(S_A + S_B) & \textbf{bosons} \\ 0 & \textbf{fermions} \end{cases}$

(b)   Type II experiment (i)

	initial state	scattering	final state
	$+|\phi\rangle_1|v\rangle_2|\psi\rangle_3$	S_A	
coherent	$+|v\rangle_1|\phi\rangle_2|\psi\rangle_3$	S_A	
superposition	$+|\psi\rangle_1|v\rangle_2|\phi\rangle_3$	S_B	$|v\rangle_1|v\rangle_2|u\rangle_3$
	$+|v\rangle_1|\psi\rangle_2|\phi\rangle_3$	S_B	

total scattering amplitude : $2(S_A + S_B)$ **bosons or fermions**

(c)   Type II experiment (ii)

	initial state	scattering	final state
coherent	$+|\phi\rangle_1|\phi\rangle_2|\psi\rangle_3$	S_A	
superposition	$+|\phi\rangle_1|\psi\rangle_2|\phi\rangle_3$	S_B	$|\phi\rangle_1|v\rangle_2|u\rangle_3$

total scattering amplitude : $(S_A + S_B)$ **bosons or fermions**

2

Figure B.2: Possible paths of scattering leading to the final state (a) $|v\rangle_1|v\rangle_2|u\rangle_3$ in type I experiment, (b) $|v\rangle_1|v\rangle_2|u\rangle_3$ in type II experiment, and (c) $|\phi\rangle_1|v\rangle_2|u\rangle_3$ in type II experiment. In (a), the upper sign is for bosons, the lower sign is for fermions. The total scattering amplitudes is enhanced for bosons, and is suppressed to zero for fermions in this type I experiment. In (b) and (c), the scattering amplitudes are the same for both bosons and fermions. It is enhanced in (c), but there is no interference leading to enhanced or suppressed scattering in (c)

.

initial-state is:

$$|i\rangle_{IB} = \frac{1}{\sqrt{N}}[\prod_{i=1}^{n_1}|\phi\rangle_i \prod_{j=n_1+1}^{n_1+n_2}|\psi\rangle_j \prod_{k=n_1+n_2+1}^{n}|v\rangle_k$$

$$+ \text{ permutation terms due to}$$

$$\text{symmetrization postulate }]. \tag{B.4}$$

All the permutations add to a total number of $N = \binom{n}{n_1}\binom{n-n_1}{n_2}$ different terms in the bracket. Any one of the n_1 particles in $|\phi\rangle$ and any one of the n_2 particles in $|\psi\rangle$ can scatter into $|v\rangle$ and $|u\rangle$ via the two processes (A) and (B). Process (A) results in a total of $N_2 = N\binom{n_1}{1}\binom{n_2}{1}$ terms in the final state $|\tilde{f}\rangle_{IB} = \hat{U}_{int}|i\rangle_{IB}$. Each of these terms has one particle in $|u\rangle$, $n_1 - 1$ particles in $|\phi\rangle$, $n_2 - 1$ particles in $|\psi\rangle$, and $n_3 + 1$ particles in $|v\rangle$. Hence there are only $N_3 = \binom{n}{1}\binom{n-1}{n_1-1}\binom{n-n_1}{n_2-1}$ physically distinct terms in the final state. Due to the symmetry property of the initial state (B.4), all these N_3 terms have the identical probability amplitude $S_A c_{IB} = S_A(\frac{N_2}{N_3})/\sqrt{N}$. Same analysis applies to the process (B) except that the probability amplitude of each term is $S_B c_{IB} = S_B(\frac{N_2}{N_3})/\sqrt{N}$. The normalized final state is $|f\rangle_{IB} = |\tilde{f}\rangle_{IB}/\sqrt{_{IB}\langle\tilde{f}|\tilde{f}\rangle_{IB}}$. The scattering amplitude is:

$$a_{IB} =_{IB}\langle f|\hat{U}_{int}|i\rangle_{IB} =_{IB}\langle f|\tilde{f}\rangle_{IB} = \sqrt{_{IB}\langle\tilde{f}|\tilde{f}\rangle_{IB}}$$

$$= \sqrt{N_3 c_{IB}^2}|S_A + S_B|$$

$$= \sqrt{n_1 n_2(n_3 + 1)}|S_A + S_B|. \tag{B.5}$$

It shows that the scattering rate is proportional to the product of the numbers of particles (n_1 and n_2) in the input states and is enhanced by the initial occupancy n_3 of the output state $|v\rangle$.

In the case of a fermion system, the initial state is:

$$|i\rangle_{IF} = \frac{1}{\sqrt{n!}}[|\phi^{(1)}\rangle_1|\phi^{(2)}\rangle_2...|\phi^{(n_1)}\rangle_{n_1}|\psi^{(1)}\rangle_{n_1+1}...|\psi^{(n_2)}\rangle_{n_1+n_2}|v^{(1)}\rangle_{n_1+n_2+1}...|v^{(n_3)}\rangle_n$$

$$+ \text{ permutation terms due to anti-symmetrization postulate}], \tag{B.6}$$

Here the superscripts $(1), (2), \ldots$ are labels of another quantum number q, which is conserved during the scattering processes. Thus, for example, the n_1 particles occupy nearly degenerate but distinct states $|\phi^{(1)}\rangle_1$, $|\phi^{(2)}\rangle_2$, etc. Scattering is only among the four states with identical quantum number q (from $|\phi^q\rangle$ and $|\psi^q\rangle$ to $|u^q\rangle$ and $|v^q\rangle$), all scattering governed by the same unitary matrix $\hat{U}_{int}$. This also implies the same energy spacing between states (p, q_1) and (p, q_2) for $p = \phi, \psi, u$ and v. Thus states such as $(|\psi^{q_1}\rangle + |\phi^{q_1}\rangle + |v^{q_1}\rangle)$ and $(|\psi^{q_2}\rangle + |\phi^{q_2}\rangle + |v^{q_2}\rangle)$ evolve in the same way.

In the state B.6, there are a total of $n!$ physically distinct terms in the bracket. Due to the anti-symmetrized form of the initial state, scattering amplitude cancel out exactly between different paths if they lead to a final state with two particles in a same state $|v\rangle$. For a scattering process in which two particles are scattered into initially unoccupied $|v\rangle$ and $|u\rangle$, there is no other paths interfering with it. Explicitly, the total scattering amplitude $_{IF}\langle f|\hat{U}_{int}|i\rangle_{IF}$ is:

$$
a_{IF} = \begin{cases}
0, & \text{if } n_3 \geq n_1, n_2, \\
\sqrt{(n_1 - n_3)n_2}|S_A|, & \text{if } n_1 > n_3 \geq n_2, \\
\sqrt{(n_2 - n_3)n_1}|S_B|, & \text{if } n_2 > n_3 \geq n_1, \\
[(n_1 - n_3)n_2|S_A|^2 + (n_2 - n_3)n_1|S_B|^2 \\
\quad + 2(n_2 - n_3)(S_A S_B^* + S_A^* S_B)]^{1/2}, & \text{if } n_1 > n_2 > n_3, \\
[(n_1 - n_3)n_2|S_A|^2 + (n_2 - n_3)n_1|S_B|^2 \\
\quad + 2(n_1 - n_3)(S_A S_B^* + S_A^* S_B)]^{1/2}, & \text{if } n_2 > n_1 > n_3.
\end{cases}
\tag{B.7}
$$

It shows that if there are initially more particles in an ensemble of nearly degenerate states $|v\rangle$ than in $|\phi\rangle$ and $|\psi\rangle$, the scattering into $|v\rangle$ and $|u\rangle$ is completely suppressed. Otherwise, the amplitude is non-zero but still suppressed by the increase of n_3.

B.2 Type II experiment

In contrast to the type I experiment, each particle in the initial matter waves of a type II experiment is in a same coherent superposition of the states $|\phi\rangle$, $|\psi\rangle$, and $|v\rangle$. In a boson system, if there are n particles in total, and each particle prepared in an

identical superposition state, the initial-state wavefunction of bosons is:

$$|i\rangle_{IIB} = \prod_{i=1}^{n}(\sqrt{\frac{1-\epsilon}{2}}|\phi\rangle_i + \sqrt{\frac{1-\epsilon}{2}}|\psi\rangle_i + \sqrt{\epsilon}|v\rangle_i) \tag{B.8}$$

The expansion of (B.8) consists of a total of 3^n different terms. There are $N_{mk} = \binom{n}{m}\binom{n-m}{k}$ terms which have m particles in $|\phi\rangle$, k particles in $|\psi\rangle$ and (n-m-k) particles in $|v\rangle$. Here m takes values from 0 to n, for each m, k takes values from 0 to n-m. We call this group of N_{mk} terms as (m,k) group. All terms in the same (m,k) group have the same probability amplitude $c_{mk}^0 = (\frac{1-\epsilon}{2})^{n/2}\eta^{\frac{n-m-k}{2}}$, where $\eta = \frac{2\epsilon}{1-\epsilon}$. It is obvious from the expansion that $|i\rangle_{IIB}$ is already fully symmetric, and no additional symmetrization procedure is necessary.

For each (m,k) group, possible scattering of a pair of $|\phi\rangle_i$ and $|\psi\rangle_j$ into $|v\rangle_i|u\rangle_j$ via process (A) results in a total of $N_2' = mkN_{mk}$ terms, each of which has one particle in $|u\rangle$, (m-1) particles in $|\phi\rangle$, (k-1) particles in $|\psi\rangle$ and (n-m-k+1) particles in $|v\rangle$. However, there are only $N_3' = \binom{n}{1}\binom{n-1}{m-1}\binom{n-m}{k-1}$ physically distinct terms. Since the initial state is symmetric, the initial group (m,k) is scattered into N_3' different terms, all with the same probability amplitude $S_A c_{mk}' = S_A c_{mk}^0 \frac{N_2'}{N_3'} = c_{mk}^0 \cdot 2(n-m-k+1)$. Similarly, scattering via process (B) contributes $S_B c_{mk}'$ to the probability amplitude. The final state $|\tilde{f}\rangle_{IIB} = \hat{U}_{int}|i\rangle_{IIB}$ is a sum of terms scattered from all (m,k) groups. Hence the total scattering amplitude is:

$$
\begin{aligned}
a_{IIB} &= \sqrt{_{IIB}\langle \tilde{f}|\tilde{f}\rangle_{IIB}} \\
&= \sqrt{\sum_{m=1}^{n-1}\sum_{k=1}^{n-m} N_3'(m,k)(c_{mk}'|S_A + S_B|)^2} \\
&= \sqrt{[\frac{1-\epsilon}{2}n][\frac{1-\epsilon}{2}(n-1)][\epsilon(n-2)+1]}|S_A + S_B|. \tag{B.9}
\end{aligned}
$$

When $n \gg 1$, the scattering rate is again proportional to the product of the average numbers of particles in the two input states (the first two terms in the last line of (B.9) corresponding to n_1 and n_2 in type I experiment), and is enhanced by the final state population by a factor $\epsilon(n-2)+1$, where $\epsilon(n-2)$, the average population in

$|v\rangle$, corresponds to n_3 in the type I experiment.

For type II experiment, a fermion system has exactly the same scattering amplitude. The initial state for fermions is

$$|i\rangle_{IIF} = \frac{1}{N'}[(\frac{1-\epsilon}{2})^{n/2} \prod_{i=1}^{n}(|\phi^{(i)}\rangle_i + |\psi^{(i)}\rangle_i + \sqrt{\eta}|v^{(i)}\rangle_i)$$

$$+ \text{ permutation terms due to anti-symmetrization postulate}]., \qquad (B.10)$$

where N' is a normalization factor. Since each particle has a different quantum number q, and q is conserved under the operation of $\hat{U}_{int}$, terms in the expansions of different anti-symmetrization groups do not interfere with each other, even after scattering. At the same time, all anti-symmetrization groups have identical scattering characteristics. Therefore it is sufficient to consider only the first line of (B.10), setting $N' = 1$. In another word, symmetrization postulate and thus quantum statistics does not affect the scattering amplitude in type II experiment. Moreover, the label for quantum number q in (B.10) has a one to one correspondence to the label of the particle number, so the label for quantum number q can be suppress and (B.10) is reduced to the same form as (B.8), leading to $a_{IIF} = a_{IIB}$. This collective enhancement effect for fermion matter waves is analogous to the super-radiance of two level atoms prepared in a Bloch state (82). The field in the vacuum state and an atom in the excited state (corresponding to particles in $|\phi\rangle$ and $|\psi\rangle$) interact and transform into the field in one-photon state and the atom in the ground state (corresponding to particles in $|u\rangle$ and $|v\rangle$). Super-radiance, or enhanced transition rate, is expected if atoms are prepared in Bloch state, i.e., if each atom is in a coherent superposition of the excited state and the ground state through the interaction with highly excited coherent light.

We again consider a simple case of three particles, each particle occupying the three states $|\phi\rangle$, $|\psi\rangle$ and $|v\rangle$ with equal probability. Then the initial state of bosons

and the reduced initial state of fermions has the same form:

$$|i> = (|\phi\rangle_1 + |\psi\rangle_1 + |v\rangle_1) \otimes (|\phi\rangle_2 + |\psi\rangle_2 + |v\rangle_2)$$
$$\otimes (|\phi\rangle_3 + |\psi\rangle_3 + |v\rangle_3)$$

To reach a final state $|v\rangle_1 |v\rangle_2 |u\rangle_3$, there are four possible paths, as illustrated in figure B.2 (b). The corresponding four terms in the initial state $|i\rangle$ originate from a coherent superposition state instead of the symmetrization or anti-symmetrization procedure. Therefore paths from each process are additive for both bosons and fermions. The constructive interference between different paths leads to enhanced scattering amplitude. To have an intuitive picture of the enhancement by the final state occupancy (corresponding to the $\epsilon(n-2)$ term in (B.9)), we consider the case where there are no particle in $|v\rangle$ before scattering. Then only two paths are possible, as shown in figure B.2 (c), and no interference terms to lead to enhancement in this case.

As discussed above, type II experiment will produce identical enhancement in scattering amplitude for both boson and fermion systems, given that the initial state of the system is prepared as a coherent superposition of all three states $|\phi\rangle$, $|\psi\rangle$ and $|v\rangle$. The enhancement comes from constructive multi-particle interference, where the different paths are created by preparing the initial state in a coherent superposition-state. Type I experiment, however, will reveal final state stimulation for bosons and inhibited-FWM for fermions (Pauli blocking). The enhancement and inhibition in this case come from constructive and destructive multi-particle interference, where the different paths stem from the symmetrization and anti-symmetrization postulate. So only type I experiment tests the true quantum statistics of the system. The final state stimulation (65), matter wave amplification (30) and condensation of exciton polaritons (84) have been demonstrated in this type of experiment, but the counterpart experiments in atomic systems are yet to be observed.

Bibliography

[1] Littlewood, P., Eastham, P., Keeling, J., Marchetti, F. & Szymanska, M. Models of coherent exciton condensation. *J. Phys.: Cond. Matt.* **16**, S3597–S3620 (2004) and refereces therein.

[2] Greene, R., Bajaj, K. & Phelps, D. Energy levels of wannier excitons in gaas-gasub 1-xalsub xas quantum-well structures. *Physical Review B (Condensed Matter)* **29**, 1807–1812 (1984).

[3] Deng, H., Weihs, G., Santori, C., Bloch, J. & Yamamoto, Y. Dynamic condensation of polaritons in a semiconductor microcavity. *Science* **298**, 199–202 (2002).

[4] Deng, H., Weihs, G., Snoke, D., Bloch, J. & Yamamoto, Y. Polariton lasing vs. photon lasing in a semiconductor microcavity. *Proc. Natl. Acad. Sci.* **100**, 15318–15323 (2003).

[5] Weisbuch, C., Nishioka, M., Ishikawa, A. & Arakawa, Y. Observation of the coupled exciton-photon mode splitting in a semiconductor quantum well microcavity. *Phys. Rev. Lett.* **69**, 3314–3317 (1992).

[6] Keldysh, L. & Kozlov, A. N. Collective properties of excitons in semiconductors. *Sov. Phys. JETP* **27**, 521–528 (1968).

[7] Comte, C. & Nozières, P. Exciton bose condensation: the ground state of an electrion-hole gas i. mean field description of a simplified model. *J. Phys.* **43**, 1069–1081 (1982).

[8] Malpuech, G., Rubo, Y., Laussy, F., Bigenwald, P. & Kavokin, A. Polariton laser: thermodynamics and quantum kinetic theory. *Semicond. Sci. Technol.* **18**, S395–S404 (2003).

[9] Sarchi, D. & Savona, V. Kinetic theory of non-equilibrium condensation of microcavity polaritons. *arXiv.org:cond-mat/0411084 and 0603106* (2006).

[10] Griffin, A., Snoke, D. W. & Stringari, S. *Bose-Einstein Condensation* (Cambridge Univ. Press, Cambridge, 1995).

[11] Anderson, M. H., Ensher, J. R., Matthews, M. R., Wieman, C. E. & Cornell, E. A. Observation of Bose-Einstein condensation in a dilute atomic vapor. *Science* **269**, 198 (1995).

[12] Davis, K. B. *et al.* Bose-Einstein condensation in a gas of sodium atoms. *Phys. Rev. Lett.* **75**, 3969 (1995).

[13] Bradley, C. C., Sackett, C. A., Tollett, J. J. & Hulet, R. G. Evidence of Bose-Einstein condensation in an atomic gas with attractive interactions. *Phys. Rev. Lett.* **75**, 1687 (1995) *ibid.* **79**, 1170 (1997).

[14] Fried, D. G. *et al.* Bose-Einstein condensation of atomic hydrogen. *Phys. Rev. Lett.* **81**, 3811 (1998).

[15] Robert, A. *et al.* A Bose-Einstein condensate of metastable atoms. *Science* **292**, 461 (2001).

[16] Pereira Dos Santos, F. *et al.* Bose-einstein condensation of metastable helium. *Phys. Rev. Letters* **86**, 3459–3462 (2001).

[17] Moskalenko, S. A. Reversible optico-hydrodynamic phenomena in a nonideal exciton gas. *Fiz. Tverd. Tela* **4**, 276–284 (1962).

[18] Blatt, J., Brandt, W. & Boer, K. Bose-einstein condensation of excitons. *Phys. Rev.* **126**, 1691–1692 (1962).

[19] Wolfe, J. P., Lin, J. L. & Snoke, D. W. Bose-Einstein condensation of a nearly ideal gas: Excitons in Cu_2O in *Bose-Einstein Condensation* (eds. Griffin, A., Snoke, D. W. & Stringari, S.) 281 (Cambridge University Press, 1995).

[20] Warren, J. T., O'Hara, K. E. & Wolfe, J. P. Two-body decay of thermalized excitons in cu_2o. *Phys. Rev. B* **61**, 8215–8223 (2000).

[21] O'Hara, K. E. & Wolfe, J. P. Relaxation kinetics of excitons in cuprous oxide. *Phys. Rev. B* **62**, 12909–12922 (2000).

[22] Jang, J. P. New perspectives on kinetics of excitons in cu2o. *Solid State Communications* **134**, 143–149 (2005).

[23] Butov, L. V., Gossard, A. C. & Chemla, D. S. Macroscopically ordered state in an exciton system. *Nature* **418**, 751–754 (2002).

[24] Snoke, D., Denev, S., Liu, Y., Pfeiffer, L. & West, K. Long-range transport in excitonic dark states in coupled quantum wells. *Nature* **418**, 754–757 (2002).

[25] Butov, L. V. *et al.* Stimulated scattering of indirect excitons in coupled quantum wells: signature of a degenerate bose-gas of excitons. *Phys. Rev. Lett.* **86**, 5608–5611 (2001).

[26] Butov, L. V., Lai, C. W., Ivanov, A. L., Gossard, A. C. & Chemla, D. S. Towards bose-einstein condensation of excitons in potential traps. *Nature* **417**, 47–52 (2002).

[27] Dang, L. S., Heger, D., André, R., Boeuf, F. & Romestain, R. Stimulation of polariton photoluminescence in semiconductor microcavity. *Phys. Rev. Lett.* **81**, 3920–3923 (1998).

[28] Senellart, P. & Bloch, J. Nonlinear emission of microcavity polaritons in the low density regime. *Phys. Rev. Lett.* **82**, 1233–1236 (1999).

[29] Savvidis, P. G. *et al.* Angle-resonant stimulated polariton amplifier. *Phys. Rev. Lett.* **84**, 1547–1551 (2000).

[30] Huang, R. *et al.* Exciton-polariton lasing and ampli.cation based on exciton-exciton scattering in a cdte microcavity quantum wells. *Phys. Rev. B.* **65**, 165314–1–7 (2002).

[31] Richard, M., Kasprzak, J., Romestain, R., Andre, R. & Dang, L. S. Spontaneous coherent phase transition of polaritons in cdte microcavities. *Phys. Rev. Lett.* **94**, 187401 (2005).

[32] Weihs, G. *et al.* Exciton-polariton lasing in a microcavity. *Semicond. Sci. Technol.* **18**, S386–S394 (2003).

[33] Shelykh, I. *et al.* Semiconductor microcavity as a spin-dependent optoelectronic device. *Physical Review B (Condensed Matter and Materials Physics)* **70**, 35320–1–5 (2004).

[34] Deng, H. *et al.* Quantum degenerate polaritons in thermal equilibrium. *arXiv.org:cond-mat/0604394* (2006).

[35] Einstein, A. Quantentheorie des einatomigen idealen Gases. Zweite Abhandlung. *Sitzungber. Preuss. Akad. Wiss.* **1925**, 3 (1925).

[36] London, F. The λ-phenomenon of liquid helium and the Bose-Einstein degeneracy. *Nature* **141**, 643 (1938).

[37] Allen, J. & Misener, A. Flow of liquid helium ii. *Nature* **141**, 75 (1938).

[38] Kapitza, P. Viscosity of liquid helium below the λ-point. *Nature* **141**, 74 (1938).

[39] Griffin, A., Snoke, D. W. & Stringari, S. *Bose-Einstein Condensation* (Cambridge University Press, 1995).

[40] Pitaevskii, L. & Stringari, S. *Bose-Einstein Condensation* (North-Holland, 1974).

[41] Bogolubov, N. On the theory of superfluidity. *J. Phys.* **11**, 23 (1947).

[42] Beliaev, S. T. Energy-spectrum of a non-ideal Bose gas. *Sov. Phys. JETP* **34**, 299 (1958).

[43] Pitaevskii, L. P. Vortex lines in an imperfect Bose gas. *Sov. Phys. JETP* **13**, 451 (1961).

[44] Griffin, A. A brief history of our understanding of BEC: From Bose to Beliaev in *Proceedings of the International School of Physics - Enrico Fermi* (eds. Inguscio, M., Stringari, S. & Wieman, C. E.) 1 (IOS Press, 1999) and refereces therein.

[45] Mermin, N. D. & Wagner, H. Absence of ferromagnetism or antiferromagnetism in one-or-two dimensional isotropic Heisenberg models. *Phys. Rev. Lett.* **17**, 1133 (1966) erratum: PRL, Vol. 17, No.26, 12/26/66.

[46] Hohenberg, P. Existence of long-range order in one and two dimensions. *Physical Review* **158**, 383–386 (1967).

[47] Khalatnikov, I. M. *An Introduction to the Theory of Superfluidity* (W.A. Benjamin, New York, 1965).

[48] Ketterle, W. & van Druten, N. J. Bose-Einstein condensation of a finite number of particles trapped in one or three dimenstions. *Phys. Rev. A* **54**, 656 (1996).

[49] Hanamura, E. & Haug, H. Condensation effects of excitons. *Physics Reports. Physics Letters Section C* **33C**, 209–284 (1977).

[50] Wannier, G. H. The structure of electronic excitation levels in insulating crystals. *Phys. Rev.* **52**, 191–197 (1937).

[51] Luttinger, J. M. & Kohn, W. Motion of electrons and holes in perturbed periodic fields. *Phys. Rev.* **97**, 869–883 (1955).

[52] Leavitt, R. & Little, J. Simple method for calculating exciton binding energies in quantum-confined semiconductor structures. *Physical Review B (Condensed Matter)* **42**, 11774–11783 (1990).

[53] Priester, C., Allan, G. & Lannoo, M. Wannier excitons in gaas-gasub 1-xalsub xas quantum-well structures: influence of the effective-mass mismatch. *Physical Review B (Condensed Matter)* **30**, 7302–7304 (1984).

[54] Borns, M. & Wolf, E. *Principles of Optics* (Cambridge Univ. Press, Cambridge, England, 1997).

[55] Hopfield, J. J. Theory of the contribution of excitons to the complex dielectric constant of crystals. *Phys. Rev.* **112**, 1555–1567 (1958).

[56] Khurgin, J. B. Exciton radius in the cavity polariton in the regime of very strong coupling. *Solid State Commun.* **117**, 307–310 (2000).

[57] Citrin, D. S. & Khurgin, J. B. Microcavity effect on the electron-hole relative motion in semiconductor quantum wells. *Physical Review B (Condensed Matter and Materials Physics)* **68**, 205325–1–5 (2003).

[58] Kavokin, A., Malpuech, G., Lagoudakis, P. G., Baumberg, J. J. & Kavokin, K. Polarisation rotation in resonant emission of semiconductor microcavities. *phys. stat. sol.* **195**, 579–586 (2003).

[59] Feshbach, H. A unified theory of nuclear reactions. II. *Ann. Phys.* **19**, 287 (1962).

[60] Pau, S., Bjork, G., Cao, H., Hanamura, E. & Yamamoto, Y. Theory of inhomogeneous microcavity polariton splitting. *Solid State Communications* **98**, 781–784 (1996).

[61] Tassone, F., Piermarocchi, C., Savona, V., Quattropani, A. & Schwendimann, P. Photoluminescence decay times in strong-coupling semiconductor microcavities. *Phys. Rev. B* **53**, R7642–R7645 (1996).

[62] Tassone, F., Piermarocchi, C., Savona, V., Quattropani, A. & Schwendimann, P. Bottleneck effects in the relaxation and photoluminescence of microcavity polaritons. *Phys. Rev. B.* **56**, 7554–7563 (1997).

[63] Müller, M., Bleuse, J., Andre, R. & Ulmer-Tuffigo, H. Observation of bottleneck effects on the photoluminescence from polaritons in ii-vi microcavities. *Physica B* **272**, 476–479 (1999).

[64] Tartakovskii1, A. I. *et al.* Relaxation bottleneck and its suppression in semiconductor microcavities. *Phys. Rev. B.* **62**, R2283–R2286 (2000).

[65] Huang, R., Tassone, F. & Yamamoto, Y. Experimentel evidence of stimulated scattering of excitons into microcavity polaritons. *Phys. Rev. B.* **61**, R7854–R7857 (2000).

[66] Panzarini, G. *et al.* Exciton-light coupling in single and coupled semiconductor microcavities: Polariton dispersion and polarization splitting. *Phys. Rev. B.* **59**, 5082–5089 (1999).

[67] Björk, G., Karlsson, A. & Yamamoto, Y. Definition of a laser threshold. *Phys. Rev. A.* **50**, 1675–1680 (1994).

[68] Raja, M., Brueck, S., Scully, M. & Lee, C. Resonant periodic-gain surface-emitting semiconductor lasers and correlated emission in a ring cavity. *Phys. Rev. A.* **44**, 4599–607 (1991).

[69] Glauber, R. J. The quantum theory of optical coherence. *Phys. Rev.* **130**, 2529–2539 (1963).

[70] Gardiner, C. W. & Zoller, P. *Quantum Noise* (Springer-Verlag, New York, 2000).

[71] El Daif, O. *et al.* Polariton quantum boxes in semiconductor microcavities. *APPLIED PHYSICS LETTERS* **88**, 061105 (2006).

[72] Pawlis, A. *et al.* Large room temperature rabi-splitting in a znse/(zn,cd)se semiconductor microcavity structure. *Solid State Commun.* **123**, 235–238 (2002).

[73] Tawara, T., Gotoh, H., Akasaka, T., Kobayashi, N. & Saitoh, T. Cavity polaritons in ingan microcavities at room temperature. *Physical Review Letters* **92**, 256402–256405 (2004).

[74] Butte, R. *et al.* Room-temperature polariton luminescence from a bulk gan microcavity. *Physical Review B (Condensed Matter and Materials Physics)* **73**, 33315–1–4 (2006).

[75] Inouye, S. *et al.* Superradiant rayleigh scattering from a bose-einstein condensate. *Science* **285**, 571–574 (1999).

[76] Deng, L. *et al.* Four-wave mixing with matter waves. *Nature* **398**, 218–220 (1999).

[77] Inouye, S. *et al.* Phase-coherent amplification of atomic matter waves. *Nature* **402**, 641–644 (1999).

[78] Kozuma, M. *et al.* Phase-coherent amplification of matter waves. *Science* **286**, 2309–2312 (1999).

[79] Moore, M. & Meystre, P. Atomic four-wave mixing: Fermions versus bosons. *Phys. Rev. Lett.* **86**, 4199–4202 (2001).

[80] Ketterle, W. & Inouye, S. Does matter wave amplification work for fermions? *Phys. Rev. Lett.* **86**, 4203–4206 (2001).

[81] Dicke, R. H. Coherence in spontaneous radiation processes. *Phys. Rev.* **93**, 99–110 (1954).

[82] Arecchi, F. T., Courtens, E., Gilmore, R. & Thomas, H. Atomic coherent states in quantum optics. *Phys. Rev. A.* **6**, 2211–2237 (1972).

[83] Sakurai, J. J. *Modern Quantum Mechanics* (Addison-Welsley, New York, 1995).

[84] Deng, H., Weihs, G., Santori, C., Bloch, J. & Yamamoto, Y. Condensation of microcavity quantum well exciton-polaritons. *Science* **298**, 199 – 202 (2002).